

1969

Liquid-metal corrosion effects of iron additions on uranium-chromium eutectic in yttrium

Robert James Cash
Iowa State University

Follow this and additional works at: <https://lib.dr.iastate.edu/rtd>

 Part of the [Nuclear Engineering Commons](#), and the [Oil, Gas, and Energy Commons](#)

Recommended Citation

Cash, Robert James, "Liquid-metal corrosion effects of iron additions on uranium-chromium eutectic in yttrium " (1969). *Retrospective Theses and Dissertations*. 4644.
<https://lib.dr.iastate.edu/rtd/4644>

This Dissertation is brought to you for free and open access by the Iowa State University Capstones, Theses and Dissertations at Iowa State University Digital Repository. It has been accepted for inclusion in Retrospective Theses and Dissertations by an authorized administrator of Iowa State University Digital Repository. For more information, please contact digirep@iastate.edu.

**This dissertation has been
microfilmed exactly as received**

69-15,602

CASH, Robert James, 1938-
LIQUID-METAL CORROSION EFFECTS OF
IRON ADDITIONS ON URANIUM-CHROMIUM
EUTECTIC IN YTTRIUM.

Iowa State University, Ph.D., 1969
Engineering, nuclear

University Microfilms, Inc., Ann Arbor, Michigan

LIQUID-METAL CORROSION EFFECTS
OF IRON ADDITIONS ON URANIUM-CHROMIUM EUTECTIC IN YTTRIUM

by

Robert James Cash

A Dissertation Submitted to the
Graduate Faculty in Partial Fulfillment of
The Requirements for the Degree of
DOCTOR OF PHILOSOPHY

Major Subject: Nuclear Engineering

Approved:

Signature was redacted for privacy.

In Charge of Major Work

Signature was redacted for privacy.

Head of Major Department

Signature was redacted for privacy.

Dean of Graduate College

Iowa State University
Of Science and Technology
Ames, Iowa

1969

TABLE OF CONTENTS

	Page
INTRODUCTION	1
OBJECT OF THIS INVESTIGATION	5
THEORY OF LIQUID-METAL SOLUTIONS	6
Liquid-Metal Solution Models	12
Immiscibility in Liquid-Metal Solutions	14
Determining the Solubility of Yttrium	21
CORROSION BY LIQUID METALS	41
Liquid-Metal Corrosion Mechanisms	41
Factors Affecting Liquid-Metal Corrosion	76
REVIEW OF THE LITERATURE	78
Uranium-Chromium-Iron Phase Studies	78
Corrosion by Uranium Alloys	79
EXPERIMENTAL PROCEDURE	84
Corrosion Tests Procedure	85
Differential Thermal Analyses	89
Solubility Tests Procedure	92
Methods of Capsule Examination	95
Materials	97
RESULTS AND DISCUSSION	103
Uranium-Chromium-Iron Phase Studies	103
Corrosion Tests Results	114
Solubility Tests Results	141
CONCLUSIONS	157

	Page
RECOMMENDATIONS FOR FURTHER STUDY	161
NOMENCLATURE	163
BIBLIOGRAPHY	167
ACKNOWLEDGMENTS	175
APPENDIX A	176
APPENDIX B	185

INTRODUCTION

The technology of liquid metals is a field which has been greatly stimulated by the advancement of the atomic energy program. More information is probably available about the use of liquid metals as coolants than for any other application. However, various metals are also considered for use as extraction agents in high temperature reprocessing of reactor fuels, as liquid-metal blanket systems, as liquid-metal fuel carriers, and as liquid-metal reactor fuels. The last category is the subject of this investigation.

As the interest in nuclear reactors intensifies, many new types of fuels are being suggested and tried in order to improve the economics of producing nuclear power. Nuclear fuel alloys in the molten state possess several attractive properties, such as 1. the ability to release the bulk of the volatile fission products, 2. little or no radiation damage, 3. increased utilization of fuel because of possible higher burn-up, 4. simplified fuel handling and lower fabrication costs, and 5. an extra degree of reactor stability as a result of the large negative temperature coefficient of reactivity.

Coupled with the advantages of molten alloys, however, is the potential for corrosion of the container with a resulting loss of fuel. Containment or corrosion by liquid metals is perhaps the most important and most difficult problem encountered in their application. The majority of the early work concerning the containment problem involved the "trial and error" approach. This method categorized certain metals and alloys as to whether they would contain a particular liquid metal at given temperatures

for various periods of time (1). Later other investigations were conducted to determine the types of interactions, such as dissolution of the solid container, intergranular penetration, compound formation, etc., which can occur between a liquid metal and a solid container.

Previous experience with potential liquid-metal reactor fuels has shown that the solubility limits and immiscibility of containment materials in particular liquid metals are decisive factors for a compatible system. The refractory metals and several chromium-molybdenum steels showed the best resistance to attack because of their low solubility and immiscibility properties. In 1958, another metal, yttrium, was reported to be nearly immiscible with liquid uranium (2); therefore it is also of interest.

An important aspect of developing a liquid-metal fueled reactor system is the proper choice of liquid metals. When using uranium liquid-metal fuels, a number of properties must be considered. Consideration must be given to 1. melting points, 2. percentages of fissionable material, 3. heat transfer properties, 4. vapor pressures, 5. neutron absorption cross sections, and 6. corrosiveness at the temperatures of operation. In most cases the corrosiveness will dictate a certain alloy over others which may have more desirable properties.

Reactor fuel temperatures are certain to rise as reactor technology advances. In today's power reactors, the solid-state nuclear fuel and its radioactive fission products are sealed in an envelope. Because this structural configuration must remain intact, the reactor temperature is limited to values of less than 1000°K. However, by relaxing the requirement for the absolute containment of fuel and fission products, and by an appropriate choice of materials, temperatures of 2000°K or more are being

obtained in nuclear-rocket reactor experiments (3). This approach throws the door wide open for liquid metals both as coolants and as nuclear fuels. On the conservative side, Los Alamos Scientific Laboratory (4, 5) envisages maximum fuel to container interface temperatures for a reactor to be in the range of 850 to 1000°C.

The 1133°C melting point of unalloyed uranium is too high for today's material technology, but various alloys of uranium have considerably lower melting points. Since previous work has been conducted with uranium-bismuth and other low-percentage uranium alloys (6, 7), investigation of the high-percentage uranium alloys is suggested. Suitable uranium-base alloys may be found among uranium's lowest melting binary eutectics with chromium, manganese, iron, cobalt, and nickel. Table 1 lists the composition and melting points of these eutectic alloys.

Table 1. Composition and melting point data^a for five uranium eutectic alloys

Eutectic alloy	Composition wt. %	Eutectic isotherm °C	Known compounds
U-Cr	95.0 % U- 5.0 % Cr	859	None
U-Mn	94 % U- 6 % Mn	716	UMn ₂ , U ₆ Mn
U-Fe	89.0 % U-11.0 % Fe	725	UFe ₂ , U ₆ Fe
U-Co	89 % U-11.0 % Co	734	6 ^b
U-Ni	89.5 % U-10.5 % Ni	740	7 or more ^c

^aData from References 8, 9.

^bSee Elliott (9) for more information.

^cSee Hansen and Anderko (8) for more information.

The observed order of increasing corrosiveness to yttrium and the refractory metals is U-Cr, U-Mn, U-Fe, U-Co, and U-Ni in accordance with ascending group numbers in the Periodic Chart (4, 5, 10), although the latter three eutectics appear to be about equally corrosive. The advantage of the uranium-chromium eutectic being the least corrosive is offset by its higher melting point. However, with a small addition of manganese, iron, cobalt, or nickel, it is possible to lower the melting point below 800°C. Because of this, U-Cr eutectic has potential as a liquid-metal fuel and its corrosion characteristics and liquid-metal properties are worthy of evaluation.

OBJECT OF THIS INVESTIGATION

The purpose of this investigation is to further the understanding of the field of liquid-metal corrosion by testing two possible liquid-metal reactor fuels, uranium-chromium eutectic and uranium-chromium-iron, in containers constructed of yttrium. The study was conducted using nominally static, isothermal test capsules as opposed to more expensive liquid-metal loops.

The objective of the experimental work was to establish the compatibility of uranium-chromium eutectic with and without iron additions and their interactions with the container metal, yttrium; and to make a preliminary study of the ternary eutectic composition in the uranium-chromium-iron system and a determination of yttrium solubility in the uranium-chromium eutectic with time. A further objective was to explain the results of the experimental tests in terms of the available theory on liquid-metal solutions and the various mechanisms by which liquid-metal corrosion can occur.

THEORY OF LIQUID-METAL SOLUTIONS

The feasibility of all applications of liquid metals rest on the solubility or insolubility of other metals in the liquid metal of interest. Various authors have tried to show some dependence of solubility on such factors as the band structure of the solution, the atomic radii of the solute and solvent species, the electronegativities, the valencies, and the excitation energies of the atoms. Correlations of solubility with the Periodic Table both by group number and atomic number, with the solute melting points, with miscibility-gap systems and the Hildebrand (11) solubility parameters, and with thermodynamic and other properties of the pure constituents have been made by numerous authors with some degree of success.

The structure of a dilute liquid-metal solution in most cases is similar in a broad sense to that of the corresponding solid solution (12). The similarity, however, extends only to the immediate region around any particular atom. This has been proved by X-ray diffraction experiments which show that metallic elements and solutions melt to form nearly close-packed arrangements of atoms in the liquid state, even in cases where the solid is not close-packed. In metals that are not close-packed such as bismuth, the coordination number for the liquid is considerably greater than the solid, thus showing the tendency towards a close-packed structure in the liquid state.

Although interpretations of X-ray data supporting that liquid metals contain aggregates resembling the solid structures are made by various authors, Hultgren and Orr (13) argue that these conclusions are questionable

in the sense that other hypotheses can explain the data equally well. The short-range order that is present is more a result of the metallic bonding through the sharing of electrons of nearest neighbors than from any specific crystal lattice. The ordering is present up to distances of about twice the interatomic spacings of the solid and rapidly become obscure at distances greater than this.

Hildebrand and Scott (14, 15) have argued and shown by various experiments that the existence of long-range solid-like structures in liquids above their melting points are untenable. The transition from a solid to a liquid and vice versa is a discontinuous process. Hildebrand and Scott argue that a liquid several tenths of a degree above its melting point does not show the slightest intimation of what will happen as its temperature is lowered. That is, if any "solid-like" structures or "seeds" were present as postulated by Eyring and Ree (16), the fraction present would increase with descending temperature until the liquid solidified and long-range ordering again occurred. In 1936 Frenkel (17) also stated that "...to our views the liquid state is in all respects intermediate between the solid (crystalline) and the gaseous one and can be in principle, connected with them by continuous transitions...". While today's theories on liquid solutions follow the reasoning of Hildebrand and Scott and Hultgren and Orr; nevertheless, a certain lack of regularity is found in solids at temperatures near their melting-points, as if a portion of the atoms were "dissolved" in the lattice and a portion of the lattice points were vacant. Furthermore, a certain amount of regularity is still found by X-ray analysis of liquids as mentioned above, especially near the solidification point.

The atoms of liquid metals are not vibrating about fixed positions, but each is milling around with its immediate neighbors in essentially a random fashion. In fact, this assumption of randomness is a necessary postulate for several of the theoretical models used to predict thermodynamic properties and behavior in liquid solutions. Several examples are the ideal-solution model which obeys Raoult's law, Hildebrand's regular-solution model (11, 14), Bernal's molecular theory model (18), and Hardy's sub-regular solution model (19). The bonds in a liquid solution are almost the same as those in a solid solution but not of a nature to cause much ordering.

In a pure liquid metal each interior atom is metallically bound to its neighboring atoms through a sharing of electrons. The atoms at the surface of the metal are similarly bound, but the number of nearest neighbors and hence the number of bonds associated with a surface atom are fewer than for an interior atom. On the other hand, the strength of the bonds at the surface is greater than that of the interior bonds, being proportional to the heat of vaporization ΔH_v divided by the number of bonds. Each atom, however, is able to move throughout the liquid medium and possesses a rapid thermal motion of a translational nature. The mobility increases with temperature. Hence, the number of nearest neighbors is the time-averaged atomic environment about any given atom within the liquid.

For a liquid metal which exhibits a face-centered-cubic (FCC) or a hexagonal-close-packed (HCP) structure just prior to melting, the number of nearest neighbors should be close to 12, the coordination number for the closest-packing type structures. For the body-centered-cubic (BCC) structure, the coordination number for the solid is 8. X-ray diffraction experiments using the "radial distribution function" (20, 21, 22) reveal

no significant differences between the liquid and solid structures of BCC, FCC, and HCP metals, although slight changes in the number of nearest neighbors and in the distance of spacings are found. Coordination numbers for liquid metals vary from approximately 8 to nearly 12 (13, 20, 22) and show a nearly closed-packed arrangement. The number of nearest neighbors logically decreases with increasing temperature because of the increase in the interatomic spacing and loss of any short-range order.

In like manner, the interior and surface atoms of a solid metal are similarly bound, but in this case the motion of the atoms would be limited essentially to oscillatory movements. A definite crystal lattice exists with long range order, and each atom has a fixed number of nearest neighbors except where a crystal defect might be located. Such defects would probably be manifested as grain boundaries and vacancies. The presence of a liquid metal at the surface will tend to alter the bonding of the solid's surface atoms especially near the points of imperfection and start the liquid-metal corrosion process.

Sauerwald et al. (23) have been able to classify molten binary alloy systems into four main groups as a result of a systematic consideration of their properties. They have listed the systems as follows:

1. Systems which exhibit intermetallic compounds in the solid phase (V Systems).
2. Systems whose properties show no peculiarities, but can be postulated by a mean-value theorem (L Systems). Essentially these are ideal solutions.
3. Systems showing certain segregation tendencies such as miscibility gaps (E Systems).

4. Intermediate systems which mutually pass from one group into another (Z Systems).

The first three groups of binary solutions are classified as having short-range order, statistical species distribution, and short-range segregation, respectively. Strong linkages between unlike atoms cause preferential short-range order (V Systems) while the absence of the linkage leads to a random distribution (L Systems). Segregation tendencies result from a preponderance of self-linkages between like atoms (E Systems). Of the 789 constitutional diagrams examined, only 23 did not fit satisfactorily into the systematic classifications.

Since the systems U-Y and U-Cr-Y investigated in this paper exhibit miscibility gaps, the following property values associated with the E Systems should exist:

1. The phase diagrams exhibit points of inflection at the beginning and end of the miscibility gap.
2. X-ray data reveal short range segregation; i.e., short-range ordering of like-groups of atoms.
3. Surface tensions show strong surface activity.
4. Viscosities exhibit points of inflection as the solution compositions are changed.
5. The activity of the solutions will show a positive deviation from the ideal; i.e., positive deviations from Raoult's law are to be expected.
6. The heat of mixing (ΔH_{mix}) will have a positive value in the range of +100 to +2000 cal/mole.
7. The excess entropy (ΔS^{XS}) will be positive in the range of +0.1

to +0.8 cal/mole.

8. Values for the free energy of mixing (ΔF_m) will be in the range of -15 to -1000 cal/mole.

Entropy, either of melting or as excess entropy, is a function of the state of order of the solid state; thus, those systems which exhibit low entropies upon melting or when forming a solution exhibit little change in order, and liquid state coordination numbers should agree closely with those of the solid. Such is the case for pure uranium and yttrium upon melting as well as for the miscibility gap systems as shown by Sauerwald et al. (23).

Thermodynamic and solubility data on the uranium-yttrium alloy system are meager; none could be found on the systems uranium-chromium-yttrium and uranium-chromium-iron-yttrium.

A phase diagram for the U-Y system has not been determined to date mainly because the miscibility gap extends nearly across the whole composition range in both the solid and liquid states. Solubilities of yttrium in molten uranium have been reported by Haefling and Daane (2) from 1150°C (0.075 wt.%) to 1250°C (0.11 wt.%). Also, metallographic evidence of a slight eutectic depression at the uranium-rich end was found.

The Mound Laboratory (24, 25) evaluated yttrium as a possible container material for viscosity measurements with liquid uranium at 1200°C, but found the metal unsuitable because of its slight solubility in uranium. The author also investigated the U-Y system at the Ames Laboratory for corrosion and solubility limits at temperatures from 1150 to 1300°C (26). Sheinhartz et al. (27) determined physical and mechanical properties of various solid U-Y dispersions by means of powder metallurgy techniques.

No compounds were formed and both elements would have segregated if the matrix had been heated above the melting point of uranium. Unfortunately, these investigators did not determine any thermodynamic properties or correlate the U-Y system with available liquid metal solution models.

Liquid-Metal Solution Models

Several reliable sources of thermodynamic data on pure uranium and yttrium are available (28, 29, 30). If one is willing to draw upon one or more of the theoretical models used to predict various thermodynamic properties, it is feasible to estimate some values with a certain degree of accuracy. Oriani (31) in a critique of statistical theory models and interaction theory models concluded that these existing models are able to give the experimentalist some, but very little, qualitative guidance. On the other hand, Sundquist (32) in reviewing three models for thermodynamic properties of miscibility-gap systems found the model developed by Lumsden to give results that are often in excellent agreement with experiment and not off by more than 30%--a small error in the theoretical field of thermodynamics of liquid-metal solutions. Pratt (33) reached essentially the same conclusions about the Lumsden model as well as the sub-regular treatment by Hardy (19). After an examination by computer, Anderson (34) suggested that the sub-regular model is most successful for exothermic systems while the Lumsden model, which is dependent upon atomic radii, works best for endothermic systems. This is so because endothermic systems are usually associated with atomic size disparity. Oriani and Alcock (35) also prefer the sub-regular and Lumsden models but state that miscibility-gap systems are consistent with the regular-solution model of Hildebrand (11).

The fact that the systems U-Y and UCr-Y contain miscibility gaps enables one to treat these systems in a special fashion. As shown by Sauerwald et al. (23) above, these systems have certain unique properties. Application of any one of the regular, sub-regular, or Lumsden solution models can be made to determine certain necessary thermodynamic properties. Since the regular solution model is the easiest to work with and a considerable number of predictions are based upon this theory, it will be applied to the systems in this investigation.

First, however, an examination of why systems exhibit immiscibility will be made. From the Hume-Rothery rules (21) it can be seen that certain conditions must be satisfied in order to form a liquid-metal solution.

1. The relative sizes of the solute and solvent atoms must be such that the solvent lattice will not be unduly strained by the presence of the foreign solute atom. This size criterion requires that, for substitutional-type solution, the relative sizes be nearly the same while interstitial-type solutions are to be expected if the solute atoms are 15% or more smaller than those of the solvent. On the other hand, if the solute atoms are more than 15% larger than the solvent atoms, limited solubility and miscibility are to be expected.

2. The lattice structures of the two elements must also be considered since the solubility depends on the type of bond formed in solution. Other conditions being equal, complete solubility can occur only when the components have similar crystal structures.

3. The valency differences play an important part since it was found that, other things being equal, a metal of lower valency is more likely to dissolve one of higher valency than vice versa.

4. Electronegativities which are interrelated with atomic radii and valency give an indication of the strength of the bonds between unlike atoms. The greater the difference in electronegativities for two elements, the larger the heat of formation or strength of bonding (36). The excess entropy of formation, ΔS^{XS} , also gives a clue to the bonding between like and unlike atoms. If ΔS^{XS} is negative, unlike-atoms form the strongest bonds; or if ΔS^{XS} is positive, there is a weaker bonding between solvent and solute atoms than between like-atoms.

For γ -uranium and α -yttrium atoms, the respective atomic diameters (9) are 3.02 and 3.556 angstroms, which is a size difference of 18%. On this basis little solubility and appreciable immiscibility would be expected. Yttrium shows the HCP structure to 1499°C (37) while uranium is BCC prior to melting; thus the two crystal structures are significantly different to hinder solution formation. Yttrium has a valency of +3, whereas uranium has a +4 valence; thus uranium will not dissolve yttrium (Rule 3) to any great extent. On the electronegativity scale, uranium and yttrium have values of 1.22 and 1.11 (38) respectively, so it would be expected that little bonding would occur, and ΔS^{XS} should be positive.

Immiscibility in Liquid-Metal Systems

Hildebrand and Scott (11) have presented a theory which holds for non-polar liquids that can be applied to systems as a check for immiscibility. This formulation has been modified by Mott (39) to apply to metal systems by introducing an allowance for the increased energy caused by differences in electronegativities. Using the theory suggested, Mott was able to account for 426 alloy systems out of 529. The simple Hildebrand rule only accounted

for 312 systems out of the 529 total. Some of those that disagree can be interpreted in terms of errors in calculation of the energy factors.

Shimoji (40) explained some of these exceptions by considering the repulsive forces as well as the attractive forces in liquid-metal solutions.

The condition for complete miscibility according to Hildebrand and Scott is given by

$$\frac{1}{2} (V_A + V_B) (\delta_A - \delta_B)^2 < 2RT \quad (1)$$

where V_A and V_B are the molar volumes of components A and B, and δ_A and δ_B are their Hildebrand solubility parameters defined by

$$\delta = \left[\frac{\Delta E^V}{V} \right]^{\frac{1}{2}} \cong \left[\frac{\Delta H^V - RT}{V} \right]^{\frac{1}{2}} \quad (2)$$

ΔE^V and ΔH^V are the energy and heat of vaporization for the pure components, R is the gas constant, and T is the absolute temperature.

Most solubility parameters listed in the literature (11, 39, 41) are calculated at 25°C where the value of RT (592 cal/mole) is usually neglected in comparison with ΔH^V , because it is less than the experimental error involved in determining ΔH^V values. Therefore, the condition for immiscibility becomes

$$\frac{1}{2} (V_A + V_B) (\delta_A - \delta_B)^2 > 2RT. \quad (3)$$

Mott modified Equation 3 by including a new term E_B , which represents the binding energy, as shown in Equation 4,

$$\frac{1}{2} (V_A + V_B) (\delta_A - \delta_B)^2 - E_B > 2RT. \quad (4)$$

The binding energy, E_B , is the combined energy of all the bonds which can form between the two elements. While its value cannot be calculated exactly, a first approximation is given by

$$E_B \approx 23,060 n(X_A - X_B)^2 \text{ cal/mole}, \quad (5)$$

where n is the number of bonds per atom, and X_A and X_B are the electronegativities of the pure elements in electron volts. Rearranging Equation 4, and substituting Equation 5, one obtains for immiscibility

$$k = \frac{\frac{1}{2} (V_A + V_B) (\delta_A - \delta_B)^2 - 2RT}{23,060 (X_A - X_B)^2} > n. \quad (6)$$

Presumably the maximum number of bonds formed by a given metal is directly related to its valency, which for the metals in the periodic chart varies from 1 to 6. Therefore, as a first approximation if k is greater than 6, then immiscibility should be expected and if the value of k is less than 1, the metals will be miscible. Mott set the limits $k \geq 6$ for some immiscibility and $k \leq 2$ for complete miscibility. The upper limit for the average number of nearest neighbors is 12; hence, the average maximum number of unlike nearest neighbors is 6, which is another reason for choosing this as the maximum number of bonds for Equation 6. For values between 2 and 6, the incidence of immiscibility depends upon relative atomic sizes.

Mott also extended his hypothesis briefly to ternary systems and listed several examples. To extend the range of miscibility of two metals A and B, it is suggested that the choice of the third metal C should be such that its solubility parameter δ_C be preferably in the range of $\delta_A \rightarrow \delta_B$ or not greatly different from either, and the electronegativity X_C should be as different as possible from X_A and X_B . On the other hand, to continue immiscibility or increase its range, one should try the opposite approach. That is, δ_C should differ from the range of $\delta_A \rightarrow \delta_B$ and each value, and X_C should be very close to X_A and X_B .

Before proceeding to analyze the systems studied in this paper via solubility parameters, it is necessary to point out the fact that δ 's are usually calculated at 25°C and change slightly with an increase in temperature. Hildebrand and Scott (11) point out, however, that for high melting and boiling metals, these changes are relatively slight because of small coefficients of thermal expansion and small changes in heat capacities, as well as small values for heats of fusion. For qualitative purposes, the value of $\delta_A - \delta_B$ for a particular binary system is independent of temperature and much the same for solid and liquid phases. The decrease in δ is also partially overcome by the term $(V_A + V_B)$ which increases with temperature.

By examining the various values in Tables 2 and 3, one can analyze the systems U-Y, UCr-Y, and UCrFe-Y which were studied in this investigation. The U-Fe system is also given for reference.

Table 2. Tabulation of data used to evaluate k in Equation 6^a

Element	Goldschmidt diameter d_G Å	Density $\rho_{20^\circ\text{C}}$ g/cc	Molar volume $V_{298^\circ\text{K}}$ cc/mole	Solubility parameter ^b $\delta_{298^\circ\text{K}}$ (cal/cc) ^{1/2}	Electronegativity χ eV
Chromium	2.54 (9)	7.19 (9)	7.23	114.6	1.56 (38)
Iron	2.54 (9)	7.86 (9)	7.11	118.2	1.64 (38)
Uranium	3.12 (9)	19.07 (9)	12.48	100.1	1.22 (38)
Yttrium	3.606 (37)	4.457 (37)	19.95	71.3	1.11 (38)

^aNumbers in parentheses refer to the references cited in the Bibliography.

^bCalculated from ΔH_V data in Reference 28 at 298°K using Equation 1 and neglecting the value of RT.

Table 3. Tabulation of k in Equation 6 using data from Table 2

System	$\frac{1}{2}(V_A + V_B)$ cc/mole	$(\delta_A - \delta_B)^2$ cal/cc	$\frac{1}{2}(V_A + V_B) \times$ $(\delta_A - \delta_B)^2$ cal/mole	$\frac{1}{2}(V_A + V_B) \times$ $(\delta_A - \delta_B)^2$ $-2RT^a$ cal/mole	$23,060 \times$ $(X_A - X_B)^2$ cal/mole	Mott number k Eq. 6
U-Cr	9.855	210.3	2,072	-2,789	2,666	-1.0
U-Fe	9.795	327.6	3,209	-1,652	4,068	-0.4
Cr-Y	13.59	1,874.9	25,480	20,619	4,670	4.4
Fe-Y	13.53	2,199.6	29,761	24,900	6,478	3.8
U-Y	16.215	829.4	13,449	8,588	279	30.8

^aThe value of $2RT$ (4861 cal/mole) was calculated at 1223°K (950°C), the temperature of interest in this investigation.

If one uses only the simple Hildebrand immiscibility rule (Equation 3), it is seen from column 4 of Table 3 that some immiscibility would be expected in the Cr-Y, Fe-Y, and U-Y systems at 950°C. In fact, however, only the system U-Y exhibits any immiscibility. Phase diagrams are available for the first four systems in Table 3 and are shown in Figures 1, 2, 3, and 4.

On the other hand when Mott's modification is taken into account, only the system U-Y should be expected to definitely show immiscibility. Both the Cr-Y and Fe-Y systems fall within the $2 < k < 6$ range, and from Table 2 it is seen that the atomic size difference is quite appreciable. Therefore, one might expect some immiscibility in the two systems. In Reference 9 note is made of two investigations where immiscibility was found in the Cr-rich end of the Cr-Y system, but other authors listed in the same

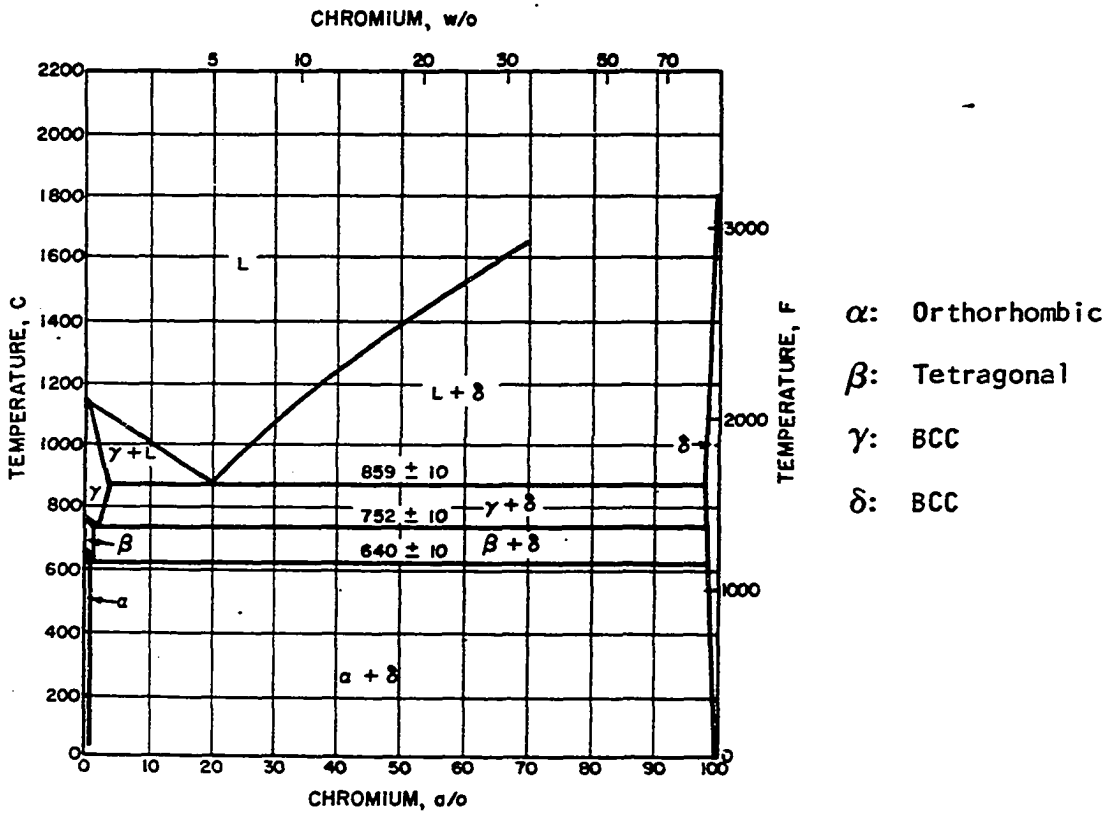


Figure 1. Uranium-chromium phase diagram (42)

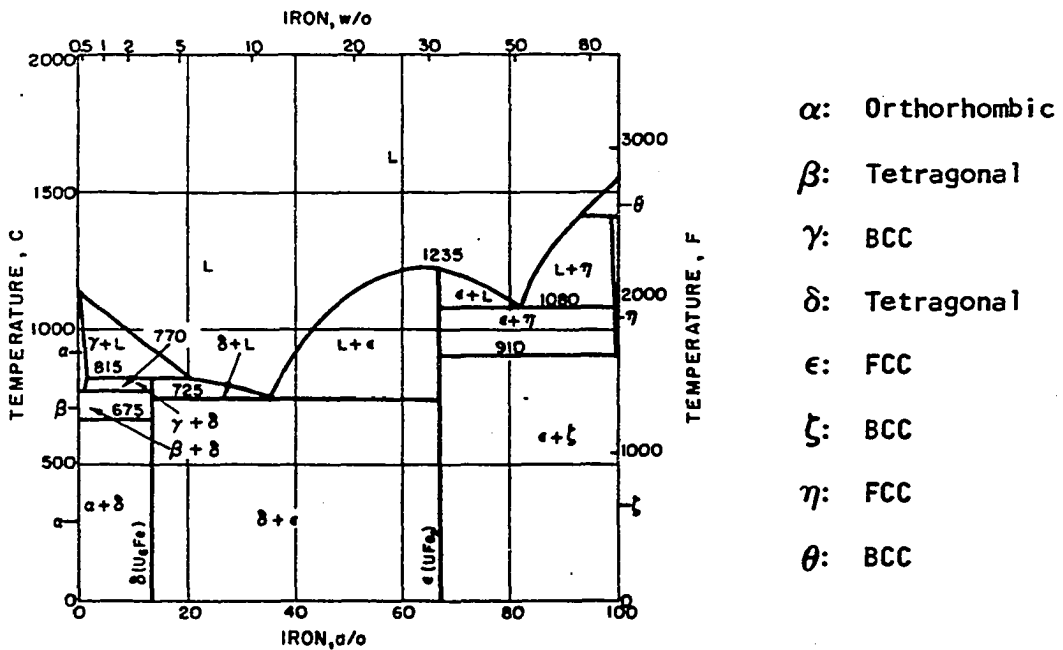
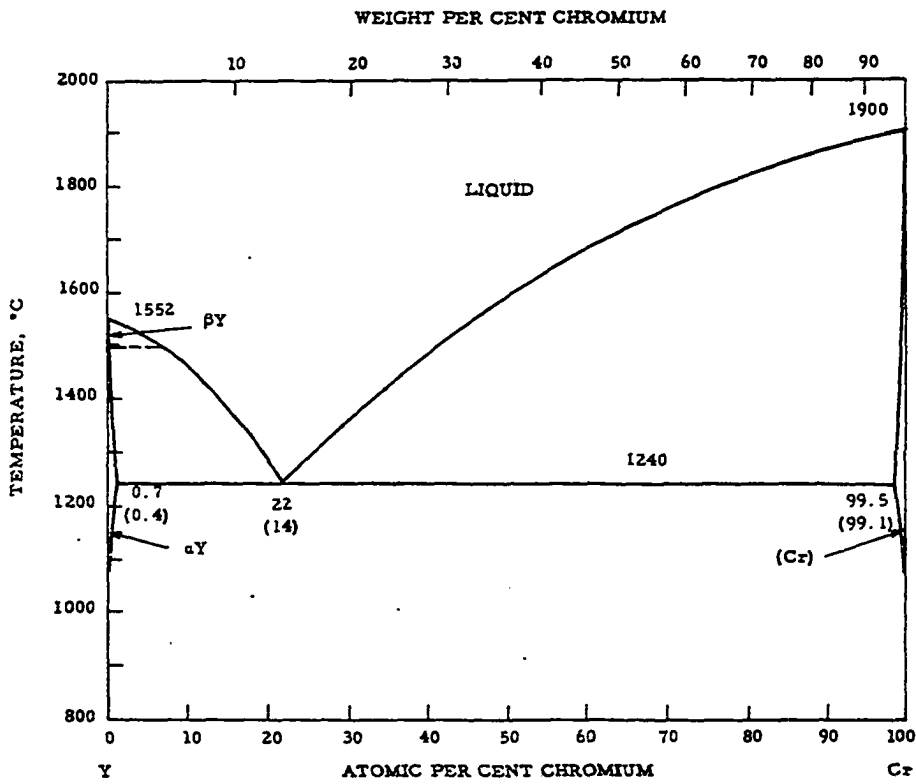
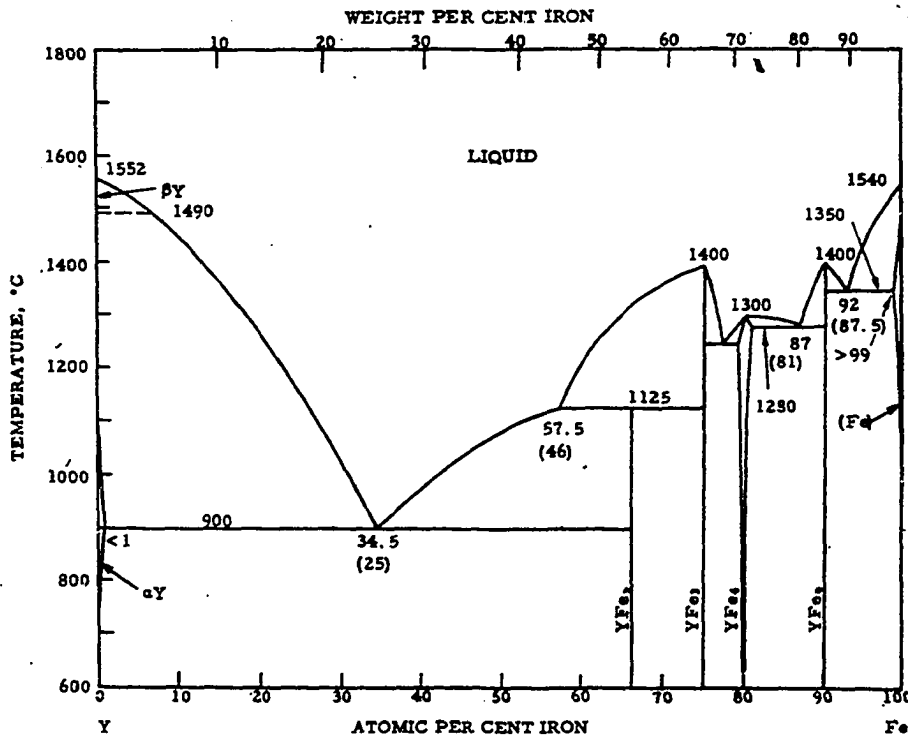


Figure 2. Uranium-iron phase diagram (42)



α Y: HCP
 β Y: BCC
 α Cr: BCC

Figure 3. Chromium-yttrium phase diagram (43)



α Y: HCP
 β Y: BCC
 α Fe: BCC
 γ Fe: FCC
 δ Fe: BCC

Figure 4. Iron-yttrium phase diagram (43)

reference refute this and suggest the error is caused by gravity segregation which appears to be liquid immiscibility.

Based on Mott's extension to ternary systems, it is seen from Table 2 that addition of chromium or iron to the U-Y system helps immiscibility from the solubility parameter viewpoint (δ_C is larger than δ_A or δ_B) but hinders it on the basis of electronegativity consideration (X_C is not close to X_A or X_B). Therefore, it is not possible to tell how the systems U-Cr in yttrium and U-Cr-Fe in yttrium might react in view of possible liquid-metal corrosion. One item of interest should be pointed out, however. Both the U-Cr and U-Fe systems show negative Mott numbers, thus indicating that the atoms of these systems form stronger bonds than the atoms of the systems Cr-Y and Fe-Y. From this standpoint, additions of chromium and iron should tend to alloy with uranium rather than with yttrium.

Determining the Solubility of Yttrium

In very dilute solution, which would be expected for yttrium in uranium, U-Cr eutectic, and U-Cr-Fe eutectic at 950°C, all solutes may be expected to obey Henry's law. That is, the activity of yttrium as a solute in solution is proportional to its mole fraction in solution

$$a_Y^L = k_Y^L N_Y^L, \quad (7)$$

where k_Y^L is the Henry's law constant for yttrium in the liquid solution and N_Y^L is the mole fraction of yttrium in solution. In dilute solutions, the constant may be considered as independent of solution composition. The constant may be identified with the activity coefficient,

$$a_Y^L = \gamma_Y^L N_Y^L \quad (8)$$

Likewise, the activity of yttrium in the solid phase is

$$a_Y^S = \gamma_Y^S N_Y^S. \quad (9)$$

At equilibrium, both activities are the same in both phases:

$$a_Y^L = a_Y^S = \gamma_Y^L N_Y^L = \gamma_Y^S N_Y^S. \quad (10)$$

But, $N_Y^S = 1$ and $a_Y^S = 1$ assuming no solubility of the liquid in yttrium; therefore, the activity of yttrium in the dilute solution is also unity, and its activity coefficient is simply the reciprocal of its mole fraction (44)

$$\gamma_Y^L = \frac{1}{N_Y^L} \quad (\text{for } N_Y^S = 1). \quad (11)$$

We could also have arrived at Equation 11 by considering 1. the common relationship of solubility versus temperature used to fit empirical data; i.e.,

$$\ln N = 2.3026 \log_{10} N = A - B/T, \quad (12)$$

where N is the atomic or mole fraction of solute in the saturated solution at the temperature $T^\circ\text{K}$, and A and B are assumed to be constants; and 2. the relationship for dilute solutions from solution theory

$$\ln \gamma \propto \frac{1}{T}. \quad (13)$$

Haefling and Daane (2) and Rough and Bauer (42) reported solubilities of yttrium (and other rare earths) in uranium from 1150 to 1250°C. Thus, by plotting these solubilities (converted to mole fractions) against reciprocal temperature, it is possible to estimate the solubility of yttrium in super-cooled uranium at 950°C. This has been done in Figure 5 with the data by

Haefling and Daane (see Table 4). The points do not all fall on a straight line because of experimental fluctuations in determining the solubilities. Therefore, a least squares treatment of the data was used to obtain the best line. This treatment gives $\ln N_Y^U = 0.544 - 9,416/T$.

Table 4. Solubility and activity coefficients for yttrium in uranium

Temp. °C	Temp. °K	$\frac{1000}{T}$ °K ⁻¹	Solubility		Activity coefficient γ_Y^U
			wt. %	at. %	
1300	1573	0.6357	(0.162) ^a	(0.433)	(231)
1250	1523	0.6566	0.15 ^b 0.114 ^c	0.401 0.305	249 328
1225	1498	0.6676	0.144 ^c	0.385	260
1200	1473	0.6789	0.118 ^c	0.315	317
1175	1448	0.6906	0.086 ^c	0.230	435
1150	1423	0.7027	0.075 ^b	0.201	498
950	1223	0.8177	(0.0292)	(0.0781)	(1280)
850	1123	0.8905	(0.00147)	(0.0393)	(2545)

^aValues in parentheses are extrapolated from a least squares fit of data from Haefling and Daane (2); $\ln N_Y^U = 0.544 - 9,416/T$.

^bData from Reference 42.

^cData from Haefling and Daane (2).

As a further check of the solubility data for yttrium in supercooled uranium one can try the method described by Pasternak (45) using effective solubility parameters. The method requires the knowledge of the solubility of one metal in liquid uranium which does not form intermetallic compounds.

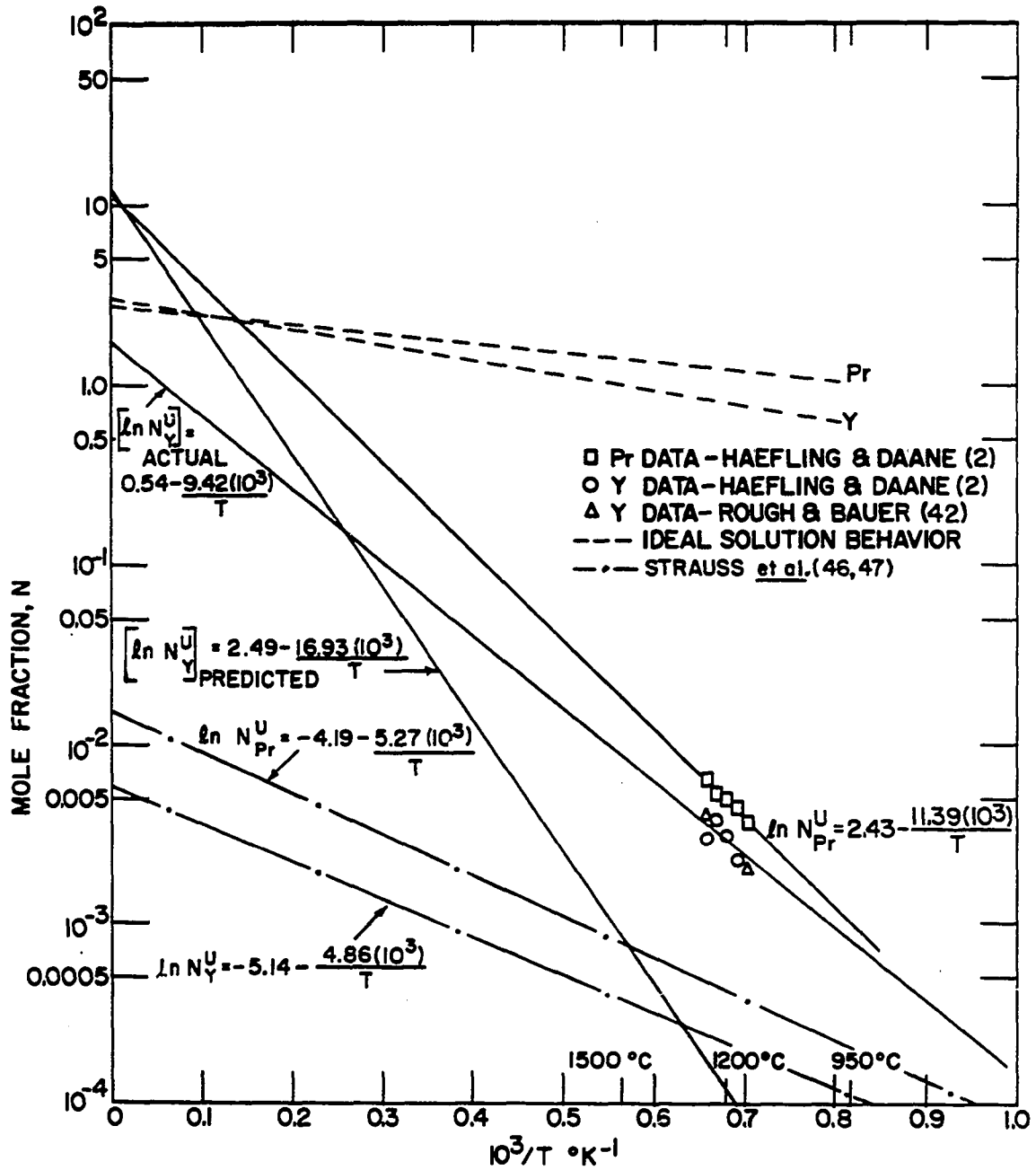


Figure 5. Comparison of yttrium and praseodymium in molten uranium as predicted experimentally and theoretically

The data listed by Haefling and Daane for praseodymium in uranium appeared to have the best correlation with temperature; hence, these data were used for the reference metal (see Table 5).

First, the solubility data for praseodymium are plotted as the $\ln N_{Pr}^U$ versus $1/T$ on semilog graph paper using a least squares fit. The straight line is extended to the limit of $1/T = 0$ where the value of N_{Pr}^U should be a measure of the excess partial molar entropy of mixing ($\Delta \bar{S}_{mix}^{XS}$) and the entropy of fusion (ΔS_m). Similarly the slope of this straight line gives the partial molar heat of solution ($\Delta \bar{H}_{Pr}$) if the heat of fusion (ΔH_m) is known. The equation of the straight line is represented by the following equation which is derived in Appendix A:

$$\ln N_{Pr}^U = A - \frac{B}{T} = \frac{\Delta S_m + \Delta \bar{S}_{Pr}^{XS}}{R} - \frac{\Delta H_m + \Delta \bar{H}_{Pr}}{RT}, \quad (14)$$

where N_{Pr}^U is the atomic or mole fraction of praseodymium in the liquid uranium solution at temperature $T^\circ K$, and A and B are constants determined by a least-squares fit. By assuming that the volume change on mixing is zero (a valid assumption for the rare earth-uranium systems because of the slight A-B type interactions), Hildebrand and Scott (11) have shown that

$$\Delta \bar{H}_A = V_A (\delta_A - \delta'_B)^2 \varphi_B^2 \quad (15)$$

where V_A is the molal volume of the solute, φ_B is the volume fraction of the solvent (≈ 1 for dilute solutions), δ_A is the Hildebrand solubility parameter for pure A, and δ'_B is the effective solubility parameter determined from the plotted data. With the calculated δ'_B , the solubility equation for the second rare earth in uranium is determined by Equations 16 and 17 by substituting the appropriate values for the solute of interest (yttrium),

$$|\text{slope}| = B = \frac{\Delta H_m + V_A (\delta_A - \delta_B)^2}{R} \quad (16)$$

$$A = \frac{\Delta S_m + \Delta \bar{S}_{Pr}^{-XS}}{R} \quad (17)$$

Figure 5 compares this treatment with the values obtained by Haefling and Daane. It is seen that the predicted solubility is too low by a factor of more than 10 in the 1200°C range. It must be recalled, however, that predicted values are based on the accuracy of the five data points for praseodymium listed in Table 5, the assumption that $\Delta C_p = 0$, and the fact that praseodymium is a liquid at the five temperatures listed. Actually, a better comparison would probably have resulted by using solubility data for gadolinium in uranium, but Haefling and Daane list only one value in their paper. Gadolinium is perhaps the rare earth which comes closest to the chemical properties of yttrium. No other data were found in the literature.

Temperature coefficient of solubility

At equilibrium solid metal A dissolved in liquid metal B can be written as



One can write for the conditions at equilibrium with the solution in its standard state (21)

$$\Delta F^\circ = -RT \ln K \quad (19)$$

where K, the equilibrium constant for reaction 18, is given in terms of the metal solubilities as

Table 5. Solubility data for praseodymium in uranium^a

Temp. °C	Temp. °K	$\frac{1000}{T}$ °K ⁻¹	Solubility wt.%	Solubility at.%	Mole fraction N_{Pr}^U
1150	1423	0.7027	0.22	0.371	0.00371
1175	1448	0.6906	0.27	0.455	0.00455
1200	1473	0.6789	0.30	0.506	0.00506
1225	1498	0.6676	0.32	0.539	0.00539
1250	1523	0.6566	0.39	0.657	0.00657

^aData from Haefling and Daane (2); least squares fit: $\ln N_{Pr}^U = 2.43 - 11,390/T$.

$$K = \frac{a_{A(B)}}{a_{A_{solid}}} \quad (20)$$

Since the solution $A_{(B)}$ is extremely dilute in the systems of interest, $a_{A_{solid}} \cong 1$ and Equation 19 becomes

$$\Delta F^\circ = -RT \ln a_{A(B)} \quad (21)$$

On a mole fraction basis $a_{A(B)}$ is N_A^B , the mole fraction of A in solution B. The temperature coefficient of solubility is simply the rate of change of solubility with temperature, $\frac{dN}{dT}$, but it is usually expressed as

$$\text{Temp. Coef. of Sol.} = - \frac{d(R \ln N_A^B)}{d(1/T)} = \frac{RT^2}{N_A^B} \frac{dN_A^B}{dT} \quad (22)$$

Hence, Equation 22 becomes

$$- \frac{d(R \ln N_A^B)}{d(1/T)} = \frac{d(\Delta F^\circ/T)}{d(1/T)} = \Delta H^\circ \quad (23)$$

from the van't Hoff equation. But ΔH° is the sum of the heat of fusion of pure solute A and the partial molar heat of solution at high dilution relative to pure liquid A.

$$-\frac{d(R \ln N_A^B)}{d(1/T)} = \Delta H^\circ = \Delta H_m + \Delta \bar{H}_A \quad (24)$$

That is, the temperature coefficient of solubility is the slope of the curve of $\ln N_A^B$ versus $1/T$ multiplied by the gas constant, R , as in Figure 5 and Equation 14. Again, it is related to the Hildebrand solubility parameter through Equation 16.

Strauss et al. (36, 46, 47) and White (48) have correlated the temperature coefficient of solubility and the A intercept (Equation 14) with an atomic size factor, S , for various liquid-metal solutions. S is defined as the ratio of the solvent radius to the solute radius. The data tend to fall on a curve shaped like the small letter "u" with a tail. Minimums occur at approximately $S = 1.0$ and 1.85 . As a comparison with Figure 5, the Strauss curves predict values of $\ln N_{Pr}^U = -4.19 - 5,270/T$ and $\ln N_Y^U = -5.14 - 4,860/T$. These values are too low by a factor of about 10 at 1200°C . Their slopes do not compare favorably with the corresponding experimental plots either. Hence, the Strauss curves do not seem to be applicable to these systems.

Estimating the uranium-yttrium system miscibility gap

The U-Y system exhibits a region of immiscibility across the composition range, but very slight solubilities exist at both ends with an eutectic at the U-rich side. Between these points immiscibility occurs, and the question of monotectic limits naturally arises. The extent of these

limits will also give a clue to the amount of dissolution corrosion which might occur.

By regular solution theory, it is possible to predict the limits of immiscibility by a method presented in Lewis and Randall (49). Since the mutual solubilities are quite small for U-Y, the activities of the metals are not appreciably different from unity. The activity coefficients are calculated from

$$\ln \gamma_A = \frac{a_{AB} V_A}{RT} \varphi_B^2 \quad (25)$$

where V_A is the molar volume of the solute, φ_B is the volume fraction of the solvent, R is the gas constant, a_{AB} is the Hildebrand interaction parameter expressing deviation from ideal behavior, and γ_A is the activity coefficient at $T^\circ\text{K}$. The parameter a_{AB} is estimated from thermodynamic data for the pure constituents using the solubility parameters and

$$a_{AB} = (\delta_A - \delta_B)^2. \quad (26)$$

The activity coefficients are given by

$$\gamma_B^A = \frac{1}{N_B^A}, \quad N_B^B \approx 1. \quad (27)$$

Equation 25 is readily derived from the expression for excess free energy of mixing, $\Delta F_{\text{mix}}^{\text{XS}}$, given by Scatchard (49) as

$$\Delta F_{\text{mix}}^{\text{XS}} = a_{AB} V \varphi_A \varphi_B \quad (28)$$

where V is the molar volume of the solution and φ_A and φ_B are the volume fractions of constituents A and B as defined in Equation 29 below. The term, $\Delta F_{\text{mix}}^{\text{XS}}$, is defined as the deviation from Raoult's law and is related to the energy of bonding for A-A, B-B, and A-B bonds. As given, Equation

25, is found to be useful for estimated values when experimental data are lacking. In addition, it applies to asymmetric systems with unequal molar volumes.

From Table 2 the solubility parameter for U is $100.1 \text{ (cal/cc)}^{\frac{1}{2}}$, and that for Y is $71.3 \text{ (cal/cc)}^{\frac{1}{2}}$. This gives 829.4 cal/cc for a_{AB} from Equation 26. With this value and $V_Y = 19.95 \text{ cc/mole}$, the activity coefficient for Y in supercooled liquid U at 950°C (assuming that the volume fraction of U is unity) from Equation 25 is 906.4. Using Equation 27, we get 0.110 at.% Y and 99.890 at.% U for the U-rich phase. At the Y-rich end, Equation 25 gives $\gamma_U^Y = 70.8$ for supercooled liquid uranium. Again with Equation 26, $N_U^Y = 1.413 \text{ at.\% U}$.

In a series of successive trials, the compositions calculated in a previous trial may be used to calculate the volume fractions (Equation 29), activity coefficients, and mole fractions in the following trial.

$$\varphi_A = \frac{V_A N_A}{V_A N_A + V_B N_B} ; \quad \varphi_B = \frac{V_B N_B}{V_A N_A + V_B N_B} . \quad (29)$$

Table 6 lists the limiting compositions of the mutual solubilities as predicted by Equation 25 for several temperatures. The values under the column N_Y^U are compared in Figure 7 with the experimental solubility data (Table 4). A least squares fit was used to plot the predicted solubility.

Estimating yttrium solubility in U-Cr and UCr-Fe eutectics

The next question which arises is how can yttrium be expected to react with U-Cr and UCr-Fe eutectic solutions? To answer this question one must again rely on the meager information available in the literature and upon the thermodynamic properties of the pure constituents.

Table 6. Limits of mutual solubility versus temperature for the U-Y system as predicted by Equation 25^a

Temp. °C	Temp. °K	RT cal/mole	^a AB ($\delta_Y - \delta_U$) ² cal/cc	ln γ_Y^U	γ_Y^U	N_Y^U		N_U^U at.%	ln γ_U^Y	γ_U^Y	N_U^Y at.%	N_Y^Y at.%
						at.%	wt.%					
850	1123	2232	829.4	(7.4135) ^b 7.3990	(1658) 1634	(0.0603) 0.0612 ^c	0.0229	99.939	(4.6375) 4.5778	(103.3) 97.30	(0.968) 1.028	98.972
950	1223	2430	829.4	(6.8095) 6.7849	(906.4) 884.4	(0.1103) 0.1131	0.0423	99.887	(4.2597) 4.1779	(70.79) 65.23	(1.413) 1.533	98.467
1050	1323	2629	829.4	(6.2940) 6.2555	(541.3) 520.9	(0.1847) 0.1920	0.0718	99.808	(3.9372) 3.8301	(51.27) 46.07	(1.950) 2.171	97.829
1150	1423	2828	829.4	(5.8511) 5.7944	(347.6) 328.4	(0.2877) 0.3045	0.1139	99.696	(3.6602) 3.5251	(38.87) 33.96	(2.573) 2.945	97.055
1175	1448	2877	829.4	(5.7515) 5.6896	(314.7) 295.8	(0.3175) 0.3381	0.1265	99.662	(3.5978) 3.4554	(36.52) 31.67	(2.738) 3.158	96.842
1200	1473	2927	829.4	(5.6532) 5.5858	(285.2) 266.6	(0.3506) 0.3751	0.1404	99.625	(3.5364) 3.3864	(34.34) 29.56	(2.912) 3.383	96.617
1225	1498	2977	829.4	(5.5583) 5.4850	(259.4) 241.0	(0.3855) 0.4149	0.1554	99.585	(3.4770) 3.3193	(32.36) 27.64	(3.090) 3.618	96.382
1250	1523	3027	829.4	(5.4665) 5.3871	(236.6) 218.6	(0.4226) 0.4575	0.1714	99.542	(3.4196) 3.2540	(30.56) 25.89	(3.273) 3.862	96.138
1300	1573	3126	829.4	(5.2933) 5.2007	(199.0) 181.4	(0.5025) 0.5513	0.2066	99.449	(3.3113) 3.1297	(27.42) 22.87	(3.647) 4.373	95.627

^aValues for V_U , V_Y , δ_U , and δ_Y are found in Table 2.

^bValues in parentheses are first trial results with $\phi^2 = 1$; values below are those obtained after 1 to 4 successive trials.

^cThe nine points fitted to Equation 12 by a least squares treatment yield: $\ln N_Y^U = 0.271 - 8,624/T$.

From Table 2 and Figure 1 (U-Cr phase diagram) it is seen that both γ -uranium and chromium exhibit BCC structures and that the chromium atom is about 17% smaller. Chromium should then form a substitutional-type solid solution with uranium, and indeed it does. There are no intermetallic compounds formed; hence A-B bonds are not predominant. Since an eutectic is formed, like atoms have greater attraction than unlike A-B atoms, but not to a point of immiscibility. Positive deviation from Raoult's law is thus the case, as it is for most metallic systems. The presence of 5.0 wt.% chromium in uranium has little effect on the phase transformation temperatures except for the $\gamma \rightarrow L$ transition. Saller et al. (50) report a lowering of approximately 10°C for the $\alpha \rightarrow \beta$ transition and about 17°C for the $\beta \rightarrow \gamma$ change.

Iron also exhibits a BCC structure to about 910°C at which point it changes to FCC. The atomic sizes of iron and chromium are very close, but the U-Fe system is seen to have two intermetallic compounds (Figure 2). Thus, the bonding of the A-B atoms is somewhat stronger than either A-A or B-B bonds. This is also reflected in the differences in electronegativities; 0.42 eV for U-Fe and 0.34 eV for U-Cr. A eutectic also exists in the system. The presence of iron at the U-Cr eutectic composition tends to lower the melting-point temperature. Saller et al. (51) report a 1.0 wt.% Fe addition to the U-Cr eutectic produces a ternary eutectic melting at approximately 757°C. This corresponds to a composition of 94.05 wt.% U-4.95 wt.% Cr-1.00 wt.% Fe (77.75 at.% U-18.73 at.% Cr-3.52 at.% Fe). Although this composition does not exhibit an eutectic structure as seen later in the Results and Discussion, the calculations presented on the following pages were made using the composition of Saller et al.

The phase diagrams for Cr-Y and Fe-Y (Figures 3 and 4) give one a fairly good indication as to what might happen in a liquid-metal corrosion system. Both systems exhibit eutectic-type diagrams, but Cr-Y has no intermetallic compounds whereas the Fe-Y system has four or more. Furthermore, the Fe-Y eutectic melts at 900°C, while that of the Cr-Y system melts at 1240°C. At 950°C, the temperature of interest in this investigation, one might expect Fe-Y compound formation and increased solution attack. On the other hand, because the amount of iron present is small and two other elements are also present in solution, the amount of corrosion which occurs may be less than normally expected. In the Y-rich region, the liquidus temperatures of both Cr-Y, and Fe-Y drop gradually from the melting point of yttrium to the eutectic points. From this standpoint, chromium and iron are similar with respect to yttrium.

The liquid characteristics for U-Cr eutectic and supercooled uranium towards yttrium should be similar. The presence of 81.6 at.% uranium in the matrix should tend to reduce the strength of Cr-Y type bonds. Hence, it might be expected that chromium would lower the solubility of yttrium. As a basis for comparison, the data on the solubility of cerium (a rare earth) in U-Cr eutectic (52) and uranium (2, 52) can be analyzed by using activity coefficients. Furthermore, both the U-Cr-Y and the U-Cr-Fe-Y systems can also be analyzed by use of Equation 25.

Voigt (52) reported the solubility of cerium in the U-Cr eutectic at 970°C to be 1.5 wt.% (2.15 at.%). This yields an activity coefficient, $\gamma_{\text{Ce}}^{\text{UCr}}$, at 970°C by Equation 27 of 46.5. By plotting the data from Haefling and Daane (2) for cerium in uranium as $\ln \gamma$ versus $1/T$ (Figure 6), the activity coefficient for cerium in pure uranium at 970°C can be estimated.

A least squares fit of the data yields $\ln \gamma_{\text{Ce}}^{\text{U}} = 2.266 + 2,406/T$ from which $\gamma_{\text{Ce}}^{\text{U}}$ at 970°C (1243°K) is found to be 66.8 (Table 7). Thus the activity coefficients of cerium in U-Cr eutectic are taken to be 69.6% of those for cerium in pure uranium.

One would like to be able to compare yttrium in U-Cr with this same method by assuming the differences in the solubility of yttrium in uranium and U-Cr are similar to those for cerium in uranium and U-Cr. This is not a valid assumption because cerium has a $+4$ valency and a much greater temperature coefficient of solubility in uranium (2) than yttrium. Cerium is a liquid above 798°C while yttrium is still a solid to 1526°C (37). Therefore, since cerium behaves different from yttrium in uranium, it would by comparison be expected to act differently in U-Cr too. The behavior of the two should be more similar than if a non-rare earth metal were compared with yttrium in the two solvents. Use of this correlation predicts a solubility of yttrium in U-Cr eutectic of 0.0494 wt.% at 950°C as seen from Table 7. This compares with 0.0292 wt.% for yttrium in super-cooled uranium at 950°C (Table 4).

Using Equation 25 one can analyze the solubility of yttrium in U-Cr and in UCr-Fe. To make the analogy requires one to assume that U-Cr and UCr-Fe eutectics act as pure components. Since a eutectic composition melts congruently, it exhibits characteristics of a compound or pure constituent. Hence, values for solubility parameters and molar volumes can be estimated by using weighted values of the pure elements.

The molar volumes for U-Cr and UCr-Fe can be determined from the densities and average molecular weights of the eutectics. Reference 53 lists a density of 17.3 g/cc for U-Cr at room temperature, and a density of

Table 7. Activity coefficients and solubility of cerium and yttrium in uranium and U-Cr eutectic

Temp. °C	Temp. °K	$\frac{1000}{T}$ °K ⁻¹	Solubility		Activity coefficients			Solubility	
			N_{Ce}^U wt.% Ce ^a	N_{Ce}^U at.% Ce	γ_{Ce}^U	γ_Y^U	$\gamma_Y^{UCr^b}$	$N_Y^{UCr^b}$ at.%	wt.%
1250	1523	0.6566	1.50	2.522	39.7	(281.1) ^c	195.7	0.511	0.226
1225	1498	0.6676	1.0	1.687	59.3	(311.7)	217.0	0.461	0.204
1200	1473	0.6789	1.15	1.938	51.6	(346.7)	241.4	0.414	0.183
1175	1448	0.6906	1.25	2.105	47.5	(387.1)	269.5	0.371	0.164
1150	1423	0.7027	1.16	1.955	51.2	(433.8)	302.1	0.331	0.146
970	1243	0.8045	(0.887)	(1.497) ^c	(66.8) ^c	(1131)	787.7	0.127	0.0560
950	1223	0.8177	(0.859)	(1.450)	(69.0)	(1281)	892.0	0.112	0.0494
850	1123	0.8905	(0.720)	(1.217)	(82.1)	(2543)	1770	0.0565	0.0249

^aData from Haefling and Daane (2).

^bEstimated from $\gamma_Y^{UCr} = 69.6\% \gamma_Y^U$: $\ln \gamma_Y^{UCr} = - \ln N_Y^{UCr} = - 0.906 + 9,416/T$ from data at 970°C of Voigt (52).

^cValues in parentheses are extrapolated from a least squares fit of data by Haefling and Daane: $\ln \gamma_{Ce}^U = 2.266 + 2,406/T$ or $\ln \gamma_Y^U = - 0.544 + 9,416/T$ (Figure 6).

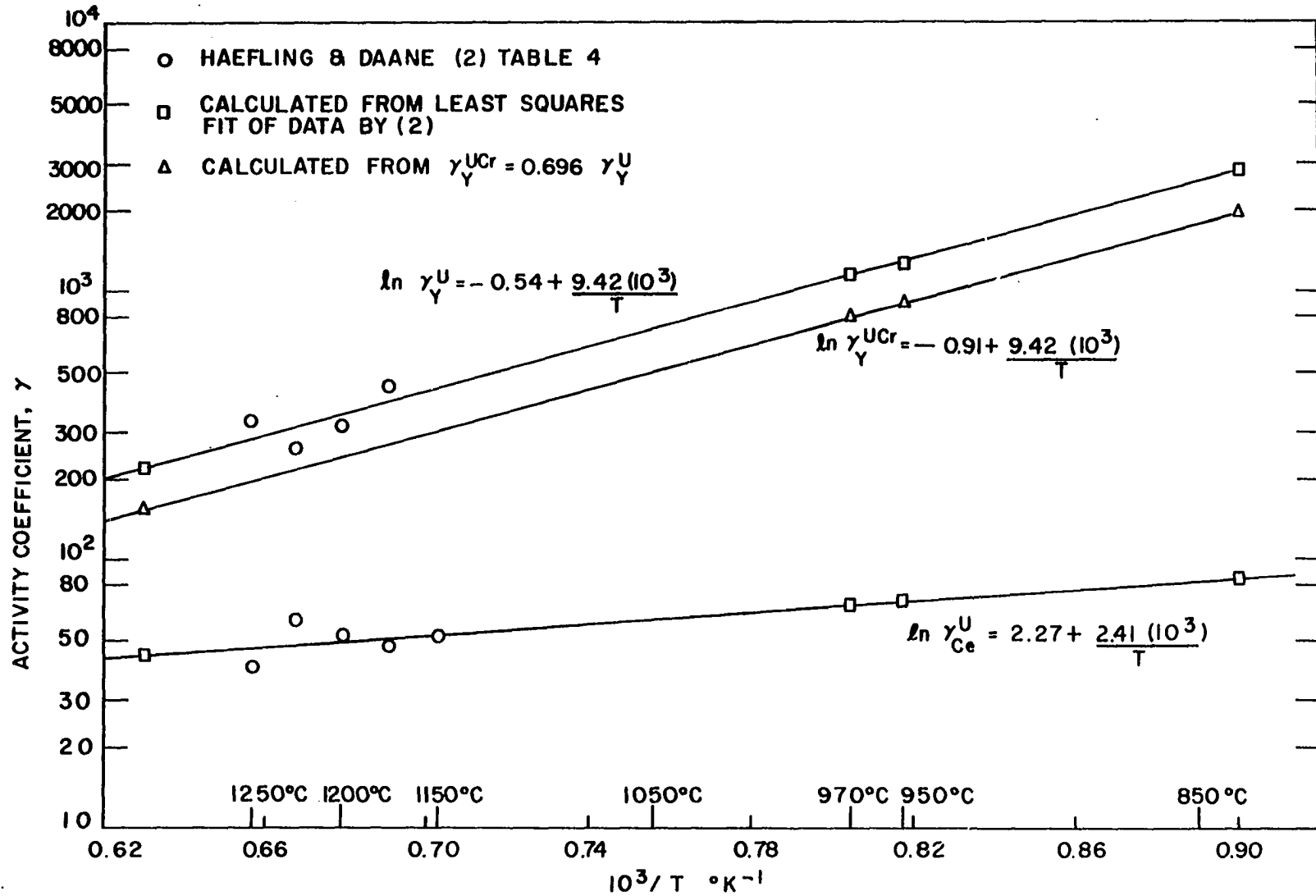


Figure 6. Activity coefficients (reciprocal mole fractions) of cerium and yttrium in uranium for predicting yttrium solubility in uranium-chromium eutectic

17.15 g/cc for a U-Cr eutectic that had been cast into iron tubes. Theoretically, using $\rho_U = 19.07$ g/cc, $\rho_{Fe} = 7.86$ g/cc, and $\rho_{Cr} = 7.19$, one gets $\rho_{UCr} = 17.6$ g/cc and $\rho_{UCr-Fe} = 17.4$ g/cc assuming no volume change upon mixing. McKee (54) lists the density of U-Cr eutectic at 0.985 the theoretical density, i.e. 17.35 g/cc. Applying this factor to the UCr-Fe eutectic yields 17.14 g/cc. These values will be used because they agree very closely with experimental values. The average molecular weight is determined by Equation 30,

$$\text{Ave. Mol. Wt.} = \frac{100}{\frac{\text{wt.\% U}}{238.03} + \frac{\text{wt.\% Cr}}{51.996} + \frac{\text{wt.\% Fe}}{55.847}} \quad (30)$$

Using the above densities and the average molecular weights, $V_{UCr} = 11.64$ cc/mole and $V_{UCrFe} = 11.48$ cc/mole.

Solubility parameters can be calculated with Equation 31 using the available heats of vaporization (28) and an atomic fraction weighting:

$$\delta_{UCr-Fe} = \left[\frac{.7775 \Delta H_U^V + .1873 \Delta H_{Cr}^V + .0352 \Delta H_{Fe}^V}{V_{UCrFe}} \right]^{\frac{1}{2}}, \quad (31)$$

where the value of RT at room temperature (592 cal/mole) is ignored because of the uncertainties in the published data for ΔH^V . Equation 31 yields $\delta_{UCr} = 101.2$ (cal/cc)^{1/2} and $\delta_{UCrFe} = 101.6$ (cal/cc)^{1/2}.

Table 8 lists the results of the calculations using Equation 25 for the solubility limits of yttrium in U-Cr and UCr-Fe eutectics at various temperatures. Again several successive trials were made to obtain the final estimates shown below the parentheses. It is seen from Tables 6 and 8 that on the basis of thermodynamic data of the pure constituents, Equation 25 predicts the following solubilities at 950°C: Y in U, 0.042

Table 8. Estimated solubility of yttrium in U-Cr and UCr-1.0 wt.% Fe eutectics predicted by Equation 25

Temp. °C	Temp. °K	RT cal/mole	^a AB ($\delta_Y - \delta_{UCr}$) ² cal/cc	$\ln \gamma_Y^{UCr}$	γ_Y^{UCr}	N_Y^{UCr}		^a AB ($\delta_Y - \delta_{UCrFe}$) ² cal/cc	$\ln \gamma_Y^{UCrFe}$	γ_Y^{UCrFe}	N_Y^{UCrFe}	
						at.%	wt.%				at.%	wt.%
850	1123	2232	894.01	(7.9908) ^a 7.9814	(2954) 2926	(0.0339) 0.0342 ^b	(0.0149) 0.0151	918.09	(8.2060) 8.1982	(3663) 3634	(0.0273) 0.0275 ^c	(0.0123) 0.0124
950	1223	2430	894.01	(7.3397) 7.3231	(1540) 1515	(0.0649) 0.0660	(0.0286) 0.0291	918.09	(7.5374) 7.5233	(1877) 1851	(0.0533) 0.0540	(0.0241) 0.0244
1050	1323	2629	894.01	(6.7841) 6.7571	(883.7) 860.1	(0.1132) 0.116	(0.0499) 0.0512	918.09	(6.9669) 6.9436	(1061) 1036	(0.0943) 0.0965	(0.0426) 0.0436
1150	1423	2828	894.01	(6.3068) 6.2658	(548.3) 526.3	(0.1824) 0.190	(0.0804) 0.0837	918.09	(6.4766) 6.4408	(649.8) 626.9	(0.154) 0.160	(0.0696) 0.0721
1200	1473	2927	894.01	(6.0934) 6.0440	(442.9) 421.6	(0.2258) 0.237	(0.0996) 0.105	918.09	(6.0508) 5.9988	(424.5) 402.9	(0.236) 0.248	(0.107) 0.112
1250	1523	3027	894.01	(5.8921) 5.8332	(362.2) 341.5	(0.2761) 0.293	(0.1218) 0.129	918.09	(6.0508) 5.9988	(424.5) 402.9	(0.236) 0.248	(0.107) 0.112

^aValues in parentheses are first trial results with $\phi^2 = 1$; values below are those obtained after 1 to 4 successive trials.

^bThe points fitted to Equation 12 by a least squares treatment yield: $\ln N_Y^{UCr} = 0.189 - 9,181/T$.

^cThe points fitted to Equation 12 by a least squares treatment yield: $\ln N_Y^{UCrFe} = 0.171 - 9,406/T$.

wt.%; Y in U-Cr, 0.029 wt.%; and Y in UCr-Fe, 0.024 wt.%. Equation 25 thus predicts the solubility of yttrium in uranium to be less than in either U-Cr or UCr-Fe. This contradicts the solubility predicted from a comparison with cerium in Table 7, from which it is seen that the solubility of yttrium in U-Cr eutectic is higher than in pure uranium.

Comparison of the various methods of estimating yttrium solubility in the three solvents, uranium, U-Cr, and UCr-Fe, is shown in Figure 7. Equation 25 shows the closest approximation to the actual values for yttrium in uranium. Since no published values are available for U-Cr and U-Cr-Fe eutectics, no comparison can be made for these systems.

It is surprising that the slope of the least squares treatment of the data by Haefling and Daane for yttrium in uranium agrees so closely with that predicted by Equation 25 and the comparison using cerium. This indicates that both methods are probably useful in predicting solubilities reasonably close to actual values. On the other hand, the predictions by Strauss *et al.* (46, 47) and Pasternak (45) are not accurate enough to be of much use for the systems mentioned here. As seen in the Results and Discussion, the solubility of yttrium in uranium was found to be less than in U-Cr eutectic at the same temperature. Thus, it would appear that the use of the cerium comparison is the most accurate method to predict the solubility of yttrium in U-Cr. This method is still based upon experimental data, however, and can only be used for comparison with U-Cr, whereas Equation 25 predicts the solubilities for all three systems with a fair degree of accuracy on the basis of thermodynamic data of the pure constituents alone.

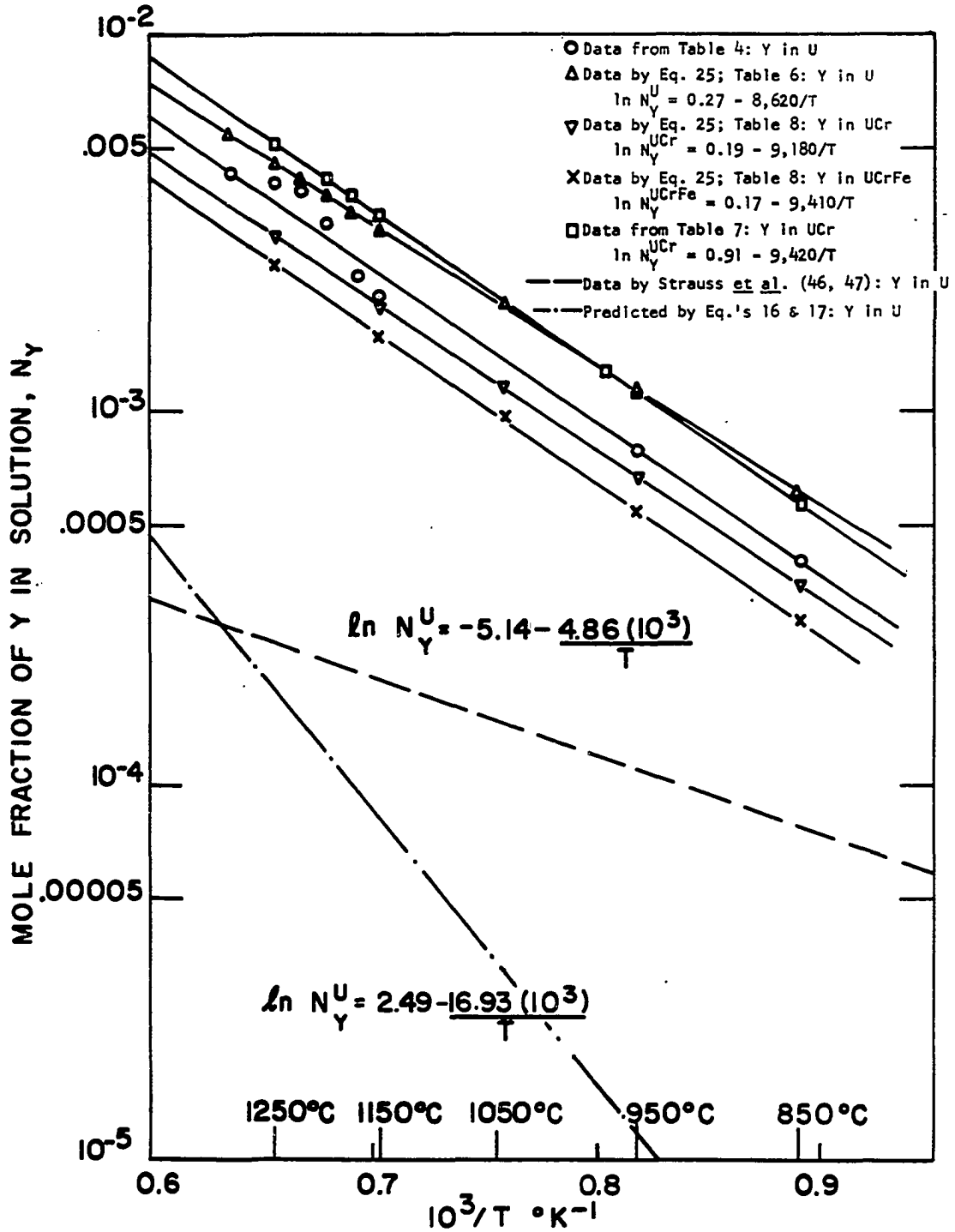


Figure 7. Comparison of yttrium solubility in uranium, uranium-chromium eutectic, and uranium-chromium-1.0 wt.% iron as predicted experimentally and theoretically

CORROSION BY LIQUID METALS

The process of liquid-metal corrosion, although by no means a phenomenon completely understood, can be simply defined as any interaction between a solid and a molten metal. It is generally agreed that there is no accompanying transfer of electrons as in the case of electrochemical corrosion. Often a weight gain or loss of the solid is associated with this interaction. For the purposes of this paper, the solid will be considered a metal in the form of a capsule as opposed to a metal coupon immersed in a liquid metal. Although liquid-metal corrosion is a poorly understood process, it is possible to classify the various types of corrosion phenomena which have been observed (1, 55, 56, 57, 58).

Liquid-Metal Corrosion Mechanisms

Liquid-metal corrosion occurs because of a thermodynamic imbalance at the interface between the liquid and solid metals. The driving force for the reaction is the tendency for the chemical potentials of the liquid metal and the solid metal to equilibrate. In any practical system, this is an impossibility in the strict sense of definition; thus, transfer of mass by several possible mechanisms is achieved. These types of interactions can be classified as follows:

- A. Dissolution of the solid metal into the liquid metal.
- B. Intermetallic compound formation by alloying between the liquid metal and the solid metal.
- C. Inward diffusion or intergranular penetration of the solid metal by the liquid metal.
- D. Impurity reactions.

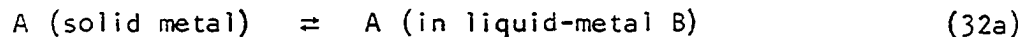
E. Dissimilar metal or concentration-gradient mass transfer.

F. Temperature-gradient mass transfer.

Corrosion can occur as a combination of one or more of the above mechanisms and becomes even more complicated if either the liquid metal or the solid metal is an alloy. Each of these corrosion interactions will be discussed in detail in the following paragraphs. Greater detail will be presented on the first three types since these were the only ones of concern in this investigation. The last three mechanisms are more important when studies involve dynamic conditions or different liquid-metal systems. Examples and photomicrographs of each type of interaction listed above are given in other references (6, 55, 57) and are not repeated here.

Dissolution of the solid metal into the liquid metal

For a two-component system of pure metals, the dissolution of solid metal (A) by liquid metal (B) can be represented by the reactions



or



where $A_{(B)}$ represents the dilute liquid solution of solid metal in liquid metal without the formation of intermediate phases. At constant temperature the process continues until the chemical potential of A is equivalent in both the solid and liquid phases. The rate of dissolution is governed by the solution rate at the solid-liquid interface and by the diffusion rate of the solute away from this stagnant boundary layer. Either of these steps can be the controlling factor as illustrated in Figure 8 (59). Diffusion-controlled liquid-metal corrosion (A) is observed in the vast majority of cases for metal systems as well as for aqueous and organic dissolution. On

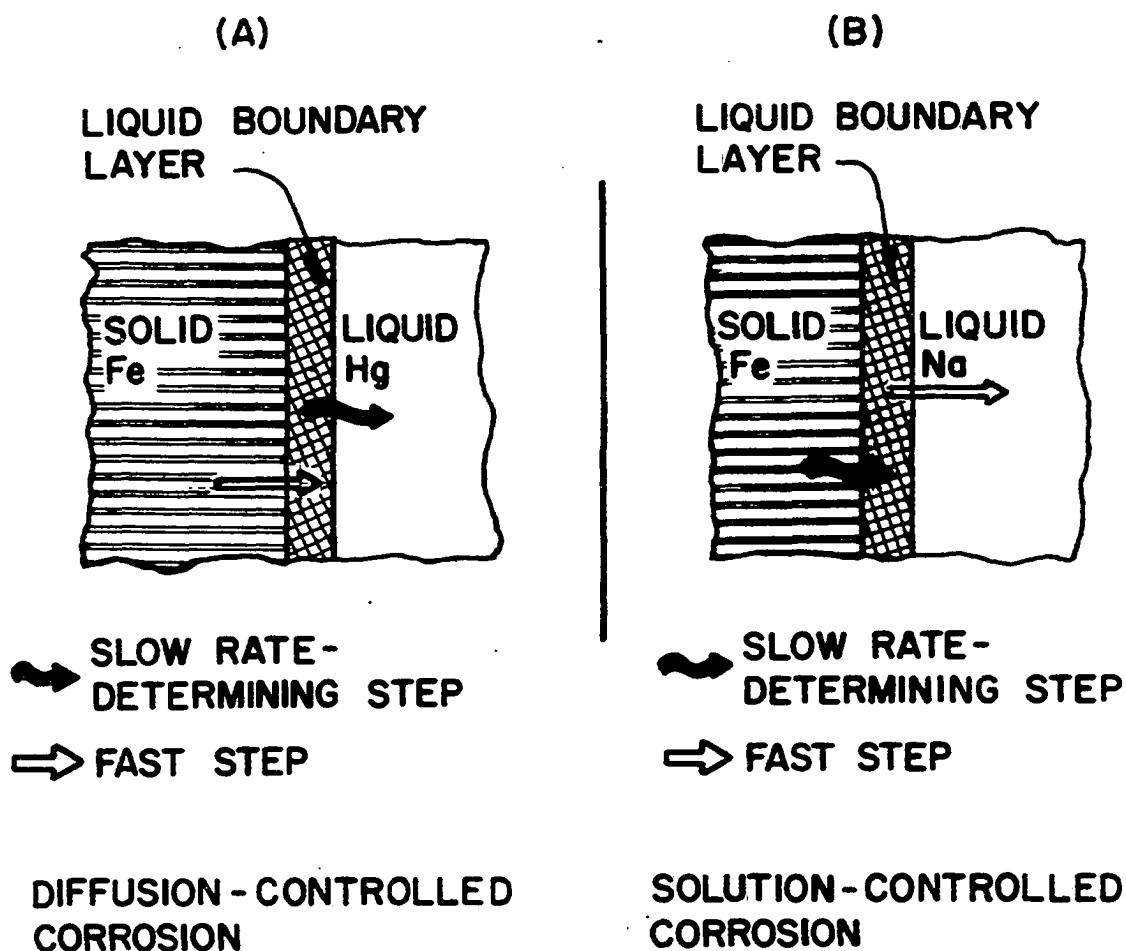


Figure 8. Dissolution of a solid metal into a liquid metal

the other hand, the solution-limited case (B) is rather rare. Epstein (59) lists the corrosion of iron by mercury to be Type A and the corrosion of iron by liquid sodium as Type B. Room temperature mercury passed over wetted iron attains its equilibrium solubility ($\sim 1\text{ppm}$) in a few seconds while iron in liquid sodium was found to require 2 hours or more to attain a saturated solution at 400°C . A third case exists where neither solution nor diffusion controls the dissolution; that is, the case where both processes occur at about the same rate. Such a situation has not been reported in the literature to the author's knowledge for any liquid-metal system.

The solution rate at the solid-liquid interface is dependent in part upon the solubility and the coefficient of solubility of the solid metal in the liquid metal. An atom of the solid metal dissolves in the liquid metal by breaking bonds with its neighbor like-atoms and forming new bonds with liquid-metal atoms. The amount of corrosion caused by this process could easily be predicted if adequate solubility data were always available and other variables could be held constant. Unfortunately, such information is lacking for most liquid-metal systems, and the magnitude and temperature coefficients of solubilities of solid metals in liquid metals cannot be predicted with accuracy by the present theories for liquid metals (60). However, static isothermal tests are usually sufficient for determining the extent of dissolutive attack for liquid-metal systems which exhibit this type of corrosion.

The diffusion rate from the solid-liquid interface, through the stagnant boundary layer and into the main body of liquid depends on the diffusion coefficient D . Diffusion occurs on an atomic scale and hence is governed by the structure of the liquid-metal solution. A number of theories on diffusion in liquids have been postulated, and several are presented in Appendix B of this paper.

Dissolution theory The kinetics of dissolution of a solid metal into a liquid-metal solution involves two rate processes: the rate at which atoms pass from the solid metal surface into the liquid layer immediately adjacent to the solid and the rate at which atoms diffuse from this stagnant interface layer into the bulk of the liquid. Noyes and Whitney were the first to present an expression for the rate of

solution of a solid in a liquid. The formulation may be derived in the following manner (61).

The rate of solution of the solid metal into the adjacent liquid layer can be expressed by the term $\bar{v}n_sA$, where \bar{v} is a frequency factor, n_s = the number of solid atoms per unit area of the solid surface, and A = the solid-liquid interface area. Opposing this is the rate of deposition of dissolved solid atoms back onto the solid surface from the adjacent liquid layer. This latter rate is assumed to be proportional to the interface surface area, A , and the concentration of the adjacent liquid layer. The net rate of solid-atom transfer to the liquid per second, therefore, is given by

$$\frac{dN}{dt} = \bar{v}n_sA - k_s nA, \quad (33)$$

where n = the concentration of solute in the solution (atoms/cc) and k_s = the proportionality solution-rate constant. When the solution becomes saturated, the net rate $\frac{dN}{dt} = 0$; thus

$$\bar{v}n_s = k_s n_0, \quad (34)$$

where n_0 = the saturation concentration of solute atoms (atoms/cc). If V = the volume of the solution (cm^3), then $N = nV$ where n = the concentration of the solute in the bulk of the solution (atoms/cc). From Equations 33 and 34,

$$\frac{d(nV)}{dt} = k_s A(n_0 - n) \quad (35a)$$

or

$$\frac{dn}{dt} = \frac{k_s A}{V}(n_0 - n). \quad (35b)$$

Integrating Equation 35b, with $n = 0$ at $t = 0$ and $n = n_t$ at any time t , produces

$$n_t = n_o [1 - \text{Exp}(-k_s A t / V)] \text{ atoms/cc-sec.} \quad (36)$$

One can also derive an expression in terms of a weight loss per unit time. The differential of Equation 36 is

$$\frac{dn_t}{dt} = \frac{n_o k_s A}{V} \text{Exp}[-k_s A t / V] \text{ atoms/cc-sec.} \quad (37)$$

Multiplying both sides by MV/N_o , where M = the molecular weight of the solute and N_o is Avogadro's number, gives the mass rate per unit time (g/sec) for solution,

$$\frac{dm}{dt} = \frac{n_o k_s A M}{N_o} \text{Exp}[-k_s A t / V] \text{ g/sec.} \quad (38)$$

Since $m = \rho_s A x$, where ρ_s = the density of the solute (g/cc) and x is the thickness (cm) of the layer of solid removed by dissolution, a measure of the rate of attack is

$$\frac{dx}{dt} = \frac{n_o k_s M}{\rho_s N_o} \text{Exp}[-k_s A t / V] \text{ cm/sec.} \quad (39)$$

This readily integrates to Equation 40 assuming $x = 0$ at $t = 0$,

$$x_t = \frac{n_o M V}{\rho_s N_o A} [1 - \text{Exp}(-k_s A t / V)] \text{ cm.} \quad (40)$$

The second process in the over-all rate of dissolution is the diffusion of solute atoms across the stagnant boundary layer of "effective" thickness δ as illustrated in Figure 9. In some cases (see Part B of this Section), compounds form in the liquid-metal solution, but still without altering the diffusion step.

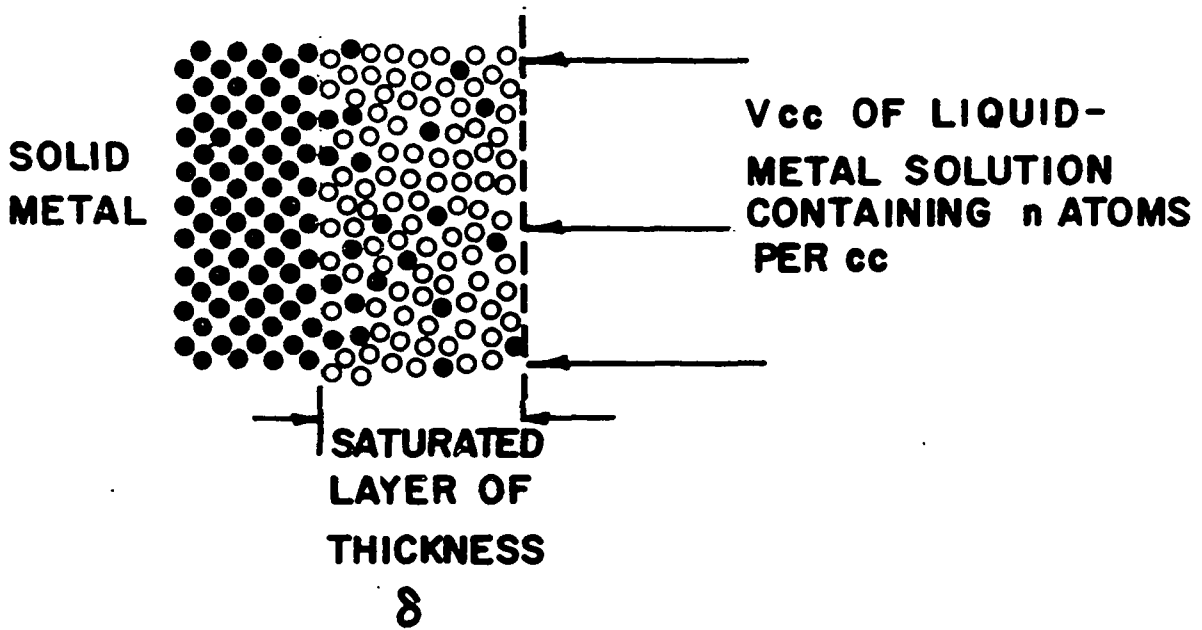


Figure 9. Representation of stagnant boundary layer of thickness δ

According to Fick's law, the number of atoms dN diffusing through the boundary layer in time dt across an area A (cm^2) is proportional to the concentration gradient $\frac{dn}{dz}$, or

$$dN = -DA \frac{dn}{dz} dt \quad (41)$$

where the proportionality constant D , is termed the diffusion coefficient (cm^2/sec). Since $n = N/V$ and $\frac{dn}{dz} = \frac{(n-n')}{\delta}$, where n' is the concentration of solute atoms in the diffusion layer,

$$\frac{dn}{dt} = \frac{DA}{\delta V} (n' - n). \quad (42)$$

If one assumes D to be independent of n , then Equation 41 yields, upon integration with $n = 0$ at $t = 0$,

$$\frac{D}{\delta} = \frac{V}{At} \ln \frac{n'}{n' - n_t} \quad (43)$$

or
$$n_t = n' [1 - \text{Exp}(-DA t / V \delta)] . \quad (44)$$

At the surface of the solid metal, the solution and diffusion rates are equal, thus combining Equation 35b and Equation 42 gives

$$\frac{dn}{dt} = \frac{k_s A}{V} (n_o - n') = \frac{DA}{\delta V} (n' - n) . \quad (45)$$

Hence,

$$n' = n_o \frac{k_s + (n/n_o)(D/\delta)}{k_s + (D/\delta)} \quad (46)$$

When the rate of passage of solid atoms into the diffusion layer is relatively fast, $k_s \gg D/\delta$; then $n' \rightarrow n_o$, that is, the concentration of solute atoms in the diffusion layer approaches the saturation value so that the net rate of dissolution is controlled by the diffusion process (Figure 8a). If the rate of solution of solid atoms into the diffusion layer is relatively slow, $k_s \ll D/\delta$, and $n' \rightarrow n$. Under that condition, the diffusion layer does not exist, and one has solution-controlled dissolution (Figure 8b).

Eliminating n' from Equations 45 and 46 results in a general expression for the net rate of dissolution,

$$\frac{dn}{dt} = \frac{k_s A (n_o - n)}{V [1 + k_s (\delta/D)]} \quad (47)$$

which integrates to

$$\ln \frac{n_o}{n_o - n_t} = \frac{k_s A t}{V [1 + k_s (\delta/D)]} \quad (48a)$$

or
$$n_t = n_o \left\{ 1 - \text{Exp}[-(k_s A t / V) / (1 + k_s \delta / D)] \right\} . \quad (48b)$$

This equation reduces to Equation 44 when $k_s \gg D/\delta$ or the rate-controlling step is diffusion through the boundary layer, and to Equation 36 when $k_s \ll D/\delta$ or the rate-controlling step is solution of the atoms across the solid-liquid interface.

As mentioned earlier in this Section if $k_s \approx D/\delta$, then neither step is rate-controlling and the general expression for n_t applies (Equation 48b). This case has not been observed for liquid metal dissolution. Using a dissolution-rate constant, α , Equation 48b reduces to

$$n_t = n_o [1 - \text{Exp}(-\alpha A t / V)], \quad (49)$$

where $\alpha = k_s$ (Solution-controlled), (50)

or $\alpha = D/\delta$ (Diffusion-controlled). (51)

The techniques for determining n_o , the saturation concentration, are well known and described in many sources. The experimental determination of α is usually accomplished by measuring n_t as a function of time at constant temperature. The slope of the curve obtained from a plot of $\log [n_o / (n_o - n_t)]$ versus t is $\alpha(A/V)$. The terms n_t and n_o can represent any appropriate measure of concentration, such as atoms/cc, g/cc, ppm, etc., as long as the two are consistent.

Dissolution can occur under two conditions: 1. the static case where the body of liquid metal in contact with the solid metal is quiescent and 2. the dynamic case where there exists a relative velocity, v , between the bulk of the liquid metal and the solid metal surface. Under dynamic conditions it is usually easy to determine which step in the dissolution process is rate controlling. Epstein (62) and others have observed that in solution-controlled dissolution, the dissolution rate constants were

independent of velocity; but for diffusion-controlled dissolution, α increased with velocity, usually linearly (62, 63, 64, 65).

The static case of dissolution presents more of a problem to determine which step is rate controlling. The dissolution-rate constant is usually found to be temperature dependent according to an Arrhenius-type expression

$$\alpha = \alpha_0 \text{Exp}[-\Delta E/RT], \quad (52)$$

where ΔE can be taken as the over-all activation energy for the dissolution process. The slope of a plot of $\ln \alpha$ versus $1/T$ yields an experimental value for ΔE which can be compared with relative values of solid-liquid interfacial tension, if such data exist for the systems of interest. This follows if the activation energy for dissolution is regarded as a measure of the energy barrier to a solid-metal atom passing from the bulk of the solid through the interface into the liquid metal, and if the interfacial tension is assumed to be a measure of this energy barrier. Because values for interfacial tensions are scarce for liquid-metal systems, it is probably easier to determine if the dissolution process is diffusion controlled for the static test case.

For the latter situation, $\alpha = D/\delta$, and usually δ is found to be independent of temperature whereas D is not. Therefore, by knowing D and α at various temperatures, a comparison of δ with temperature should yield almost constant values. Epstein (62) shows α to be given by a two parameter equation of the form

$$\ln \alpha = a - b/T, \quad (53)$$

which is equivalent to Equation 52. Ward and Taylor (64) found α to be independent of temperature, but their data were taken at two temperatures

only 50°C apart. Hence, their conclusion was not well corroborated.

It is possible to arrange Equation 49 to yield an expression independent of α , A, and V, which is obeyed for all dissolution data at any temperature and under static or dynamic conditions (64). Let $n_x = (x)(n_o)$ where x is any fraction less than unity, and $t_x =$ the time for n_t of Equation 49 to reach the concentration n_x . Therefore, by Equation 49

$$n_x = n_o [1 - \text{Exp}(-\alpha A t_x / V)] = x n_o \quad (54)$$

and

$$1 - x = \text{Exp}(-\alpha A t_x / V). \quad (55)$$

Taking the natural log of both sides, one can solve for

$$\alpha A / V = -(1/t_x) \ln(1 - x). \quad (56)$$

Substituting Equation 56 into Equation 49 with $n_o = n_x/x$ yields

$$n_t / n_x = (1/x) \left\{ 1 - \text{Exp}[(t/t_x) \ln(1 - x)] \right\}. \quad (57)$$

Being independent of geometry, Equation 57 as a general expression can be used to extrapolate concentration-time relationships from limited experimental data.

Corrosion engineers usually express the results of experimentation in terms of a corrosion rate

$$R = \Delta W / At \quad (\text{g/cm}^2\text{-sec}), \quad (58)$$

where ΔW is the total change in weight of a specimen of area A exposed to the liquid metal for a time t. ΔW can also be thought of as the weight of solute in solution that contacted area A of solid metal. A mass balance with Equation 49 shows that

$$\Delta W = -n_t V, \quad (59)$$

the minus sign indicating a weight loss of solid metal. Thus,

$$R = -(n_0 V/At)[1 - \text{Exp}(-\alpha At/V)] \text{ g/cm}^2\text{-sec.} \quad (60)$$

If the corrosion experiment is carried out to saturation; that is, $t \gg V/(\alpha A)$, then Equation 60 reduces to

$$R \cong -(n_0 V/At). \quad (61)$$

Up to this point, details about the diffusion coefficient, D , have not been mentioned. It has been seen that for both static and dynamic dissolution processes that are diffusion-controlled, the dissolution-rate constant, α , is equal to D/δ . Almost all liquid-metal systems studied from a dissolution standpoint are found to be diffusion controlled (66); hence the need to determine D .

The diffusion of molecules and ions in aqueous or organic solvents has been studied extensively for many years. In the case of liquid metals, however, there is a deficiency of information on diffusion coefficients. This is caused by the experimental difficulties encountered in determining liquid-metal diffusivities and by a lack of reliable theories to account for the phenomenon of liquid diffusion.

In papers on diffusion in liquid metals, Pasternak and Olander (67) have compared two methods of determining mutual diffusion coefficients in dilute solutions. The first method is a modification of Eyring's absolute-rate theory, and the second is an application of the principle of corresponding states by Thomaes and Itterbeek (68). The absolute-rate method requires only pure component viscosity and density data which are usually available or which can be estimated by various correlations where data are lacking (69, 70). The corresponding-states method, on the other hand,

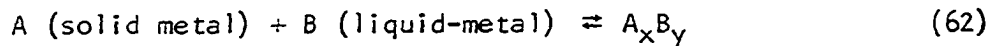
requires partial molar heat of mixing data, which may not be available for the systems of interest. This is certainly the case for the Y-UCr and Y-UCrFe systems. The accuracy of both methods is about the same, and since the method based on absolute-rate theory requires only pure component data, it is the simpler of the two methods and can be applied to more systems. Hence, this method will be used in this investigation to calculate the diffusion coefficients for the systems of concern. This has been done in Appendix B.

It must be noted here in closing on dissolution theory that when the solid-metal container is an alloy, the over-all dissolution process becomes considerably more complicated. Each alloy constituent will exhibit a different solubility and a different coefficient of solubility in the liquid metal. Likewise, the diffusion coefficients for each element in the liquid-metal solution will be different and each element of the alloy will be seeking an equilibrium value. Further complications are involved when intermetallic compounds are formed between the liquid metal and one or more of the alloy constituents, as discussed in the next section.

Intermetallic compound formation

Type A liquid-metal corrosion consists of solution of the solid metal into the liquid metal followed by diffusion of the solute atoms across a stagnant boundary layer of thickness δ into the main body of the liquid metal. No other reactions occurred in the dissolution process and only two species were present.

In Type B corrosion considered here, dissolution corrosion must first appear followed by a reaction leading to one or more intermetallic compounds at the interface region. A reaction for this type of liquid-metal corrosion can be represented by the following equation:



where $A_x B_y$ is an intermetallic compound consisting of x atomic parts of A and y atomic parts of B . Metallographic examination, X-ray diffraction analysis, and hardness testing are three methods of determining intermetallic compound formation. In addition, phase diagram information is often available (8, 9).

For continued corrosion to occur by this process, the solution of A atoms into B must proceed followed by diffusion through the intermetallic compound layers. Likewise, liquid-metal B atoms must diffuse from the bulk of the liquid through the compound layers in order to cause solute atoms to dissolve. Usually the diffusion coefficients will be different for the two processes.

Here again, the rate of growth of the compound layers is governed either by the solution rate or by the diffusion processes. If solution controlled, the rate of growth (thickness) of the intermediate phases will be very slow until the liquid solution has progressed well towards equilibrium, at which time the thickness increase will be governed by the reaction rate of compound formation. If the growth of the compound layers is controlled purely by diffusion, as is usually the case (71), the increase in thickness should follow a parabolic law,

$$x^2 = k't \quad (63)$$

where x is the thickness of the intermetallic phase after time t and k' is the parabolic rate constant at the temperature of interest. It is assumed that the layer is coherent and does not tend to break up and float away from the interface region.

It is important to note that when pure metals are involved, intermetallic compound formation must continue until one phase (either A or B) has disappeared as dictated by the phase rule. Thus equilibrium can not be obtained in a binary system undergoing Type B corrosion unless diffusion through the intermetallic phases is halted by some physical barrier. Since diffusion is a rather slow process, intermediate phases of constant composition might possibly furnish the necessary barrier. At best, however, the diffusion process would probably continue at an infinitesimal rate.

The amount of the original solid metal which goes into true solution in the liquid metal will naturally depend upon the volume of liquid present (see Type A corrosion) but the growth rate of the intermetallic phases should be independent (or nearly so) of this volume (71).

Because a true equilibrium cannot be obtained in systems which form intermetallic compounds, these systems are unlikely to be of interest in circumstances demanding a very high corrosion resistance. Even if the intermetallic compounds form coherent layers in the interface region, reduced corrosion attack still continues because of diffusion through the layers. The formation of intermetallic compounds is usually associated with appreciable solubility of the solid in the liquid metal. Unfortunately there is no satisfactory theory from which the formation of intermetallic compounds can be predicted.

Sauerwald et al. (23) classified systems of binary alloys which exhibit intermetallic compounds (V systems) as a special group, just as they did the miscibility gap systems discussed earlier. The "V systems" show strong linkages between unlike atoms which cause preferential short range order. As expected this group of systems exhibits peculiarities in thermodynamic and other physio-chemical properties. When atoms of elements in V systems have only slight affinities, their behavior approach those of the L systems (systems showing no peculiarities). The following properties are characteristic of intermetallic (V) systems:

1. The phase diagram should exhibit congruent intermetallic compounds.
2. The heat of mixing (ΔH_{mix}) is large and exothermic, ranging from -500 to $> -10,000$ cal/mole.
3. The excess entropy (ΔS^{XS}) is positive and varies from 0 to 3.0 cal/mole $^{\circ}K$.
4. The free energy of mixing (ΔF_{mix}) is large and ranges from -1500 to 9000 cal/mole.
5. The activity of these systems shows a negative deviation from the ideal.
6. X-ray data show short range ordering.
7. A change in volume is to be expected of up to 30% upon mixing.
8. Viscosities values will show extremes and points of inflection as the system composition changes.

In this investigation only the Fe-Y system exhibits compound formation (Figure 4). Iron also forms two intermetallic phases with uranium (Figure 2), which tends to limit the extent of possible formation of

Fe-Y compounds. A quaternary system such as UCrFe in yttrium is greatly complicated from this standpoint. It is possible that diffusion barriers might be formed as mentioned above.

In almost all cases the intermetallic compounds formed in Type B corrosion have higher melting points than liquid metal B. Thus the layer formed adjacent to solid metal A will be a solid at the temperature of interest.

In all systems the liquid has a certain solubility in the solid, and no matter how slight there must always be some diffusion into the solid with the subsequent formation of a solid solution (just as in Type A corrosion). However, the term "intermediate phase" is not applied to a solid solution whether compounds are formed below the original surface or not. This type of inward diffusion, if it does not occur along grain boundaries, involves only several atomic layers. Diffusion along grain boundaries can proceed to a much greater depth and will be discussed under Type C corrosion. In most systems investigated with high corrosion resistance, the solid solubility is usually very slight and signs of a solid solution are not generally detectable (71).

From the correlation by Mott (39) it is seen that when $k < 2$, bonding between A-B atoms is stronger than between A-A or B-B pairs. This is exactly what happens when intermetallic phases are formed, A-B type bonds predominate. According to Pauling (72), the differences in electronegativities for two elements is an indication of the strength of bonding between the two: the larger the electronegativity difference, the stronger the bond. Of the four elements of concern in this study (Table 2), iron and yttrium have the largest electronegativity difference (0.53 eV). From this

viewpoint some intermetallic phase formation would be expected, but one must also look at the large differences in atomic diameter (2.54 Å for iron versus 3.606 Å for yttrium) and the solubility parameters (118.2 for iron vs. 71.3 for yttrium). These latter two factors tend to override the formation of an intermediate phase. Mott's value of k from Table 3 for Fe-Y is 3.8 whereas k for U-Cr, which exhibits no intermediate phases, is -1.0. U-Fe, which has two intermetallic compounds, has a $k = -0.4$. As seen in Figure 4, the four Y-Fe compounds which are possible occur on the iron-rich side of the phase diagram probably because of the large atomic size difference. Thus a predominance of iron is necessary before compound formation can occur. In the UCr-1.0 wt.% Fe system of interest in this study, yttrium atoms available for reaction would outnumber the amount of iron present. Hence, little intermetallic compound formation should be found in the UCrFe-Y system.

The use of an alloy container with one or more constituents which can form intermetallic compounds with the liquid metal again complicates the situation. Exactly what might happen cannot be predicted by theory and even phase diagram information may be of little help. Instead of increasing corrosion an alloy might show higher corrosion resistance than any of its pure constituents.

An alloy which exhibits intermetallic compounds among its own constituents may show better corrosion resistance towards the liquid metal (with which it does not form compounds) than the pure constituents do. Weeks and Gurinsky (73) cite such cases for lead in alloys with intermetallic compounds. Alloys in which no compound formation occurred showed relatively

lower resistance to mass transfer. In general, however, if the liquid metal forms a compound with one of the alloy constituents, corrosion attack of a noticeable degree would be expected. Whether it would be enough to prohibit the alloy's use for a container could only be determined by actual experimentation.

In summary, Type B corrosion attack occurs through the formation of new solid intermetallic phases between the liquid and solid metals. This corrosion is also accompanied by dissolution and diffusion processes. When solubility in the liquid is high, the increase in thickness of the intermediate layers is delayed until the liquid approaches its equilibrium solubility. Subsequently, new phases become thicker because of diffusion of solid and liquid atoms through them. The rate of growth usually decreases with time. A consequence of this type of corrosion, barring the interruption of diffusion, is that attack must continue until either the solid or liquid has completely transferred to a new phase. In particular instances, the intermetallic phases are not coherent but tend to break away forming a suspension. This results in an increased rate of corrosion attack. If a solid alloy contacts the liquid metal, the situation becomes more complicated although less attack could possibly occur. Only experimental tests will give the answer to what to expect.

Intergranular penetration of the solid metal

When liquid-metal atoms are capable of penetrating the boundaries between individual grains of a solid metal, any of three possibilities can occur: 1. The liquid-metal atoms can penetrate the entire thickness of the solid. 2. Dissolution attack can occur between the grains which will

enlarge the boundary area and produce further attack. 3. Dissolution occurs followed by the formation of intermetallic compounds between grains. All three processes involve diffusion of liquid-metal atoms from the bulk of the liquid into the solid-metal grain boundaries. Stress corrosion occurs in the same manner for stressed solid metals by causing embrittlement along the grain boundaries.

If a metal is heated several hundred degrees above room temperature, the surface regions intersected by grain boundaries will attain an equilibrium structure by surface diffusion. At the site of each grain boundary a slight groove is formed as shown in Figure 10; this phenomenon is referred to as thermal grooving (74). The surface tensions, γ , soon reach

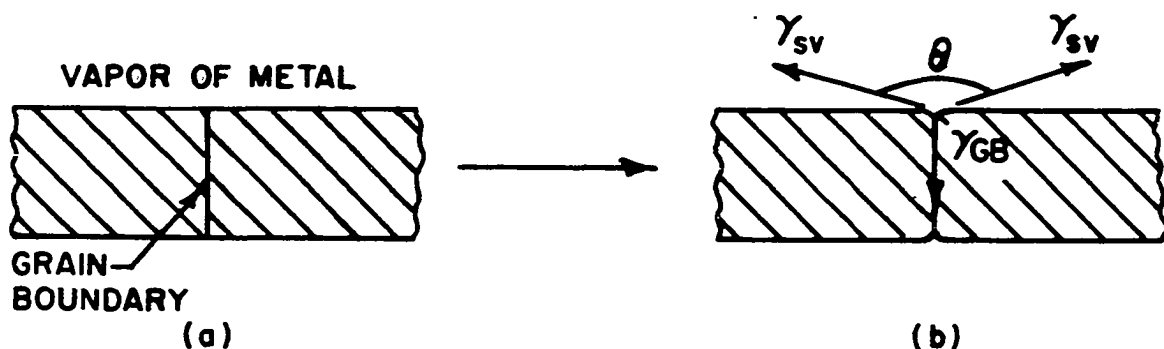


Figure 10. Thermal grooving of metal surfaces at elevated temperatures

equilibrium and by Smith's equation (75)

$$\cos \theta/2 = \gamma_{GB}/2\gamma_{SV} \quad (64a)$$

or

$$\cos \theta/2 = \gamma_{GB}/2\gamma_{SL} \quad (64b)$$

where γ_{GB} is the surface tension (interfacial energy) of the grain boundary, γ_{SV} is the solid-vapor surface tension, and γ_{SL} is the solid-liquid surface tension when the surface is contacted by a liquid metal. The angle, θ , is

referred to as the dihedral angle or the groove angle. Likewise, when a metal surface is exposed to a liquid metal at elevated temperatures, similar thermal grooving may occur, but the groove angle is usually smaller and may be zero. This is represented in Figure 11.

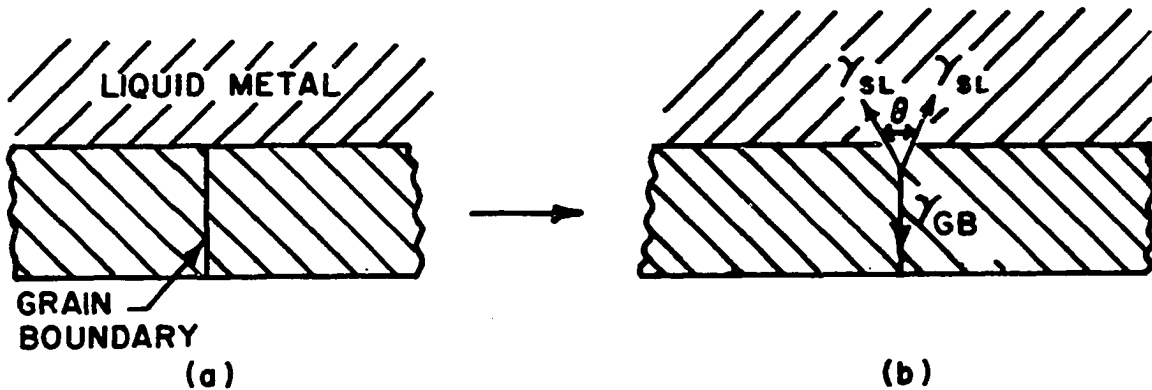


Figure 11. Schematic presentation of surface tension effects in grain boundary penetration

In the example illustrated in Figure 11b, the groove angle $\theta > 0^\circ$, so that $\gamma_{GB} < 2\gamma_{SL}$ by Equation 64, and the surface tensions are in equilibrium. Such a configuration creates a stable liquid-solid geometry, and the liquid will not penetrate the grain boundary. If however, $\theta = 0^\circ$, then $\gamma_{GB} \geq 2\gamma_{SL}$, and surface tension equilibrium is not attainable. Thus, the liquid penetrates the grain boundaries and destroys the adhesion between grains. This is the case for complete grain-boundary filming by the liquid.

The above two examples are actually observed in the Cu-Pb and Cu-Bi systems, respectively. Molten lead at 900°C does not embrittle copper, but bismuth at the same temperature rapidly penetrates the copper grain boundaries and destroys its mechanical strength. This type of attack is easily detected by tensile testing or bending tests. Figures 12a and 12b, drawn

from photomicrographs of Smith (75), show that for Cu-Pb the groove angle is stable ($\sim 60^\circ$); but for Cu-Bi the groove angle is approximately zero, and grain boundary penetration occurs.

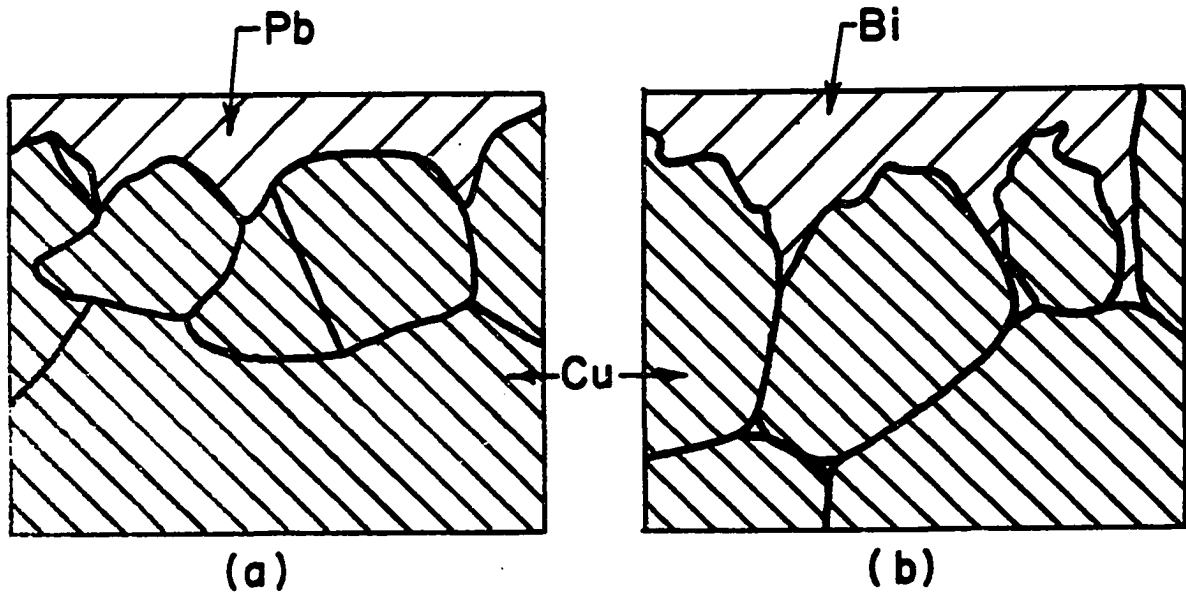


Figure 12. Grain boundary grooves for (a) Pb + Cu and (b) Bi + Cu

A third case is illustrated in Figure 13 where

$$\gamma_{GB} < 2\gamma_{SL} < 1.6\gamma_{GB} \quad (65)$$

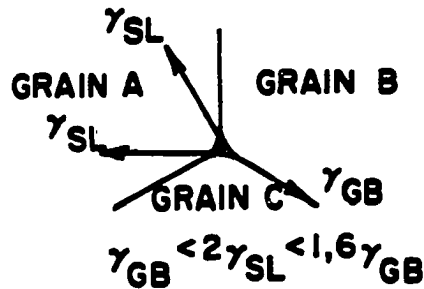


Figure 13. Intergranular penetration into a triple grain intersection

Under these conditions, the liquid metal can penetrate triple grain intersections and diffuse through the metal by flowing along these channels (76). As γ_{SL} approaches γ_{GB} , the stable liquid-phase geometry progresses through the channel configuration to a complete boundary film at $2\gamma_{SL} \leq \gamma_{GB}$ (Figure 12b). Thus, to prevent this type of intergranular penetration requires that $2\gamma_{SL}$ must be greater than $1.6\gamma_{GB}$.

The dihedral angle is of primary importance in connection with the penetration of a liquid metal into a solid metal. If the solid metal is slightly soluble in the liquid, it will dissolve most rapidly at the grain boundaries. When θ is greater than zero, penetration will cease as soon as the groove angle is reached, and further dissolution attack must occur under conditions that sustain this angle. If, however, the dihedral angle is zero, intergranular penetration proceeds continuously and the liquid metal is carried in by capillary action. This results in a prying apart of the grains and inexorable disintegration of the solid. Such action is intensified when a stress is present; in fact, a tensile stress can probably cause penetration even when θ is somewhat greater than zero.

If the surface tensions of the pure constituents of a liquid-metal corrosion system are known or can be estimated, it is possible to predict theoretically if grain-boundary penetration will occur. Good (74) gives the following equation relating the three surface tensions:

$$\gamma_{SL} = \gamma_{SV} + \gamma_{LV} - 2\phi \sqrt{\gamma_{SV} \gamma_{LV}} \quad (66)$$

where

$$\phi = \frac{4(V_1 V_2)^{\frac{1}{3}}}{[(V_1)^{\frac{1}{3}} + (V_2)^{\frac{1}{3}}]^2}, \quad (67)$$

γ_{LV} is the surface tension of the liquid metal in contact with its vapor, and V_1 and V_2 are the molar volumes of the pure constituents at the temperature of interest. Using Equation 64b the dihedral angle θ can be calculated if γ_{GB} is known for the solid metal of interest. Otherwise, actual measurements of the angle from microstructure are necessary. There is apparently no theory applicable for the calculation of γ_{GB} , which must be determined experimentally. Since γ_{GB} is not known for yttrium, it is not possible to calculate a value for the dihedral angle θ and thereby determine if grain-boundary penetration occurs without measuring γ experimentally. Also γ_{SV} for yttrium has not been determined and the method of Grosse (77, 78, 79) is not applicable for solid-vapor surface tensions. A fair approximation of γ_{SV} , however, can be made by assuming $\gamma_{SV} \approx \gamma_{LV}$ for supercooled yttrium at 950°C and using Equation 66 and Grosse's method to obtain γ_{SL} . γ_{SL} can also be estimated from Equation 68 as shown by Weeks (80).

When there is a large difference in atom size or if the two metals are immiscible, Smith states that the interfacial tension, γ_{SL} , can easily exceed half of that for γ_{GB} . Such is the case for uranium and yttrium; hence grain boundary penetration would not be expected for this system.

Weeks (80) has related γ_{SL} to the partial molar enthalpy, $\bar{\Delta H}$, associated with the transition of atoms from the pure solid into liquid solution by Equation 71,

$$\bar{\Delta H}/\gamma_{SL} \approx K \approx V/d, \quad (68)$$

where V is the molar volume and d is the closest approach of atoms for the solute. The value of $\bar{\Delta H}$ is calculated from the solubility curve after a method by Kleppa and Weil (81) as shown for the U-Y system in Appendix A.

According to Weeks, a low value of $\Delta\bar{H}$ (< 10 Kcal/mole) may be associated with grain-boundary penetration. From Figure 5 $\Delta\bar{H}$ for yttrium in uranium is 18.7 Kcal/mole, or considerably above that where penetration should occur.

Once the liquid metal has penetrated the grain boundary the processes of dissolution and/or diffusion will occur unless suitable impurities capable of lowering the surface energy γ_{GB} are segregated in the grain boundaries. The specific case of diffusion in grain boundaries has been adequately handled with mathematical models using Fick's law by Fisher, by Whipple, and by Suzuoka (82). Details will not be presented here because the equations and derivations are rather involved but are found in References 82 and 83.

If grain-boundary attack occurs, there are several possible ways to alter the surface energies attributing to the penetration. One can try to increase the solid-liquid interface tension, γ_{SL} , by impurity additions to the liquid metal. Those impurities which lower surface energy will tend to segregate to the surface by Gibbs Adsorption Isotherm (76) and possibly block entrance of the liquid metal into the grain boundaries. However, if a given liquid metal composition must be maintained, this method can not be used, and the only variable which can be changed is γ_{GB} . By adding certain impurities to the solid-metal matrix, it may be possible to lower the grain-boundary surface tension such that

$$2 \gamma_{SL} > 1.6 \gamma_{GB} \quad (69)$$

Upon the addition of such impurities, γ_{GB} is lowered or impurity particles precipitate in the grain boundaries to block intergranular penetration as shown in Figure 14. The precipitate particle B creates two new surfaces

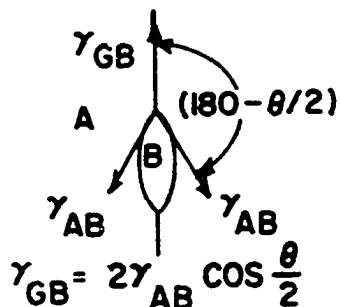


Figure 14. Schematic presentation of surface tension effects with grain boundary precipitates

each with a unit surface tension of $\gamma_{AB} < \gamma_{GB}$. Thus, if

$$\gamma_{AB} < 2 \gamma_{SL} < \gamma_{GB}, \quad (70)$$

the precipitate prevents liquid penetration by a "blocking" effect.

For a given solute, the tendency for grain-boundary segregation is given by the degree of lattice solubility of the solute in a given solvent. Large solubility produces only slight segregation because of the ease of accommodating a solute atom at a lattice boundary imperfection. But, elements which exhibit low solubility will tend toward large equilibrium segregations (84). In the case of yttrium, the elements carbon, nitrogen, and oxygen all form one or more intermetallic phases, but nitrogen is apparently the least soluble of the three, ~ 600 ppm at 1525°C (6). Therefore, if intergranular attack occurs in yttrium with the liquid-metals studied in this investigation, nitrogen additions to the yttrium matrix should tend to reduce γ_{GB} .

Eldred (71) states that the solid-metal grain boundaries are usually unwetted when the mutual solubility of the solid and liquid is low,

because γ_{SL} tends to be high for these systems. Such is the case with the metals studied in this investigation; therefore little, if any, intergranular penetration is to be expected.

In summary, intergranular corrosion attack can be expected to occur whenever the grain-boundary interfacial energy, γ_{GB} , is greater than twice the solid-liquid interfacial energy, γ_{SL} . (In the case of a triple grain intersection, $1.6 \gamma_{GB}$ need be only greater than $2 \gamma_{SL}$.) Once penetration occurs, the process of dissolution and/or diffusion continues with the possibility of forming intermetallic phases in the boundaries. In some cases, such as zinc in molybdenum, the liquid metal will simply diffuse through the grain boundaries causing little structural damage (26). If surface tensions for the solid, liquid, and grain boundaries are known, the dihedral angle can be estimated, thus predicting whether penetration will occur. In general, systems exhibiting very low mutual solubilities will not be expected to undergo intergranular penetration.

Impurity controlled corrosion

In any given corrosion system involving even the purest of metals, there will always be the presence of some impurity atoms in both the liquid and solid metals. In most cases the metallic impurities are of little concern unless present in significant amounts, whereas the non-metallic impurities such as carbon, oxygen, and nitrogen can play an important roll in the over-all performance of the system. The impurity reactions are probably the least understood of the various types of corrosion mechanisms. For alkali metals these impurities, especially oxygen, have an important and often dominating influence on corrosion processes. In other metallic

systems, the impurities are usually not dominating but, nevertheless, important. Sometimes the whole mode of attack can be changed because of the effect of the impurity on the surface tensions (grain-boundary attack) or because of the activity of the impurity.

Depending on the particular system of concern, impurities can either increase or inhibit corrosion. For alkali metals, the presence of oxygen usually accelerates corrosion (85), but with liquid lead the rate is decreased (57). In some systems additions of titanium or zirconium will tend to form protective carbide, nitride, and oxide layers which inhibit dissolution or intergranular penetration. These additions are especially helpful in preventing corrosion by liquid bismuth (73).

Both uranium and yttrium have large affinities for oxygen, nitrogen, and carbon. Oxygen is particularly difficult to remove as an impurity because the solubility is so high. Thus in any U-Y system, the oxygen will be an interstitial impurity which will redistribute itself between the metals by partitioning to achieve equilibrium. Formation of an oxide film on the interface at elevated temperatures is highly unlikely because of the increased solubilities of oxygen in both metals. Nitrogen, hydrogen, and carbon are less soluble than oxygen and will also tend to redistribute themselves between the two metals; all four impurities form at least one or more compounds with the two metals. Thus, the formation of a film at the interface is improbable. Because uranium, yttrium, titanium, and zirconium have similar affinities for these impurities the latter two metals will not be helpful as corrosion inhibitors.

One possible corrosion inhibitor is a layer of carbide on the inner surfaces of yttrium. Los Alamos Scientific Laboratory has had considerable

success in containing molten plutonium fuels in tantalum by this means (76, 86). Also, the Ames Laboratory had some degree of success in the mid 1950's with tantalum carbide layers in preventing corrosion attack by the U-Cr eutectic (87, 88).

In conclusion, the presence of impurities in the liquid and solid metals may give rise to Type D corrosion attack. Oxygen is usually the impurity of special interest, but others such as carbon, hydrogen, and nitrogen may produce similar effects. Metallic impurities are usually not of a corrosion-controlling nature unless present in significant amounts. Systems which can form a layer at the solid-liquid interface may increase corrosion, especially if it is non-coherent, breaks up, and passes into the liquid. On the other hand, inhibitive films may be formed which protect the solid surface from attack that might otherwise occur by direct contact with the liquid metal.

Dissimilar-metal mass transfer

When two or more solid metals or alloys are contacted by the same liquid metal, the liquid metal may act as a carrier for transporting atoms from one solid metal to the surface of the other solid metal. This type of mass transfer typically occurs by dissolution of the one solid by the liquid metal followed by a second interaction between the dissolved metal with the second solid metal to form an intermetallic compound. Considerable transfer may occur even though the individual solubilities of the two solid metals in the liquid are quite small. This type of corrosion does not require a dynamic system or a temperature gradient but may occur in a static, isothermal test involving a metal coupon suspended in a

capsule of a different metal. Experimentally the migration through the liquid metal has generally been in one direction only.

The driving force for this process is simply the thermodynamic requirement that the chemical potential (partial molar free energy) of each element be in equilibrium in all phases that are in contact. Both temperature and the solubilities of the two metals will affect the rate of reaction and extent of mass transfer. Even if intermetallic compounds are not formed in the ternary system, alloying will occur to make both solid-metal surfaces equivalent alloys. Sometimes a dissolved metal inhibitor such as titanium or zirconium will deposit on the surface of one of the solid metals.

This type of mass transfer also occurs with the non-metallic impurities when both solid metals or alloys are essentially insoluble in the liquid metal. Gettering of oxygen, nitrogen, carbon, and hydrogen in the alkali metals, or bismuth and lead containing titanium or zirconium are classic examples. Titanium or zirconium additions are sometimes deemed advisable in order to prevent the exchange of non-metallic impurities which could cause embrittlement, decarburization, etc. of one of the solid metals or alloys.

As now envisioned by Los Alamos Scientific Laboratory and others (89), molten fuel in a reactor core would be encapsulated in long circular fuel pins approximately $\frac{1}{2}$ -inch in diameter. Except for additions of possible inhibitor elements, this type of mass transfer will not be an initial problem, since there will only be one containment metal in contact with the liquid fuel. The accumulation of fission products, however, will provide the presence of dissimilar metals that can not be avoided. Deposit of the fission products will undoubtedly occur at the interface between the container and the fuel causing possible corrosion or a reduction in the over-all

heat transfer coefficient. This becomes the subject of an investigation outside the realm of this study.

The process of dissimilar-metal mass transfer consists of the dissolution of one solid metal, transfer by diffusion-convection through the liquid metal to the surface of a second metal, and subsequent interdiffusion or reaction. The process is most likely to be controlled by the diffusion or reaction at the second metal surface because the layer growth rate is slow compared to the initial rate of solution of the *first solid metal*. Temperature and the degree of solubility are the two important variables which determine the rate of mass transfer.

Temperature-gradient mass transfer

Temperature-gradient mass transfer occurs in a solid metal-liquid metal system as a result of a temperature difference between two points of the system. The liquid metal can be held static or circulated in a loop. In either case the driving force is the temperature differential and the fact that the solubility of the solid metal is temperature dependent. If a material could be found which had a zero temperature coefficient of solubility, it would be immune to mass transfer of this type.

The mechanism of temperature-gradient mass transfer is illustrated in Figure 15 for the case of a dynamic loop with a hot leg and a cold leg. For alloys, one constituent may be selectively removed by dissolution attack and diffuse into the circulating steam. In most cases the rate of diffusion of the solid metal through the stagnant boundary layer and into the main stream of flow will be the controlling rate for mass transfer. Of course, large temperature differences and large temperature coefficients of

solubility result in increased transfer rates of the solid to the cold portion of the system.

Mass transfer because of a thermal gradient is usually the most damaging type of liquid-metal corrosion to occur, if the metals and conditions are right. Even though the solubility of the container metal in the liquid metal may be extremely small, over a period of time large amounts of the solid can be transformed. Long before any weakening of the container could result, the solid transferred would have begun to form a plug, reducing and eventually stopping flow in a dynamic system. Prevention of this plugging, through proper selection of materials, corrosion inhibitors, or perhaps continuous corrosion product removal, is of great importance in the successful operation of a liquid-metal system.

Epstein (62, 90) has used a heat-transfer analogy to derive equations for temperature-gradient mass transfer in a closed loop. His early equation for diffusion-controlled mass transfer from the hot leg is given by

$$R_T = 0.023 (D/d) (vd/\nu)^{0.8} (\nu/D)^{0.4} \left(\frac{dS^\circ}{dT}\right) \Delta T, \quad (71)$$

where D = diffusion coefficient (cm^2/sec) of the solute in the liquid metal at temperature $T^\circ\text{C}$,

d = inside diameter of the loop tubing (cm),

v = flow velocity in loop (cm/sec),

ν = kinematic viscosity (cm^2/sec) of the liquid at $T^\circ\text{C}$,

S° = solubility of solute in the liquid metal at $T^\circ\text{C}$,

ΔT = temperature differential ($^\circ\text{C}$) in the circuit, and

$\frac{dS^\circ}{dT}$ = average slope of the equilibrium solubility at the mean loop temperature.

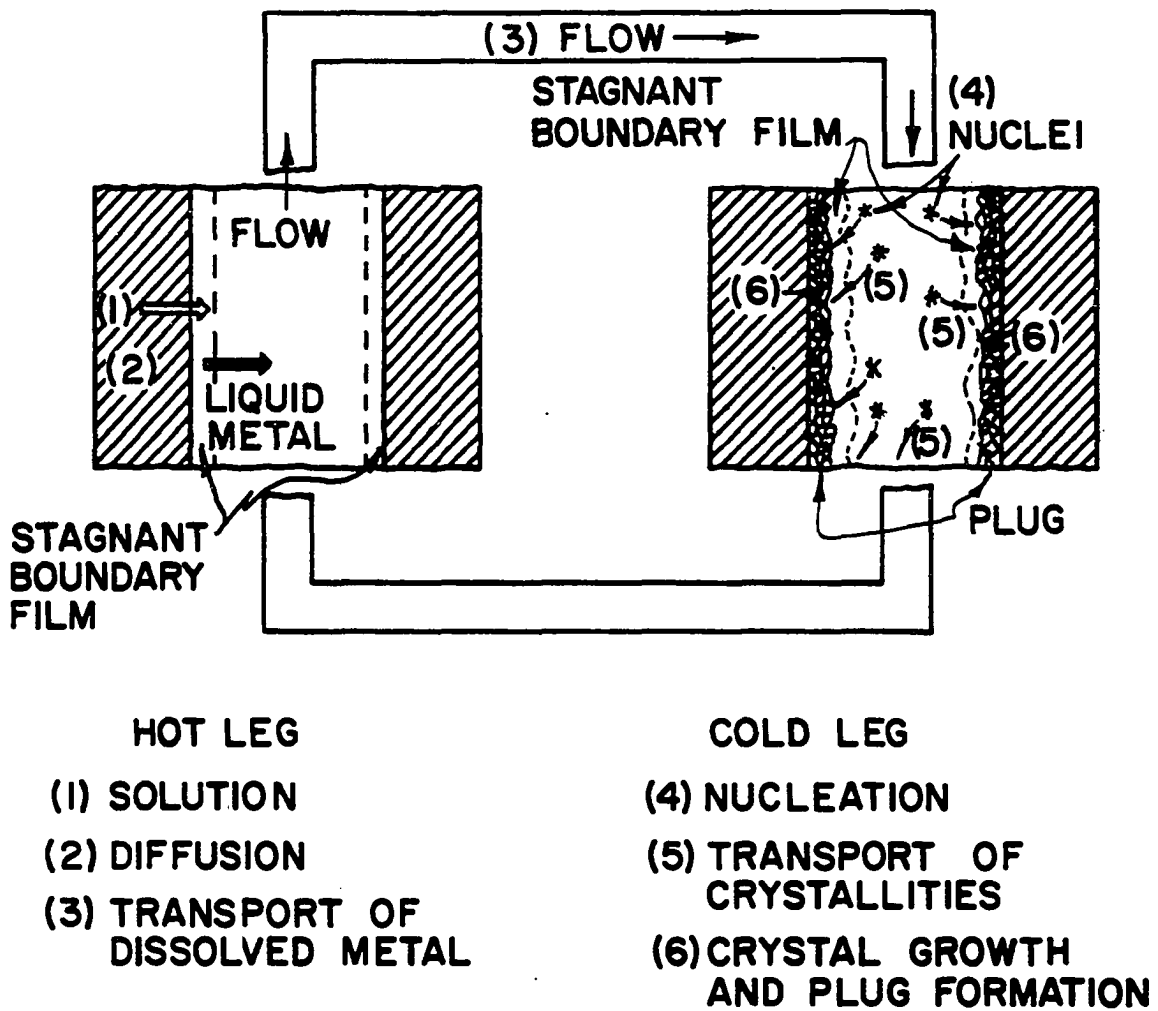


Figure 15. Mechanism of temperature-gradient mass transfer

If the mass transfer is solution controlled, the flow rate is finite, and ΔT is small,

$$R_T = \alpha(S_{T_1}^0 - S_{T_2}^0), \quad (72)$$

where α is again the dissolution-rate constant.

Epstein's more recent equation (90) for temperature-gradient mass transfer which is diffusion-controlled or solution-controlled is given by

$$R_H(x) = - \frac{S_H^c - S_C^c}{(1/\alpha_H + 1/\alpha_C)} \text{Exp}[-(4\alpha_H/vd)x], \quad (73)$$

where $R_H(x)$ = corrosion rate ($\text{g/cm}^2\text{sec}$) at a distance x cm from the beginning of the hot zone,

S_H^c = solubility of solute (g/cc) at the hot zone temperature T_H^c ,
 S_C^c = solubility of solute (g/cc) at the cold zone temperature T_C^c ,

α_H = hot zone dissolution-rate constant (cm/sec),

α_C = cold zone dissolution-rate constant (cm/sec),

d = loop tubing diameter (cm), and

v = flow velocity (cm/sec).

Equation 73 is valid for larger ΔT 's which have long, essentially isothermal areas at both the hot and cold sections of the loop. The mechanism of mass transfer in this case, whether it is diffusion or solution-controlled, and how oxygen or other impurities influence the system, enter into this Equation only insofar as they influence α . Thus, $\alpha = k_s$ (Equation 50) for solution-controlled mass transfer, or $\alpha = D/\delta$ (Equation 51) for diffusion-controlled mass transfer.

The boundary layer thickness δ has been found to be dependent upon velocity and viscosity (60, 64, 65, 66). Ward and Taylor (64) proposed that

$$\delta \propto (v/\nu)^n \quad (74)$$

where $n = 0.5$ for laminar flow and 0.2 for turbulent flow. In their experiments, however, the values of n were not substantiated. Instead, n was found to be unity. Various authors (66) report different values of n , ranging from 0.5 to 1 .

In diffusion-controlled temperature-gradient mass transfer, the corrosion rate R_T should be independent of the velocity v , and indeed, this has been verified experimentally (62).

As mentioned previously under Type E corrosion, the envisioned core of a liquid-metal fueled reactor would consist of a number of long cylindrical fuel pins. The fuel would be essentially static except for convection currents produced by temperature gradients along the length of the core. Because the fuel pins will be approximately $3/8$ to $1/2$ inch in diameter, the convective currents will be somewhat retarded, but not enough to inhibit thermal-gradient mass transfer. Undoubtedly, any corrosion occurring will be diffusion-controlled, characteristic of most liquid-metal systems. With v essentially zero, the boundary layer thickness, δ , will be constant since it is assumed to be independent of temperature (65) or nearly so (91) for diffusion-controlled processes. If the convective velocity v can be determined, the mass transfer rate can be determined from Equations 71 or 73.

In summary, thermal-gradient mass transfer will occur in a liquid metal system regardless of the geometry whenever a temperature differential exists between two points of the system. The equilibrium concentration of the container metal will be higher in the hotter regions than in the cooler regions, and the resulting concentration gradient will allow transport to occur. When the concentration of the solute exceeds its solubility in the cold region, precipitation will take place. The net effect is a continuous transport of material to the cooler regions. Metals which exhibit low mass-transfer rates are those which have very small temperature coefficients of solubility or which are insoluble in the liquid metal. In the case of

mass transfer caused by impurities such as oxygen, inhibitors which remove the impurities are often very successful in reducing corrosion. In liquid-metal systems requiring temperature differences, thermal-gradient mass transfer can be the most damaging because plugs are sometimes formed which restrict circulation.

Factors Affecting Liquid-Metal Corrosion

In the discussion of the six types of corrosion mechanisms which can occur in liquid-metal systems, it is seen that in every case dissolution of the solid metal into the liquid metal occurs before any of the other types of corrosion can proceed. Thus, the over-all corrosion of a system is a combination of Type A and one or more of the other types. Liquid-metal corrosion becomes even more complex because there are so many variables which may affect it. Below are listed the principal factors affecting liquid-metal corrosion:

1. Temperature
2. Temperature gradient
3. Cyclic temperature fluctuation
4. Surface area to volume ratio
5. Purities of the liquid and solid metals
6. Flow velocity
7. Surface condition of the container metal
8. The number of metals in contact with the same liquid metal
9. Metallurgical condition of the container metal.

The use of alloys for both containers and liquid metals again creates additional problems. Indeed, liquid-metal corrosion phenomena are often

complex problems. For this reason, further data on solubilities of single components, multicomponent effects, temperature coefficients of solubility, thermodynamic properties, and kinetics of dissolution and precipitation of solid metals are needed. Better analytical techniques for determining impurity concentrations are also needed in order to correlate their effects upon the various corrosion processes.

REVIEW OF THE LITERATURE

Uranium-Chromium-Iron Phase Studies

Molten uranium and uranium alloys, especially the U-Cr eutectic alloy, have long been of interest as possible fuels or blanket materials in nuclear reactors. In the early 1950's it was realized that the corrosion encountered at the high temperatures necessary to maintain pure uranium in the molten state ($>1133^{\circ}\text{C}$) was more severe than any available metal or alloy could handle. Therefore, attention was focused on the alloys of uranium which melted at much lower temperatures where the corrosion problems would be less harsh. For almost a decade the solution of up to 10 wt.% uranium in bismuth was considered as a possible liquid-metal fuel.

At the same time the high uranium content alloys of chromium, manganese, iron, cobalt, and nickel were also considered as possible solid and liquid fuels. Saller et al. of Battelle Memorial Institute considered several of these and other alloys for possible solid-fuel element material (92). Their work finally settled on the U-5 wt.% Cr eutectic alloy because of its castability and excellent physical properties (93, 94). As a result of adding impurities for grain refinements and improvements in various physical properties, it was found that additions of manganese, iron, or nickel lowered the liquidus and solidus temperatures (51). The experimenters were interested in the effects of these impurities on the melting points, allotropic transformation temperatures, ductility, and other properties. These studies were important because the proposed U-Cr fuel elements were to be fabricated by casting around iron and various stainless steel coolant tubes.

As a result of a general investigation of iron additions to the U-Cr eutectic, Saller et al. (51) noted the presence of a ternary eutectic at 1.0 wt.% iron melting at approximately 760°C. In fact, U. S. Patent 2,735,761 (95) and British Patent 816,603 (96) were issued for the ternary alloy containing approximately 94 wt.% U-5 wt.% Cr-1 wt.% Fe melting at 760°C. However, no liquid-metal corrosion studies were conducted with any of the alloys. A separate study was undertaken to investigate the ternary eutectic point in the U-Cr-Fe system because a previous test at the Ames Laboratory in 1954 (97) and several thermal analyses conducted by the author contradicted the presence of a ternary eutectic at the patented composition. These tests indicated that the composition was an incongruent alloy with a molten range of over 70°C.

Corrosion by Uranium Alloys

Actual liquid-metal corrosion experiments with the U-Cr eutectic in the molten state were first conducted at the Ames Laboratory. From 1953 to 1955 investigators ran a series of preliminary tests with the eutectic in then available tantalum (~99.8% pure), niobium and several tantalum and niobium alloys (98, 99). Pure tantalum showed the best corrosion resistance, but intermetallic compounds of both niobium and tantalum (NbCr_2 and TaCr_2) were formed which caused capsule failure. Additions of 1.0 wt.% iron or manganese to the U-Cr eutectic were also made and the two alloys were tested in tantalum and zirconium containers (97). Tests were conducted at 850°C until the alloys penetrated the 0.005 inch wall capsules; 30 days for tantalum and 21 days for zirconium. This rate was essentially that observed for the pure eutectic at 900°C. The liquidus and solidus

temperatures for the U-Cr-1.0 wt.% Fe alloy (supposedly a ternary eutectic (51) melting at 757°C) were found to be 841° and 776°C, respectively.

In an agitated thermal-gradient capsule test run at temperatures of 900° and 1000°C, the observed penetration rate for pure U-Cr in tantalum was 0.010 inch in 14 days (97). This was about twice the rate observed in static, isothermal tests. The most severe corrosion occurred at the 1000°C end. A similar test with a 0.3 wt.% silicon addition at 950°C to 1050°C underwent a corrosion rate of 0.003 inch per day (87) compared to the above test of 0.007 inch per day at 900-1000°C.

These same investigators (87, 88, 100) also tried carbide coatings on molybdenum, niobium, tantalum, titanium, vanadium, and zirconium of 0.001 inch thickness for tests with pure uranium and the U-Cr eutectic. Only tantalum crucibles with a TaC₂ coating proved to be promising as a container for U-Cr. A 2000 hour test at 1100°C was successful and no evidence of corrosion attack was discovered by microscopic examination (100). Tests with pure uranium at 1200 to 1300°C were unsuccessful. Other tests with the eutectics, U-Fe, U-Mn, and U-Ni, were also unsuccessful in niobium, molybdenum, tantalum, zirconium, and thorium at 800°C. Of the five metals, tantalum showed the best resistance to corrosion.

Yttrium, when it first became available in large quantities in 1957, was found to be immiscible with uranium (2). This naturally led to a series of tests with the various uranium-rich eutectics in yttrium capsules. Fisher and Fullhart (7) and Cash and Fisher (10) list data on a number of tests conducted with U-Cr, U-Fe, and U-Mn in niobium, tantalum, and yttrium. The only system completely free of corrosion attack was U-Cr in yttrium. The longest test lasted 2991 hours at 900°C supposedly without any signs of

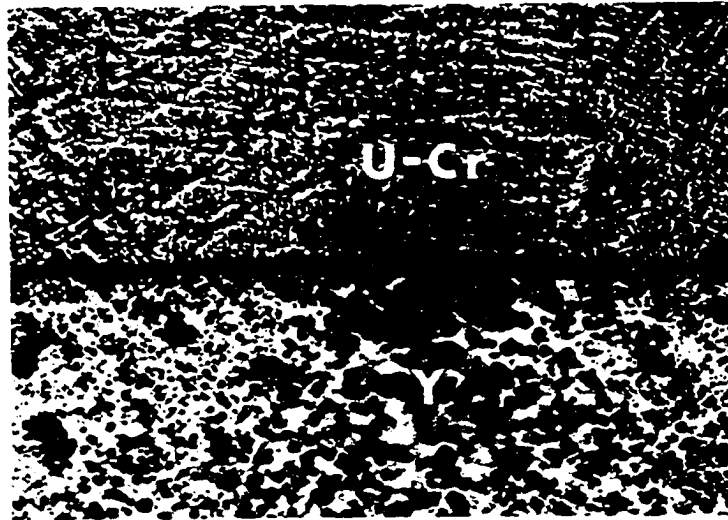


Figure 16. Uranium-chromium eutectic--yttrium interface, 120X (static test: 1100 hours at 900°C)

corrosion attack. Isothermal, static, and dynamic tests were conducted. Test capsules were examined microscopically, but apparently no solubility or spectrographic analyses were taken. Figure 16 shows a microphotograph of the interface from one of the test capsules.

Two yttrium loops were also constructed at the Ames Laboratory and operated with circulating U-Cr eutectic; however, both failed. There was no detectable mass transfer or intergranular attack of the yttrium in either case. The first loop operated for 250 hours at temperatures up to 1000°C, but the second loop failed after 12 hours with temperatures up to 1100°C. Yttrium sections of the latter loop were found to contain over 1000 ppm of copper impurity. Since copper forms an eutectic with yttrium melting at 760°C (9), the failure was subsequently blamed upon the copper impurity. Copper had been used as the jacket material when the yttrium tubing was extruded. Even though the copper liner was removed by pickling in a solution of 50% HNO₃ - 50% HF, enough copper had probably been

worked into the yttrium matrix during extrusion to cause localized melting at elevated temperatures.

The U-Mn eutectic in both tantalum and yttrium up to 925°C showed some signs of attack after tests of 250 to 500 hours, but the capsules had not failed. The U-Fe eutectic was more corrosive and failed in both containers in less than 200 hours at 900°C.

Los Alamos Scientific Laboratory in a search for capsule materials for U-Pu-Mn, U-Pu-Fe, and Pu-Co-Ce alloys also considered yttrium and tantalum (4, 5). Tests were conducted on the U-Mn and U-Fe eutectics with and without plutonium additions. No tests were conducted with the U-Cr eutectic, however. Yttrium containers underwent dissolution attack with U-Mn at 850, 900, and 950°C and dissolution and intergranular attack with U-Fe at 850°C. The presence of plutonium tended to reduce the amount of attack. The degree of attack was about the same after 1000 hours as it was after 200 hours for U-Mn in yttrium at 850°C. There was a similar, but more marked intensification at 900 and 950°C at the meniscus level. The increased attack where the circulation of a part of the fuel with the bulk of the fuel is inhibited (meniscus) may be related to the fact that the Y-Mn system exhibits an eutectic at 25.2 wt.% Mn melting at 878°C as well as several intermetallic compounds (101). This might set a maximum temperature for containing U-Mn in yttrium although the attack at 950°C is not catastrophic (4, 10). Plutonium additions appeared to inhibit attack at the meniscus. The U-Fe eutectic in yttrium at 850°C for 1000 hours was about twice as corrosive as similar tests with U-Mn.

Tantalum was used to contain the ternary U-Pu-Mn in a 200 hour test at 950°C; dissolution attack occurred to a depth of 0.0008 inch (5). With a

carbide layer, tantalum suffered 0.0015 inch of intergranular attack with U-Mn at 1100°C for 210 hours. No dissolution was observed in this test (102).

Corrosion tests on Ta-0.1% W alloys with yttrium additions involving the Pu-Fe fuel revealed a considerable improvement in the corrosion resistance as a result of the yttrium additions (103). The yttrium tends to segregate in the grain boundaries and inhibits intergranular penetration. Carburization of tantalum also seemed to retard corrosion by both Pu-Fe and Pu-Co-Ce.

Davis et al. (104) have studied the design of a liquid-metal fuel reactor using U-Fe eutectic. They reported that Knolls Atomic Power Laboratory has contained U-Fe in vanadium capsules at 900°C with little evidence of corrosion. Experimental data on these tests were not given, but it seems unlikely that vanadium would be adequate because the Fe-V system exhibits an intermetallic compound. No other information on U-Fe in vanadium was found in the literature.

Additional container materials for containment of U-Cr and other high content uranium alloys have been suggested and investigated by Powell (105). Tests from 860°C up to 950°C with capsules made from 95 wt.% U-5 wt.% Nb and 90 wt.% U-10 wt.% Nb were successfully run with the U-Cr eutectic for periods up to one month. An essential element of these capsules, however, is the oxide layer (UO_2 and U_3O_8) separating the capsule material from the molten eutectic. This oxide layer must be built up before the actual containment can be effected by passing oxygen over the surfaces for several minutes at 400°C. Powell concludes that the U-Ni eutectic severely attacks the U-5 wt.% Nb capsules, even at 800°C. In addition, thermal cycling causes a breakdown of the oxide layer.

EXPERIMENTAL PROCEDURE

There are two general experimental methods for determining the corrosion of solid metals by liquid metals: static tests and dynamic tests. Static tests are usually conducted under isothermal conditions or as nearly so as possible. They involve capsules or a pot of the liquid metal in which coupons are suspended. Dynamic tests consist of agitating the liquid metal past the solid metal surface as with rocker type tests, spinner tests in a molten pot of liquid, or a circulating loop. Rocker tests are run either isothermally or under a temperature gradient, while spinner tests are done isothermally and loop tests use a temperature gradient.

Static, isothermal tests were employed in this investigation because they are useful in cases where the solubilities of the systems to be tested are not known. They are sufficient to determine dissolution attack, intergranular attack, and intermetallic compound formation. Actually only dissolution attack is to be expected from the U-Cr eutectic in yttrium, while possibly the other two corrosion mechanisms may be present with the U-Cr-Fe system in yttrium. It has already been shown that intergranular penetration is unlikely when the solubility is extremely low (71) and there is a large atomic size difference (75). The static systems were not only inexpensive and easier to fabricate than dynamic systems but also allowed closer control of important variables which affect corrosion.

Static tests are excellent for providing a means of eliminating corrosive systems and can also be quite a good method for selection of desirable systems. In the present day envisaged design of a liquid-metal fuel reactor, the core would consist of long cylindrical fuel pins as in the

LAMPRE project. In such a design, the liquid fuel would circulate slowly by convection under the temperature gradient present. Static tests are therefore selective for such a system and were used extensively in determining suitable containers for the Pu-Fe and Pu-Co-Ce fuels used in LAMPRE I and II (4, 5, 106). This is not to say that dynamic tests need not be employed for a full evaluation of a particular system. Only an in-pile test under neutron irradiation and actual expected conditions can give complete answers.

Much of the important corrosion work in liquid metals is empirical. Theoretical models for predicting solubilities, as well as other physical parameters which enter into the analysis of corrosion processes, are so poor that they are virtually useless (107). There is essentially no alternative to direct experimental measurement. Many workers in this field seriously doubt whether it is possible to formulate general laws of behavior for liquid-metal systems (107).

Corrosion Tests Procedure

In all tests of this investigation except those for the solubility runs, the molten fuel was in contact with only one container material in order to avoid interactions discussed under Type E corrosion attack. Coupon specimens were not used, and thus only interactions between the inner capsule surface and the liquid fuel were possible.

Tantalum capsules were used for differential thermal analyses because of the ease of fabricating the special thermocouple well, while yttrium was employed for the regular corrosion test runs. The tantalum and yttrium capsules were prepared by cutting off two-inch lengths of high-purity

annealed stock tubing with a silicon carbide cut-off wheel. For tantalum, the tubing was 0.75 inch O.D. with 0.030 inch wall thickness. Caps for the tubing ends were punched from 0.030 inch tantalum sheet with a specially designed die which produced a cup 0.690 inch in diameter about 7/32 inch high. The bottom caps were drilled to accommodate a 5/32 inch O.D. tantalum tube, 1/2 inch in length, sealed over at the top end (Figure 20). This thermocouple well was welded into the cap by an electron-beam welder, as described below.

The yttrium tubing was 0.800 inch O.D. with 0.050 inch thick walls. End caps were punched from 0.040 inch high-purity sheet at 7/8 inch diameter and subsequently turned down to 0.735 inch diameter on a lathe. The capsule ends were recessed with a 0.050 inch lip, 0.740 inch in diameter to support the end caps and provide a ridge of metal which fused to the cap during welding.

The surfaces of the tantalum capsules were left in the "as received" condition except for cleaning. The inner yttrium surfaces, however, were polished to a smooth finish with 600 grit silicon carbide abrasive cloth.

The capsules and end caps were thoroughly cleaned in acetone with an ultrasonic cleaner and air dried on absorbent tissue. The bottom caps were welded in place first using a Sciaky Electron-Beam welder (E.B.). Each weld was then carefully checked for faults under a magnifying glass and tested on a Veeco helium leak detector. Leaky capsules were rewelded or rejected. Each capsule and lid were carefully weighed before and after insertion of the test sample. Enough sample was added to fill the capsule half full when in the molten state. The capsule was then evacuated and backfilled with argon; the top lid was put in place under argon, and the whole capsule was

evacuated in the E. B. welder to 10^{-4} to 10^{-5} torr before welding. After welding, the top lid was examined carefully for possible cracks or inclusions. It was not possible to leak check this weld; thus the top of the capsule was always the last weld completed. Since the liquid metal was not expected to contact this area except by vapor or a climbing action, failures caused by faulty welds would be minimized. Figure 17 is a photograph showing the tubing, end cap, weld, and cleaned inside surface of an yttrium capsule.

The yttrium capsules were next sealed in three-inch capsules of $3/4$ inch, schedule 40 Inconel 600 pipe for protection against oxidation at high temperatures. These welds were also accomplished in the E. B. welder. End caps for the Inconel pipe were prepared from $7/8$ inch solid rod cut into $1/8$ inch disks. The ends were prepared in the same manner as for yttrium capsules. The Inconel welds were also inspected as previously described. Because yttrium readily combines with the nickel present in Inconel, the capsules were first wrapped in 0.002 inch tantalum foil to prevent direct contact with the Inconel surfaces. A typical test capsule arrangement is shown in Figure 18. The vacuum produced by the E. B. welder between the yttrium capsules and the Inconel sheath was sufficient to protect them from oxidation.

Preparation of the liquid alloys consisted of either separate arc melting beforehand or of adding the desired weight of individual constituents to the capsule, sealing, and induction melting. In most instances the alloys were prepared in electric-arc vacuum melters first as buttons which were turned over and remelted several times before finally melting into "fingers".



Figure 17. Yttrium capsule showing weld, cap, and inside surface

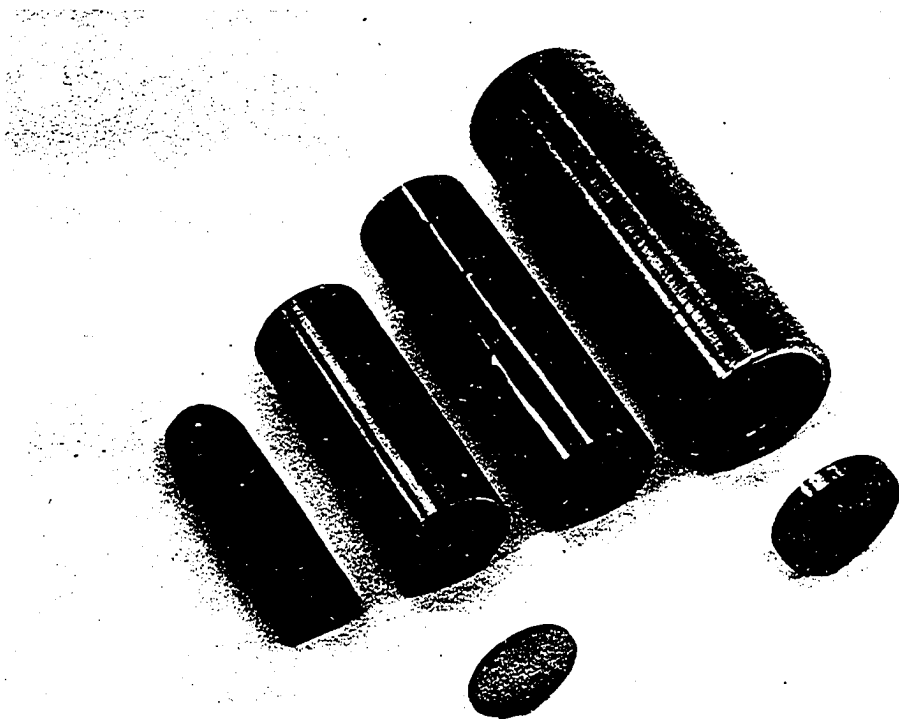


Figure 18. Uranium-chromium slug with yttrium capsule, tantalum foil, and Inconel sheath

After the sealed Inconel capsules were carefully inspected, they were placed in preheated electrical muffle furnaces for the corrosion tests. Figure 19 shows the furnace bank used. The furnace temperatures were measured by chromel-alumel thermocouples placed inside the furnaces, and each temperature was recorded on a six-point Honeywell strip-chart recorder. The furnace temperatures were controlled by individual powerstats which controlled the power input to each furnace. A constant voltage transformer was used to eliminate the normal voltage fluctuations and supply electrical power to the variable powerstats. This method of furnace control supplied a continuous source of heat which maintained essentially a constant temperature. Variations were less than $\pm 2^{\circ}\text{C}$ for test periods up to 3000 hours, and they were gradual over a period of hours and not like the frequent ± 5 to 10°C cycling of an on-off controller. In some systems, it is found that constant temperature cycling has a considerable effect on corrosion rates (57).

After completion of certain test periods, the Inconel capsules were removed and water quenched in order to maintain the solution state and avoid possible precipitation. The Inconel end cap was removed with a lathe and the yttrium removed. The capsule was then cut in half axially on the cut-off wheel for examination and specimen preparation.

Differential Thermal Analyses

The melting-point determinations were conducted in tantalum capsules with a thermocouple well as shown in Figure 20. Induction melting of the constituents directly in the tantalum capsules was done frequently for these tests, although a number of alloy samples were prepared by electric-

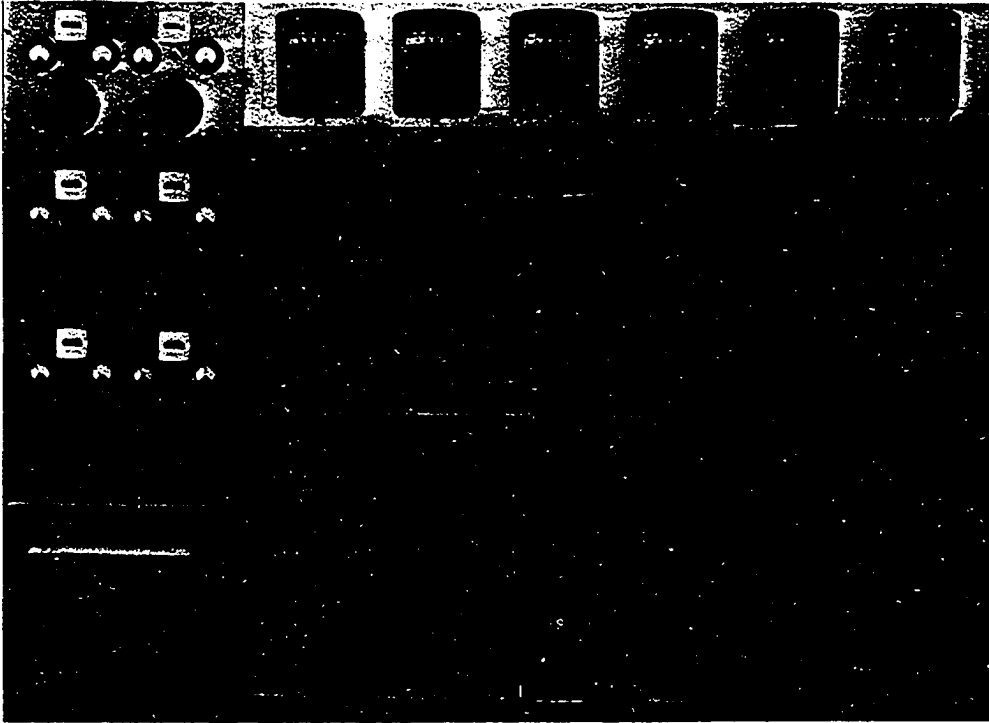


Figure 19. Furnace bank showing rotary apparatus, control panel, and constant voltage transformer

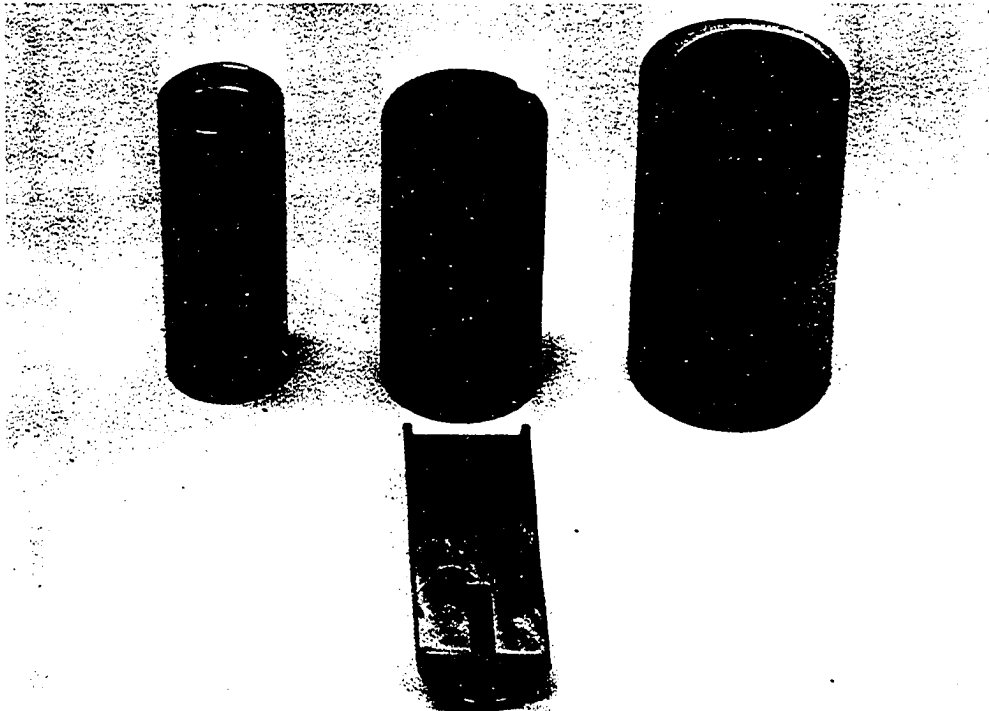


Figure 20. Tantalum capsules with thermocouple well, insulator, and molybdenum standard capsule for melting-point determinations

arc vacuum melting. As a standard reference, a molybdenum holding capsule (Figures 20 and 21) was used to contain the tantalum melting-point capsules. The Molybdenum in turn was supported by a 2 inch diameter tantalum cup. Two calibrated chromel-alumel thermocouples were used; one for the molybdenum reference and one for the tantalum capsule well temperature. Using a Leeds-Northrup Model K-3 potentiometer, measurements of the tantalum well temperatures were made whenever a transformation occurred. This was determined by using a two-pen Honeywell strip-chart recorder which indicated the well temperature and the differential temperature between the molybdenum and the tantalum. The determinations were made in the large Inconel bomb shown in Figure 21 in an atmosphere of helium. In each run the thermocouple contacting the top of the tantalum well actually supported the capsule thereby assuring a good thermal contact. Heating and cooling rates were obtained in a vertical electric muffle furnace using a programmed controller. Linear rates from 60 to 300 degrees per hour were employed.

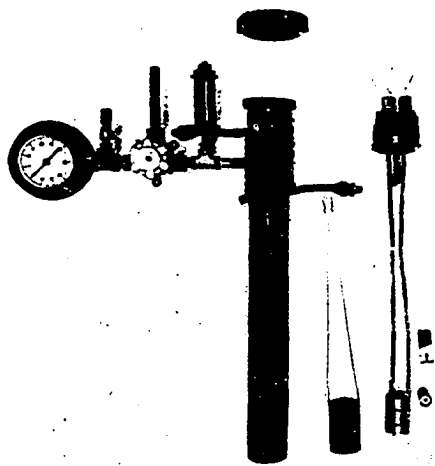


Figure 21. Inconel bomb used for differential thermal analyses

Solubility Tests Procedure

In order to determine the dissolution rate constant, α , it was necessary to obtain a plot of yttrium concentration in the bulk of the liquid-metal fuel versus time. Yttrium concentration data from analytical and radiochemical analyses were obtained by two separate series of solubility tests.

Radioactive tracer technique

Yttrium tabs, which were irradiated approximately 20 minutes in a thermal neutron flux of 4×10^{13} neutrons/cm²-sec, were equilibrated with the U-Cr eutectic at 950°C for periods from 10 minutes to 24 hours. These tests were conducted in a specially designed 360° rotary capsule holder which is inserted in one of the muffle furnaces as shown in Figure 19 (Furnace No. 4). This device holds two capsules near the center of the heated zone of the furnace about 10 inches from the front opening. A chromel-alumel thermocouple was attached to the side of each capsule holder for accurate temperature monitoring. Each capsule was held in place by an Inconel slide wire, which allowed instantaneous release of the capsules into a water bath in front of the furnace for quenching. The capsules were kept in a vertical position during quenching by two vertical pieces of pipe immersed in the water bath.

In these tests 2.065 inch long by 0.625 inch I.D. graphite crucibles with tight fitting caps were used to contain the eutectic alloy. The yttrium tabs were placed in a 5/32 inch deep slot in the top graphite lid. The graphite, in turn, was sealed in Inconel sheaths in the E. B. welder. The yttrium tabs were 0.032 inch thick by 0.250 inch wide by 0.656 inch

long. When positioned in the graphite caps, 0.500 inch of the tab length was exposed above the slot. This provided a surface area of 1.87 cm^2 for contact with 50.00 grams of the eutectic or a surface to volume ratio of $S/V = 0.65 \text{ cm}^{-1}$.

After the Inconel capsules with the graphite crucibles were sealed, they were placed singly in the 360° rotary device and subsequently put into the preheated furnace in a vertical position with the yttrium tab on top. When the capsule temperature stabilized at 950°C (45 to 60 minutes), the capsule was inverted to allow the eutectic to contact the yttrium tab and begin the testing period. The capsule was rotated through a 270° arc at three cycles per minute using a reversible, variable-speed, DC motor. At the end of the test period, the yttrium tab was again rotated to the top. One minute was allowed for the U-Cr to settle to the bottom of the graphite before the capsule was quenched. The graphite capsule was removed and broken apart to obtain the equilibrated sample. The surface scum was removed on a lathe, and the slug was then sliced into three or four pieces for radioactive separation. This analysis procedure is explained later.

Analytical analysis technique

This method of determining yttrium concentration in the bulk of the U-Cr eutectic was chosen when difficulties were encountered in getting the true yttrium-90 activity from the samples run with radioactive yttrium tabs. The procedure for these tests consisted of preparing 16 regular yttrium capsules for solubility runs in the 360° rotary furnace. The capsules were the same as those used for the corrosion tests.

The surface area of each capsule was calculated from the inner dimensions and then enough previously arc-melted eutectic was readied to make the surface to volume ratio $S/V = 5.50 \text{ cm}^{-1}$. This amounted to filling the capsule approximately one-half full with the alloy. These capsules were subsequently placed in the proper length Inconel sheaths to fit in the 360° rotary apparatus.

Since in these tests the molten alloy would be in contact with the yttrium surfaces as soon as the melting-point temperature was reached, it was important to reach the test temperature and start counting the time of the test period as quickly as possible. To accomplish a standard procedure, a number of blank runs were tried to become familiar with the over-all test operation.

First, the Inconel sheath and its enclosed capsule were preheated to $860 \pm 2^\circ\text{C}$ in a separate furnace for about 30 minutes. The 360° rotary holder in turn was preheated to approximately 975°C in Furnace No. 4. At a given time, the rotary apparatus was quickly removed from the furnace and the preheated sample transferred to its holder. The rotary apparatus was then returned to the furnace and the powerstat adjusted to its test temperature setting. This procedure took less than 15 seconds to complete. Timing of the test period and the beginning of 360° rotation commenced two minutes after the capsule holder temperature reached the test temperature. Thus, four to five minutes after placing the rotary apparatus in the furnace, timing of the capsule test duration started. This additional time should have allowed the alloy to reach the test temperature at about the time rotation and timing were started. Since Inconel is a rather poor heat conductor, it was felt the extra time of two minutes was necessary for the

U-Cr eutectic to reach the test temperature. In all cases, the outer Inconel capsule temperature as indicated by the thermocouple in the capsule holder increased approximately 10°C above the test temperature during this interval, but rapidly decreased to the test temperature when rotation was started.

About 15 seconds before the end of the test duration, the capsule was rotated to a vertical position and the chain removed so that quenching could be rapidly effected at the end of the timing. Tests were conducted at 900, 950, 1000, 1050, and 1100°C for times from 3 minutes to 120 minutes. Rotation was maintained at 3 rpm, with two turns in a clockwise direction before reversing to a counter-clockwise direction for two revolutions. This was done with a timer and a relay hooked to the DC rotary motor to prevent twisting of the thermocouple lead wires to the temperature recorder.

After each capsule was tested, the yttrium capsule was removed and sectioned axially on a cut-off wheel. A sample of approximately five grams was cut from the bulk of the eutectic, well away from the wall. These samples were then sent to Analytical Services for determination of the yttrium impurity.

Methods of Capsule Examination

Several methods of analysis were used to evaluate the type of corrosion and the corrosion products of each capsule. These included analytical analyses for yttrium in the U-Cr and U-Cr-Fe liquid metals, spectrographic analyses for any uranium, chromium, or iron in the yttrium, microprobe analyses, and metallographic and visual analyses to determine the amounts and mechanisms of corrosion. The combined results of all of these analyses were

considered in making conclusions about the corrosion tests.

Spectrographic analysis

Samples from the bulk of the liquid metal were analyzed spectrographically to determine the presence of yttrium before analytical analyses were made. Filings from the outer capsule surfaces were checked for uranium, chromium, or iron penetration through the grain boundaries.

Analytical analysis

Samples of the liquid-metal fuel in the capsules were analyzed for yttrium content after the corrosion tests. The sample was taken from the bulk metal at a distance from the capsule wall. The purpose of this test was to determine the amount of capsule metal in solution as a function of test duration and temperature.

Radioactive tracer analysis

The U-Cr eutectic slices were first dissolved in 3N HCl followed by the addition of 6N HNO₃ and heated until the uranium had dissolved. Using 3 gram samples, yttrium carrier was added. The yttrium was precipitated from solution with HF after which it was scavenged four times with thorium and ceric iodate to remove thorium daughter products. The remaining yttrium was precipitated as yttrium oxalate which was weighed and counted for the yttrium-90 β . The count rate was corrected to 100% yield by the use of a standard sample irradiated with the original tab.

Visual analysis

Simple visual inspection of the samples after sectioning and during preparation of the samples for analysis was particularly informative as a

qualitative test evaluation. Information noted visually included a check for swelling, possible oxidation, the presence of any residues, the presence of any condensate on the walls of the vapor region, and points at which corrosion attack was most likely to occur. A check of the meniscus was always made in order to note whether or not wetting of the capsule walls had occurred and to see if the liquid metal also showed any tendency to climb the walls and completely cover the available surface area.

Metallographic analysis

Probably the most informative single analysis was metallography. Sections of the corrosion capsule were polished and etched for microscopic examination. The yttrium wall adjacent to both the liquid and vapor region was etched to detect any changes in grain structure or any grain boundary penetration by the liquid metal. The formation of any intermetallic compounds or any dissolution attack of the yttrium wall could also be detected.

Microprobe analysis

Microprobe analyses were conducted on a number of corrosion test samples and melting-point samples as a further check on analytical, spectrographic, and metallographic analyses. Informational data on grain boundaries, interface regions, and element distributions were obtained. The presence of various possible elements was confirmed or denied in a number of instances. Several photographs were obtained from oscillograph traces which will be presented later.

Materials

High-purity metals were used in all of the corrosion tests in order to

minimize the effect which any impurity might have on corrosion. Care was taken to remove all surface films from the metals before encapsulation to ensure high-purity samples.

Uranium

The uranium used in this investigation was 99.9% pure obtained from the National Lead Company of Ohio in the form of cylinders 1-3/8 inch in diameter by 4 inches long, weighing about 1.8 Kg. The analysis furnished by the supplier was an average of 21 regular production derbies. The results are shown in Table 9.

Table 9. Chemical analysis of uranium

Element	Average	Range
	ppm	ppm
C	30	5-100
N	55	10-650
Cr	24	10- 50
Cu	8	1- 15
Fe	100	39-168
Mg	61	8-800
Mn	11	6- 20
Ni	56	14- 70
Si	31	15- 70

Chromium

The chromium used for making the U-Cr eutectic was 99.997% pure crystal bar stock obtained from the Chromalloy Corporation. A typical analysis of the metal as well as an Ames Laboratory spectrographic analysis is given in Table 10.

Table 10. Chemical and spectrographic analyses of chromium

Element	Supplier analysis	Ames Laboratory spectrographic analysis
	ppm	
O	2	
H	0.3	
N	1.9	
C	10	
Al	1	--- ^a
Ca	2	---
Cu	0.1	---
Fe	11	Faint Trace
Mg	2	---
Mn	0.1	---
Ni	1	---
Si	10	---
V	1	

^a--- means impurity level was too low to be detected.

Iron

Electrolytic melting stock iron was obtained from the Glidden Company with a purity of 99.940%, in the form of brittle sheet 1/16 to 1/8 inch in thickness. The typical impurities for this grade of iron as given by the supplier are shown in Table 11.

Table 11. Chemical analysis of electrolytic iron

Element	Suppliers analysis wt.%	Element	Suppliers analysis wt.%
Al	<0.001	Mo	<0.004
Be	<0.0005	Ni	0.001
Ca	<0.001	N	0.0005 ^a
C	0.002	O	0.014 ^a
Cr	0.001	Si	0.003
Co	0.0010	Ta	<0.001
Cu	0.004	Sn	<0.003
H	0.0010 ^a	W	<0.001
Pb	<0.001	V	<0.001
Mg	<0.0005	Zn	<0.001
Mn	0.0015	Zr	<0.001

^aAmes Laboratory vacuum fusion analysis.

Yttrium

The yttrium used in the investigation was extruded from Ames Laboratory production Billet No. 345 as tubing of 0.85 inch O.D. by 0.65 inch I.D. A special graphite lubricant was used instead of a copper jacket (108).

Metallographic examination of several cross sections of the extruded tubing revealed an oxide layer of 0.005 to 0.010 inch thick on the outer surfaces and a 0.001 to 0.004 inch layer on the inner surfaces. Both layers were subsequently removed when the capsules were finished on a lathe to 0.800 inch O.D. by 0.695 inch I.D.

Before extruding, the larger six-inch diameter billet was doubly electron-beam melted into four 2½ inch diameter billets to further remove fluorides and oxygen. Table 12 lists the major impurities of the billet before it was electron-beam melted.

Table 12. Ames Laboratory analysis of yttrium billet No. 345

Element	Impurity level	Element	Impurity level
	ppm		ppm
O	690 ^a	Ni	< 1
F	619 ^{a,b}	Ca	< 10
C	286	Mg	< 13
N	103	Si	<150
Cu	25	Ti	<500
Fe	157	Zr	< 50

^aBoth values lowered as a result of electron-beam melting.

^bFluoride content probably <100 ppm after electron-beam melting.

Tantalum

High-purity tantalum tubing was purchased from the National Research Corporation at 99.97% purity for melting-point capsules and other corrosion

tests. The six-foot lengths of tubing were 0.750 inch O.D. with 0.030 inch wall thickness. The impurities present are listed below in Table 13.

Table 13. Chemical analysis of tantalum tubing

Element	Suppliers analysis	Element	Suppliers analysis
	ppm		ppm
O	13	Mo	39
N	33	Nb	130
C	8	Ni	1
Al	<10	Si	10
Cr	< 1	Ti	< 5
Cu	< 1	W	51
Fe	< 5	Ta	balance

RESULTS AND DISCUSSION

The results of each of the three studies--U-Cr-Fe eutectic investigation, solubility tests, and corrosion tests--will be presented individually under separate headings. Where appropriate, tables and figures with photomicrographs are shown for easy reference.

Uranium-Chromium-Iron Phase Studies

Table 14 lists the results of the differential thermal analyses run by the author as a part of this investigation. Various compositions in the uranium-rich end of the ternary system were tested including additions of iron from 0.02 to 10.0 wt.% to the base U-Cr eutectic. It is seen that the samples at 1.0 wt.% iron (No's 0040 and 0254) exhibit average solidus and liquidus temperatures of 765 and 834.5°C, respectively. This is clearly not the eutectic composition. This was also confirmed by microscopic examination of the samples as seen later in several photomicrographs (Figure 24c).

A plot of the thermal data using various iron additions to the U-Cr eutectic from 0 to 10.0 wt.% iron is shown in Figure 22. This partial phase diagram indicates the ternary eutectic to be near the 2.5 wt.% iron addition. This composition corresponds to point A on the tentative ternary phase diagram in Figure 23 which is a polythermal projection of the liquidus surface of the region under investigation. Here, E_1 and E_2 are the pure U-Cr and U-Fe eutectic compositions, respectively. The dashed lines running from points A and B on the diagram represent approximate binary eutectic valleys leading from the binary eutectic compositions

Table 14. Differential thermal analyses data^a for uranium-chromium eutectic and uranium-chromium-iron alloys

Sample No.	Nominal composition (wt.%)			Transformation temperatures (°C)			
	U	Cr	Fe	$\alpha \rightarrow \beta$	$\beta \rightarrow \gamma$	Solidus	Liquidus
0007	95.00	5.00 ^b	--	661	758	870	872
0008	94.97	5.03 ^b	--	662	757	870	871
0009	94.82	5.18 ^b	--	661	757	870	872
0012	95.00	5.00	--	662	759	871	874
0255	95.00	5.00	--	662	758	869	872
0038	94.98	5.00	0.02	655	755	863	871
0251	94.98	5.00	0.02	655	753	863	872
0252	94.76	4.99	0.25	654	750	766	863
0039	94.52	4.98	0.50	653	750	765	855
0253	94.52	4.98	0.50	652	750	765	855
0041	94.29	4.96	0.75	651	750	765	852
0040	94.05	4.95	1.00	653	750	765	834
0254	94.05	4.95	1.00	654	750	765	835
0019	93.91	4.94	1.15	651	750	765	835
0042	93.81	4.94	1.25	654	750	765	835
0017	93.58	4.92	1.50	654	750	766	816
0256	92.62	4.88	2.50	653	750	765	767
0053	92.15	4.85	3.00	661	750	765	768
0054	91.44	4.81	3.75	None	750	765	768
0257	90.25	4.75	5.00	None	None	748	755
0258	85.50	4.50	10.00	None	None	736	746
0051	96.50	1.00	2.50	654	750	765	795
0031	91.08	1.88	7.04	None	None	724	752
0035	92.38	2.62	5.00	None	None	746	761
0052	95.00	2.50	2.50	655	750	765	765.6

^aAverage values taken from two or more runs.

^bChromium content determined by chemical analysis.

to the ternary eutectic composition. The lines are shown linearly, although in actuality they probably curve slightly changing inflection once or twice before reaching the ternary point. A similar dashed line is also drawn to the composition of the liquidus valley on the Cr-Fe side of the diagram (22 wt.% Cr).

The three areas labeled " α ", " β ", and " γ " in Figure 23 are primary phase fields. These primary phase fields are separated by the eutectic curves or binary valleys. A primary phase field is that volume of a temperature-composition prism for a three-component system in which one solid is in equilibrium with the melt. A binary valley is the line of intersection of two adjacent primary phase fields along which the two solids of the adjacent primary phase fields are in equilibrium with the melt. At the ternary eutectic point, the three solid phases and the melt are in equilibrium.

Point B on the ternary diagram corresponds to the composition for Sample 0052. Again linear dashed lines are drawn from the point to E_1 , E_2 , and E_3 representing proposed binary valleys. This composition exhibits the closest approach to the ternary eutectic composition of all the alloys run (Table 14) as evidenced by both thermal analysis and microscopic examination (Figure 24f). Although Sample 0256 displayed a near eutectic composition by thermal analysis, metallographic examination did not corroborate this finding (Figure 24e).

According to Ricci (109), the three binary eutectic curves meeting at point E must intersect in such a way that the angle between adjacent curves is not greater than 180° . Thus in Figure 25, configurations (a)

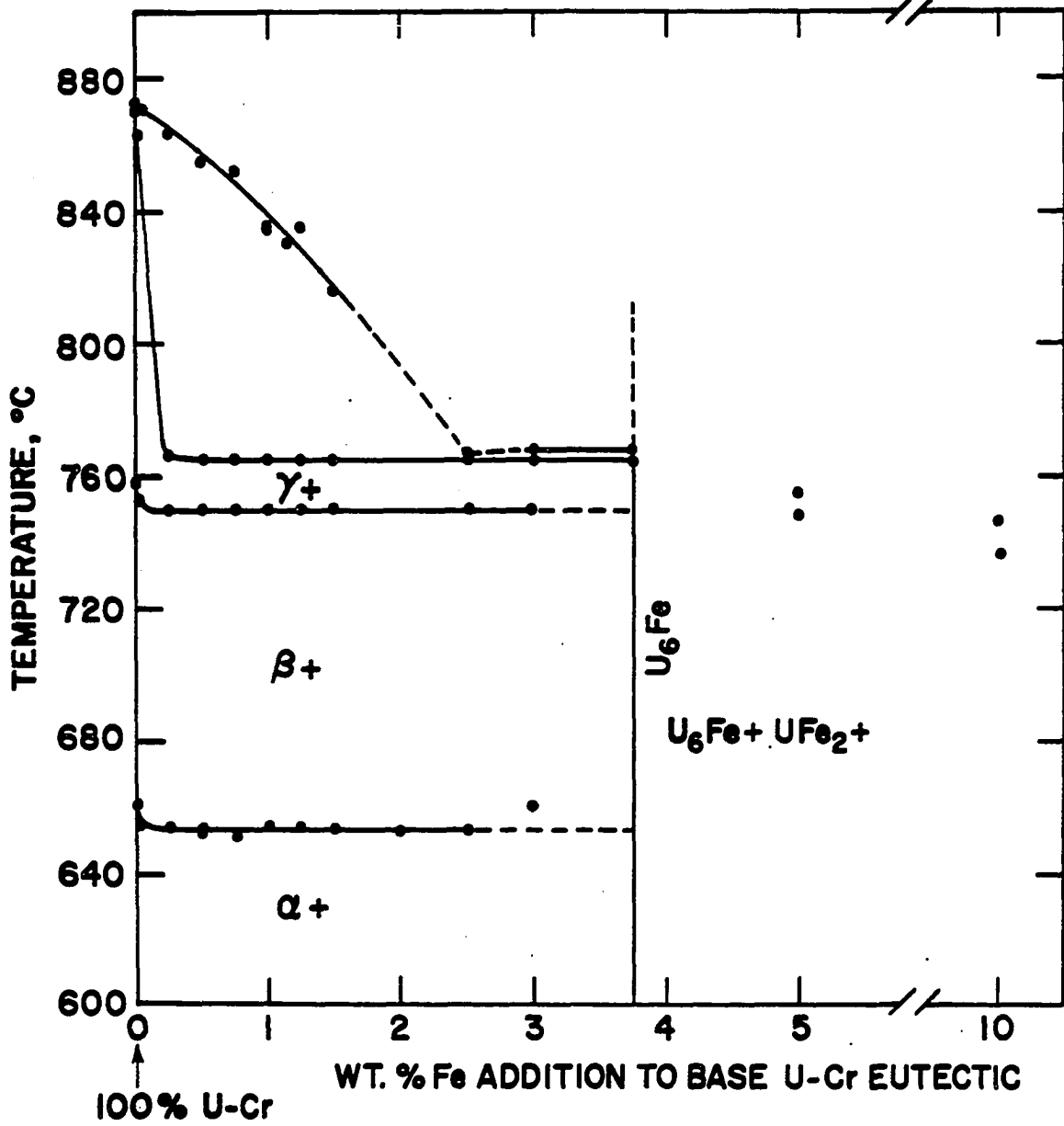


Figure 22. Proposed partial binary phase diagram for the uranium-chromium eutectic versus iron system

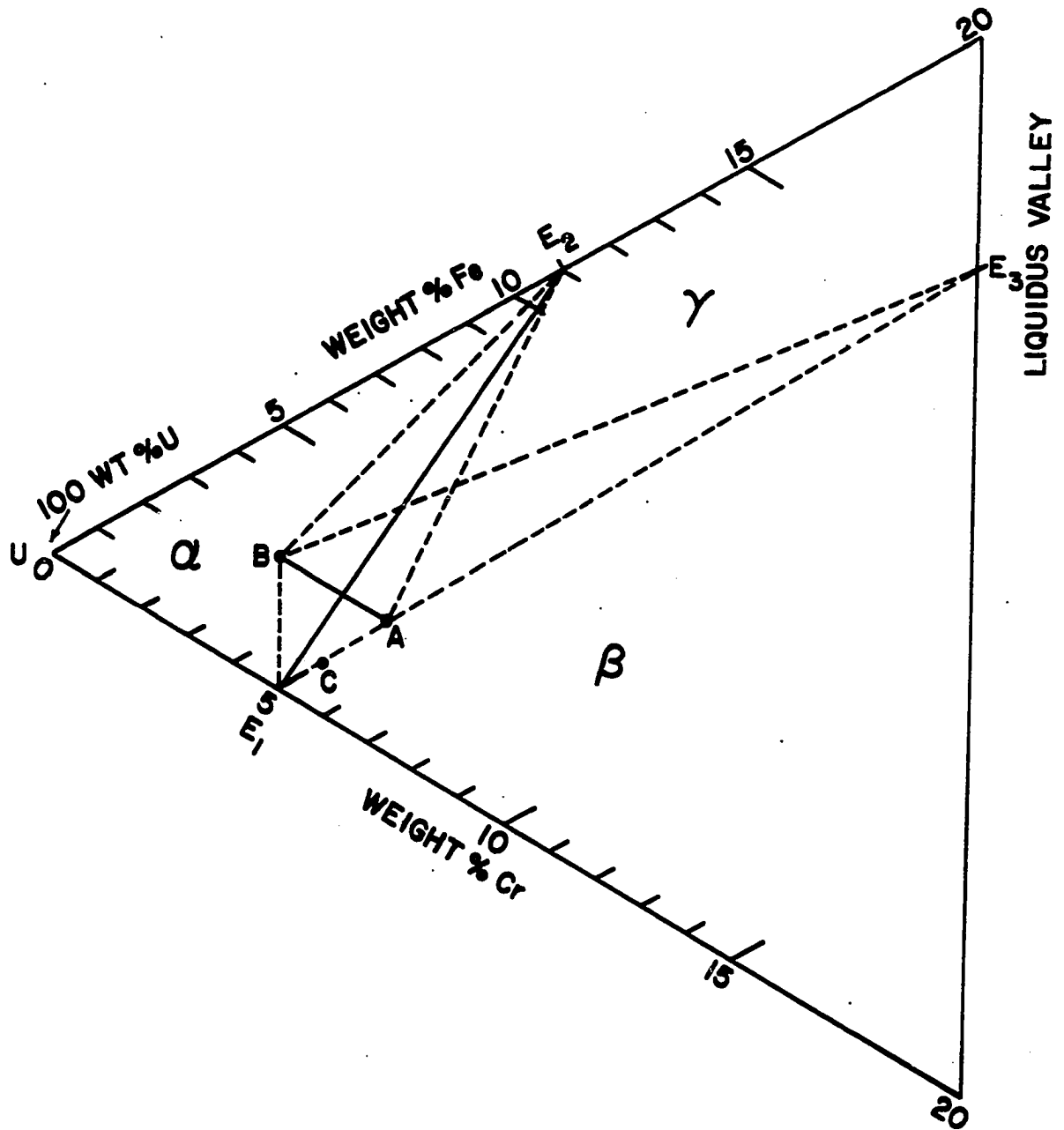
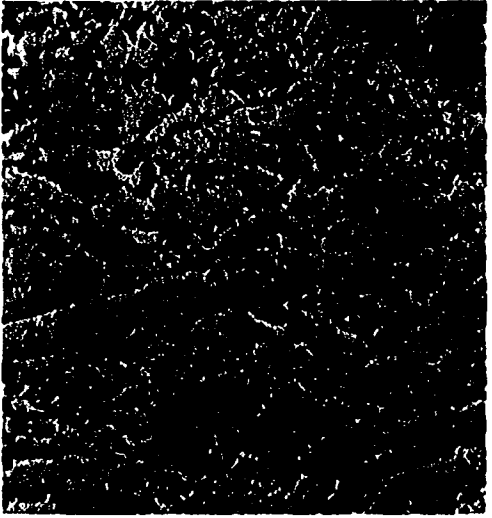


Figure 23. Proposed ternary phase diagram of the uranium-chromium-iron system (tentative)

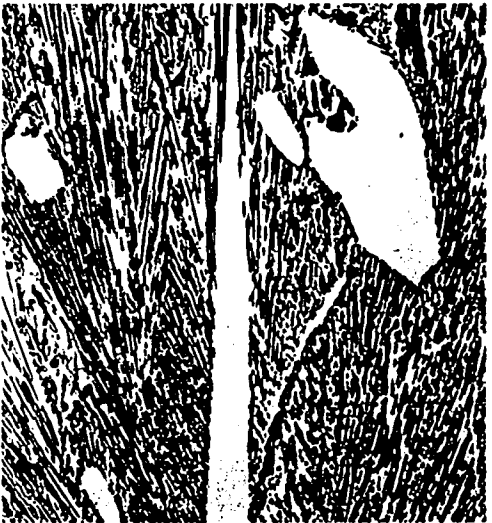
Figure 24. Microstructures of uranium-chromium eutectic and uranium-chromium-iron alloys (as electropolished in 3% perchloric)

- a. Sample C-5: U-Cr eutectic (250X)
- b. Sample C-2: U-Cr-0.25 wt.% Fe (250X)
- c. Sample C-4: U-Cr-1.00 wt.% Fe (250X)
- d. Sample C-8: U-Cr-10.0 wt.% Fe (250X)
- e. Sample C-6: U-Cr-2.50 wt.% Fe (250X)
- f. Sample 0052: U-2.5 wt.% Cr-2.5 wt.% Fe (150X)

.001
.002 INCHES
.003
.004
250 X
.007
.009
.010



.003
INCHES
.010
150 X
.016



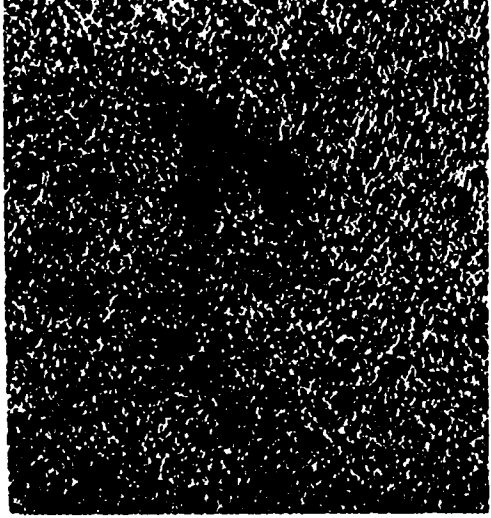
.001
.002 INCHES
.003
.006
250 X
.007
.009
.010



.001
.002 INCHES
.003
.006
250 X
.007
.009
.010



.001
.002 INCHES
.003
.006
250 X
.007
.009
.010



.001
.002 INCHES
.003
.006
250 X
.007
.009
.010



and (b) are possible but that of (c) is impossible.

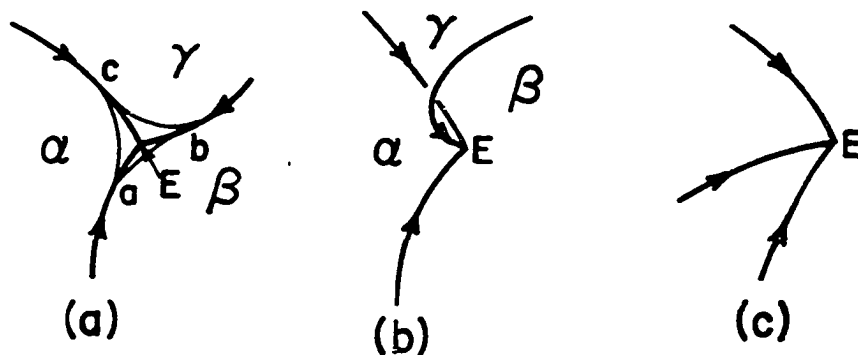


Figure 25. Possible (a and b) and impossible (c) intersections of binary eutectic curves on a ternary eutectic phase diagram

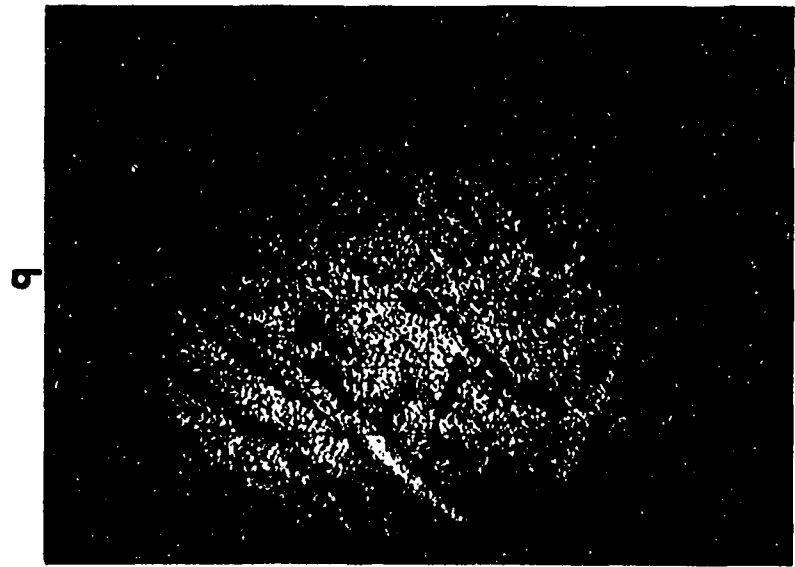
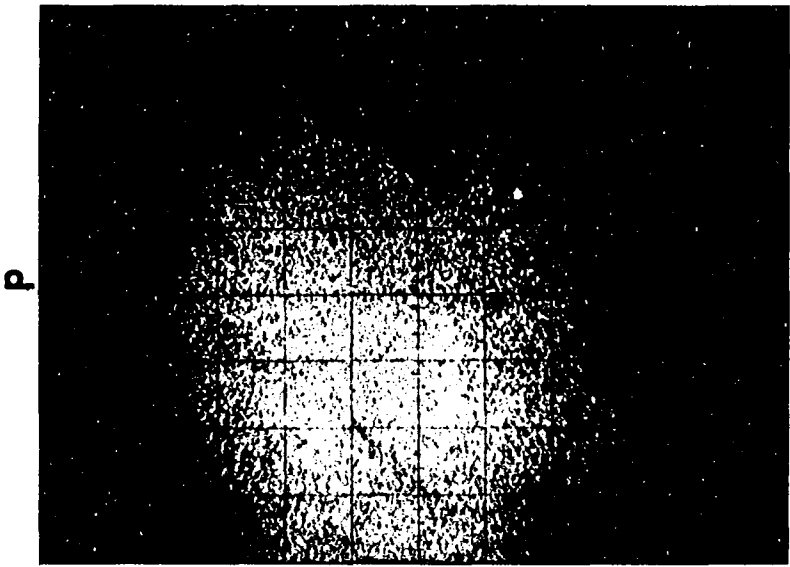
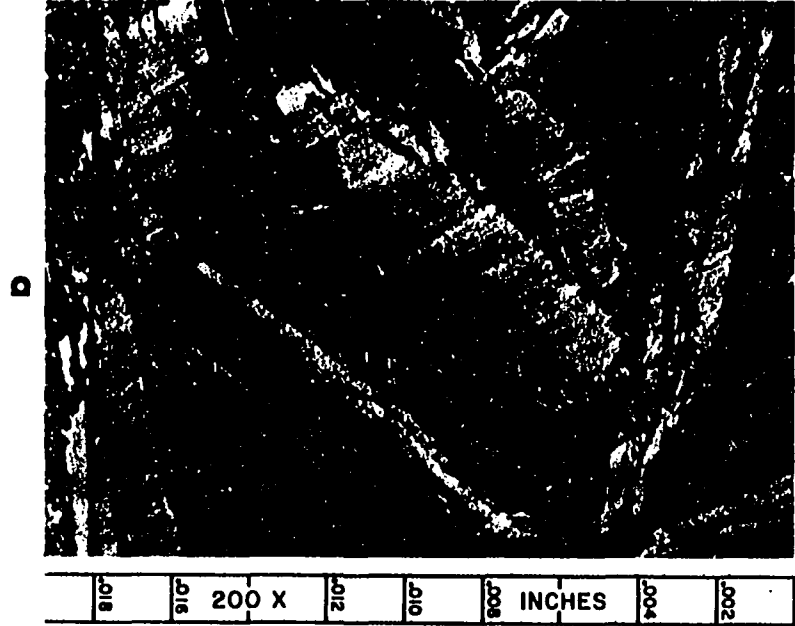
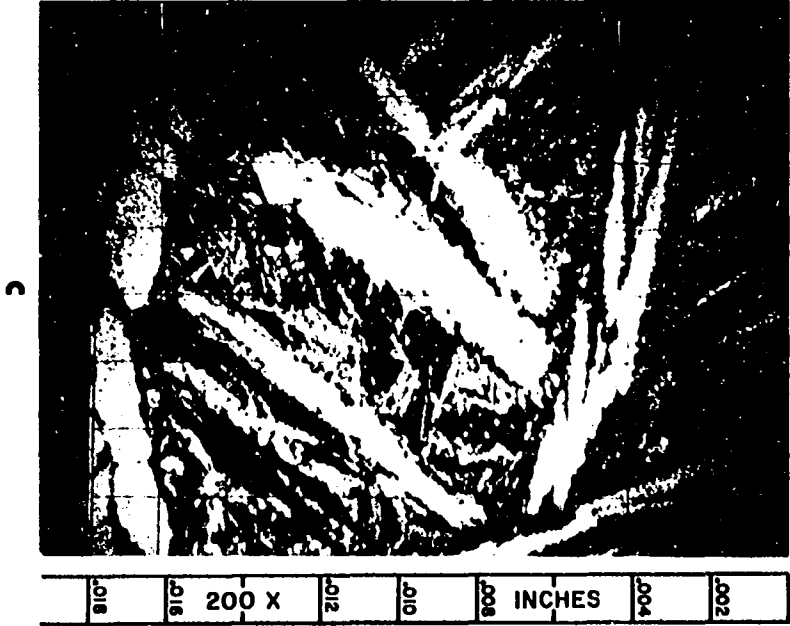
Referring again to Figure 23 in light of Figure 25, Point B might be an impossibility. If it is assumed that the two binary valleys E_1B and E_2B are nearly linear, the eutectic point would have to lie on the right side of the straight line joining E_1 and E_2 . Points A and C fulfill this requirement. The other contingency, of course, is that Figure 25b applies. This is a distinct possibility since the ternary eutectic point E has a melting point (765°C) between E_1 (859°C) and E_2 (725°C). If the binary valleys E_1B and E_2B are not linear but curve appropriately, then Point B is still credible. Without further investigation, various possibilities can only be speculated. Based on the preliminary data from Table 14, the ternary eutectic point lies close to the line AB. Thermal analyses and microscopic examinations show the eutectic to be close to point B.

The photomicrographs shown in Figure 24 illustrate the microstructure of six of the U-Cr-Fe alloys. The pure U-Cr eutectic is shown in view (a). A comparison of (c) with (a) and (b) shows the eutectic structure present is still primary U-Cr eutectic, whereas the surrounding areas contain a nearly uniform distribution of U-Cr-Fe solid solution. The U-Cr eutectic regions were shown to be deficient in iron by microprobe analysis. View (d) shows the microstructure of the 10 wt.% iron addition to the U-Cr eutectic. Beyond about 3.75 wt.% iron the allotropic forms of uranium disappear and are supplanted by U_6Fe and UFe_2 , in that order. The 10 wt.% iron alloy is largely that of the two compounds and chromium. Iron tends to distribute itself quite uniformly with the uranium present, but the chromium tends to segregate for alloys above about 2.5 wt.% iron. This was borne out in microprobe analyses of the various U-Cr-Fe alloys. A vivid illustration of chromium rejection is seen in the sequence of photomicrographs shown in Figure 26.

Figure 26a is a photomicrograph of the area considered in the UCr-2.5 wt.% Fe alloy. From the series of photomicrographs in Figure 24 one might think that the needles in Figure 26a are basically U_6Fe , but the chromium image obtained from the microprobe (Figure 26c) shows an accumulation of chromium at the needles. The uranium and iron distributions tend to be fairly uniform. A semi-quantitative analysis of the needles by the microprobe showed their composition to be approximately 84 wt.% U, 12 wt.% Cr, and 4 wt.% Fe. The composition of the region between needles was shown to be about 95 wt.% U, 4 wt.% Fe, and 0.8 wt.% Cr, or roughly that of the U_6Fe compound.

Figure 26. Photomicrographs of uranium-chromium-2.5 wt.% iron micro-structure analyzed by electron microprobe: Sample 246 (200X)

- a. Photomicrograph of the area scanned by electron beam
- b. Oscilloscope picture of iron image from microprobe showing iron distribution
- c. Oscilloscope picture of chromium image from microprobe: note concentration of chromium in needles
- d. Oscilloscope picture of uranium image showing uniform uranium distribution



It is somewhat surprising that the chromium is rejected from solution on cooling since the Cr-Fe system forms a complete series of solid solutions and the iron and chromium atoms have similar sizes and electronegativities. It is, perhaps, the electronic structures which cause the chromium to be rejected because uranium forms two intermetallic compounds with iron but none with chromium.

The allotropic transformation temperatures of the U-Cr eutectic are not greatly affected by the addition of iron. Heating data show a decrease of approximately 8°C for the $\alpha \rightarrow \beta$ and $\beta \rightarrow \gamma$ transformations for iron additions above 0.25 wt.%. At about 3.75 wt.% iron and above the transformations disappear as shown in Figure 22.

The results of this auxiliary investigation have shown the ternary eutectic point to be near the composition of 95 wt.% U-2.5 wt.% Cr-2.5 wt.% Fe melting at 765°C . This is in contradiction to the literature reported value (51, 95, 96) at 94 wt.% U-5 wt.% Cr-1 wt.% Fe melting at 760°C . The pure U-Cr eutectic composition at 95 wt.% U-5 wt.% Cr was found to melt at approximately 870°C , whereas the literature (42) lists a value of $859 \pm 10^{\circ}\text{C}$ for the melting point.

Corrosion Tests Results

Corrosion by uranium-chromium eutectic

The main purpose of the over-all investigation was to determine the corrosive effect of iron additions to the base U-Cr eutectic alloy contained in yttrium containers. In order to determine these effects it was necessary to know the effect of pure U-Cr eutectic on the yttrium alone. This was accomplished by testing a series of yttrium capsules containing the U-Cr

eutectic for various durations in an isothermal furnace at 950°C. A total of 22 capsules were investigated including three tests conducted by Fisher and Fullhart (7) earlier at the Ames Laboratory. Table 15 is a tabulation of these capsule tests and best summarizes their results. Figures 27, 28, and 29 show various photomicrographs of the samples. In most cases, the area at the interface between the yttrium and U-Cr eutectic is reproduced.

All tests except Samples 279B, 263, and 264 were run as nominally static, isothermal tests. The three exceptions were run isothermally in the 360° rotary apparatus in Furnace No. 4 shown in Figure 19.

In actuality it was impossible to maintain the static capsules at the same temperature from top to bottom. A difference of 1° to possibly 2 or 3°C existed along the length of the capsules which were placed vertically in the furnace. The inside muffle furnace dimensions are 7½ inches wide by 5¼ inches high by 15 inches deep. Nichrome resistance wire is wrapped on the outside of this shell to maintain the temperature as nearly uniform as possible for this type of design. In an experiment conducted several years ago, the author found temperature differentials between the ends of a four-inch Inconel capsule of 0.5 to 3.0°C at various locations in the back-half of the furnace. Such temperature differentials are great enough to cause significant density differences which give rise to convective agitation of the melt. Eldred (71) calculated that a difference of as little as 10^{-3} g/cc in density between the top and bottom of the melt are enough to cause convective currents. It is a well-known fact that the dissolution rate is much greater for an agitated specimen than for an ideally static one. Hence, an increased degree of corrosion attack would be expected at the meniscus. The over-all effect is that a V-form capsule results, enhanced by the fact

Table 15. Results of isothermal yttrium capsule tests with uranium-chromium eutectic^a

Sample number	Temp.	Length of test hours	S/V ratio cm ⁻¹	Type of corrosion	Depth of corrosion		Yttrium in solution ppm	
	°C				≤ ^b inches			
279B ^a	950	0.05	5.50	slight dissolution		< 0.0001	226 ^c	Standard reference sample structure.
150	950	1.0	3.15	dissolution		0.0007	271	Meniscus turned up. Thin probe analysis at 800X.
261	950	50	2.86	dissolution & Si-Y compd	Top Bot	0.0024 0.0010	734	Meniscus turned up slight visible. Thin oxide coat
262	950	175	2.82	"	Top Bot	0.0028 0.001	--	U-Cr wet capsule wall only near interface. Si-Y glob
263 ^a	950	175	7.47	dissolution		0.0007	686	Y surfaces cleaned before thermal grooving. Also s
264 ^a	950	175	7.49	"		0.0012	618	Y capsule oxidized in air cant difference from No.
245	950	300	2.70	dissolution & Si-Y compd	Top Bot	0.0020 0.0017	568	Meniscus was almost flat. Y ppt. along interface an
162	950	504	2.79	"	Top Bot	0.002 0.0017	--	Meniscus turned up. Some
165	950	504	2.68	"	Top Bot	0.0042 0.001	539	Meniscus turned up. First but about the same distan
163	950	988	2.67	"	Top Bot	0.0078 0.0043	--	Meniscus turned up. Si-Y increased attack very not
164	950	988	2.69	"	Top Bot	0.0109 0.0055	--	Meniscus turned up. Y ppt. Si-Y present at the bottc
166	950	1500	2.68	"	Top Bot	0.0028 0.001	--	Meniscus turned up. Cons Y ppt. near meniscus. Th
167	950	1500	2.69	"	Top Bot	0.0118 0.0025	--	Meniscus turned up. Si-Y
168	950	2000	2.69	"	Top Bot	0.0138 0.0044	--	Meniscus turned up. Si-Y clusters of Si-Y. Y ppt.
169	950	2000	2.68	"	Top Bot	0.0164 0.0042	--	Meniscus turned up. Si-Y clusters. Y ppt. floating near
161	950	3000	2.88	dissolution	Top Bot	0.0049 0.0038	458	Meniscus almost flat--turned other capsules near bottc

^aAll capsules were run as nominally static tests except Samples 279B, 263, and 264, which were dynamic.

^bCorrosion penetration listed is the maximum measured along the sectioned capsules' interfaces.

^cYttrium present as an impurity in the uranium before testing was determined to be 113 and 204 ppm.

Remarks

- ard reference sample. See Fig. 27a. Note uniform interface and characteristic U-Cr eutectic micro-
ture.
- cus turned up. Thin layer of oxide coating present. Very slight dissolution attack discerned by micro-
analysis at 800x.
- cus turned up slightly. Increased dissolution attack at meniscus. See Fig. 27b where Si-Y globules are
le. Thin oxide coating present at interface in certain places. Bottom has Si-Y along most of interface.
- et capsule wall only in certain places at meniscus. Y ppt. collected at the meniscus and along the walls
interface. Si-Y globules also present along interface. See Fig. 29d.
- faces cleaned before test--compare with No. 264. Fig. 27c shows typical Y grain-boundary structure and
al grooving. Also see Fig. 29c. Y ppt. visible under microscopic examination.
- sule oxidized in air at 250°C before test. Inner and outer surfaces were bright after test. No signifi-
difference from No. 263. Y ppt. and a few Si-Y globules present under microscopic examination.
- cus was almost flat. Attack along interface nearly equal at top and bottom. Very few Si-Y globules present.
. along interface and floating at meniscus (Fig. 31a).
- cus turned up. Some Y ppt. near interface. Several Si-Y globules present but much less than in No. 165.
- cus turned up. First signs of large amounts of Si-Y globules--rather randomly spaced along the interface,
bout the same distance into the U-Cr. See Fig. 27d. Some pure Y ppt. visible.
- cus turned up. Si-Y globules all along interface. Y ppt. along interface and floating at the meniscus.
ased attack very noticeable at meniscus. See Fig. 27e showing Y and Si-Y globules.
- cus turned up. Y ppt. floating at U-Cr surface. Again increased attack at meniscus. Considerably less
present at the bottom of these samples.
- cus turned up. Considerably less corrosion noticed for this sample and also much less Si-Y present. Some
. near meniscus. Thermal grooving of Y noticeable.
- cus turned up. Si-Y globules abundantly present. Always increased attack near groupings of Si-Y globules.
- cus turned up. Si-Y globules are further from interface with time. Fig. 27f shows increased attack near
ers of Si-Y. Y ppt. at meniscus and near top at the interface.
- cus turned up. Si-Y globules are further from interface in top samples.. Always increased attack at menis-
Y ppt. floating near surface. See Fig.'s 29a, 29b, and 29c showing microprobe verification of Si.
- cus almost flat--turned up in some places, down in others. Less attack near meniscus, but about the same as
capsules near bottom. Si is absent in both top and bottom samples. See Fig. 28a. Y ppt. at surface.
- d 264, which were dynamic tests rotated 360°.
- sules' interfaces.
- to be 113 and 204 ppm from chemical analysis of two separate samples.

Table 15 (Continued)

Sample number	Temp. °C	Length of test hours	S/V ratio cm ⁻¹	Type of corrosion	Depth of corrosion ≤ ^b inches	Yttrium in solution ppm	
170	950	3000	2.68	dissolution & Si-Y compd	Top 0.0157 Bot 0.0044	--	Meniscus turned up. Si deep attack right at me
146 ^d	960	360	-- ^e	"	Top 0.0017 Bot 0.0012	--	Meniscus turned down. interface. No Si near
148 ^d	925	2000	3.9	"	0.0019	--	Meniscus turned up and interface. See Fig. 28
147 ^d	950	3000	2.7	"	Top 0.0079 Bot 0.0110	--	Meniscus turned up. A No. 170. Jagged attack
259 ^f	1200	60	2.6	"	Top 0.0016 Bot 0.0007	1,412	Meniscus turned up. Se U-rich eutectic with Y
260	1200	60	2.7	"	Top 0.0032 Bot 0.0029	2,138	Meniscus turned up. Se Quite uniform attack as

^dSamples 146, 148, and 147 are actual samples run by Fullhart (7, 10).

^eCapsule shape precludes estimation of surface area to volume ratio.

^fSample 259 contained pure uranium as a comparison test of corrosiveness with the U-Cr eutectic

Remarks

turned up. Si-Y compound again present giving increased attack. Y ppt. at meniscus. Fig. 28b shows attack right at meniscus.

turned down. Si-Y globules are present in very slight amount. Y ppt. visible at meniscus and along wall. No Si near bottom (Fig. 28c).

turned up and down. Only 3/16 inch depth of U-Cr in machined Y capsule. Si-Y globules present all along wall. See Fig. 28d. Several areas of increased attack near Y ppt. floating at surface.

turned up. A few Si-Y globules visible. Considerable Y ppt. and Si-Y floating near meniscus--more than in No. 260. Jagged attack on top, but uniform at bottom (Fig. 28e).

turned up. Several Si-Y globules. Y ppt. floating at surface. Little attack compared to No. 260. Eutectic with Y similar to that in Fig. 28f. Some Y grain boundaries transverse width of capsule wall.

turned up. Several Si-Y globules present. Y ppt. at meniscus. U-rich Y eutectic visible (Fig. 28f). Form attack as compared to 950°C samples.

U-Cr eutectic used in Sample 260.

that the density of yttrium is much less than the U-Cr eutectic.

The differences in density of the melt not only arises from the temperature differential present but also because of the difference in composition (more solid metal in solution near the meniscus than near the bottom). The temperature difference is also increased as a result of the positive heat of solution, characteristic of partially immiscible systems such as yttrium--U-Cr. On this basis, then, it is not surprising that each of the static capsules listed in Table 15 shows more severe corrosion and a deeper penetration near the meniscus because of the increased agitation at the surface. Examples are shown in Figures 27b and 28b. Figure 30 is a dual plot of the penetration observed at the meniscus and at the bottom of the static test capsules with time. Some of the points are rather dispersed in nature, but the over-all effect of the corrosion is evident. Since only the maximum penetration and not an average amount is plotted, such a statistical distribution is to be expected. If the tests had all been conducted dynamically, the curves would probably have been more uniform and the amount of corrosion considerably less.

The dynamic capsules, on the other hand, did not exhibit this effect and underwent considerably less corrosion attack although their surface to volume ratios were higher than the static capsules. In essence the static tests conducted in this investigation were a more severe test of yttrium as a container material than the isothermal dynamic tests.

The liquid-metal corrosion attack occurring in this series of tests consisted of dissolution attack which was further complicated by inter-metallic compound formation between impurity silicon and the yttrium. The silicon impurity was discovered by microprobe analyses on a number of

Figure 27. Photomicrographs of interface regions for yttrium corrosion test samples with uranium-chromium eutectic (as electro-polished in 3% perchloric)

- a. Sample 279B, 0.05 hours: note smooth interface of standard test sample for corrosion test series (250X)
- b. Sample 261, 50 hours: near meniscus showing several Si-Y globules and yttrium ppt. (250X)
- c. Sample 263, 175 hours--dynamic test: showing typical grain boundaries and groove angle (250X)
- d. Sample 165, 504 hours: line of Si-Y globules (250X)
- e. Sample 163, 988 hours: Si-Y globules and yttrium ppt. are visible (250X)
- f. Sample 168, 2000 hours: increased attack near cluster of Si-Y globules at bottom (150X)

0.01
0.002 INCHES
0.001
250 X
0.007
0.006
0.010



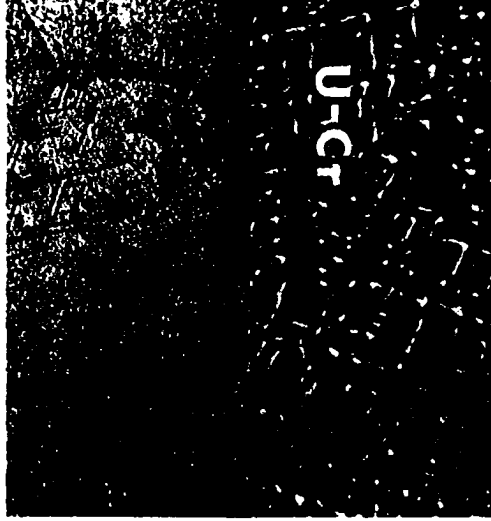
c

0.01
0.005 INCHES
0.010
150 X
0.015



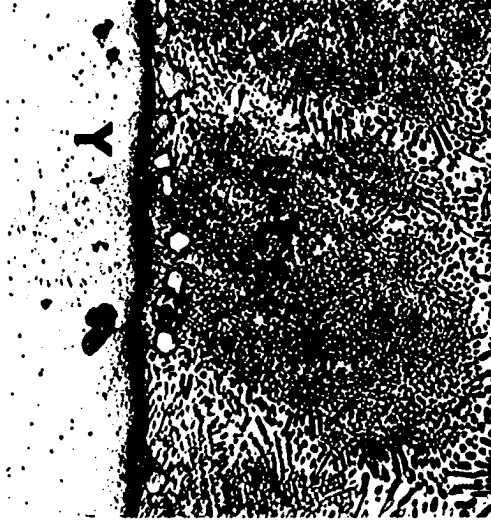
e

0.01
0.002 INCHES
0.001
250 X
0.007
0.006
0.010



d

0.01
0.002 INCHES
0.001
250 X
0.007
0.006
0.010



b

0.01
0.002 INCHES
0.001
250 X
0.007
0.006
0.010

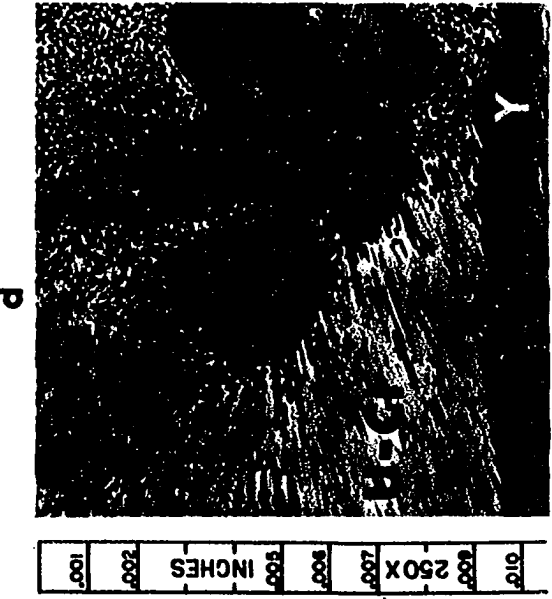
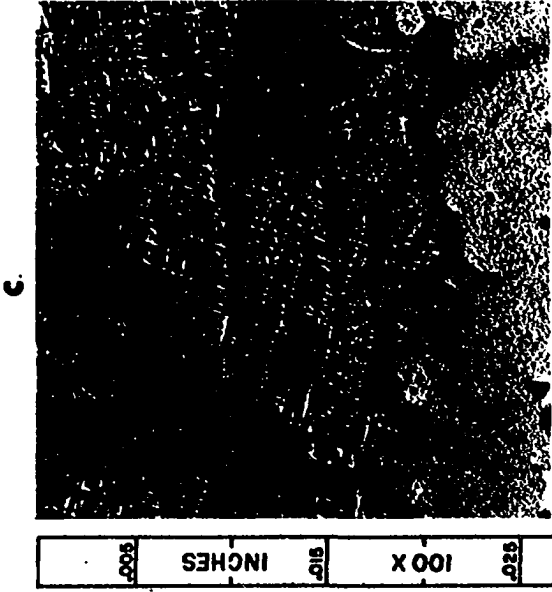
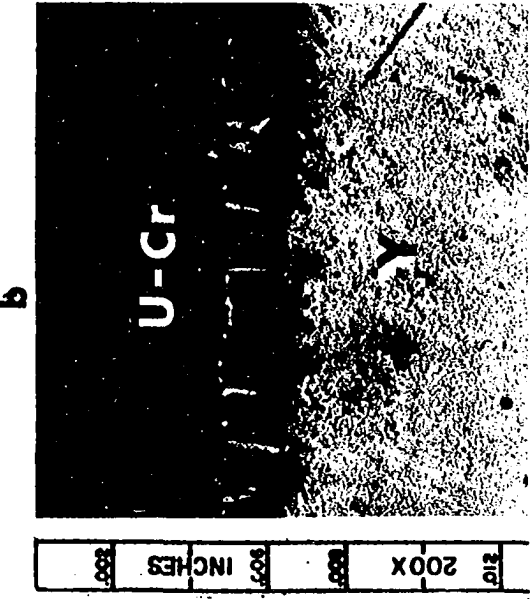
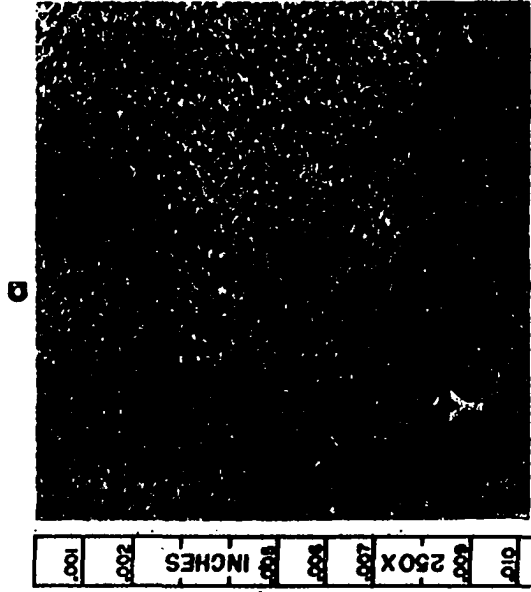
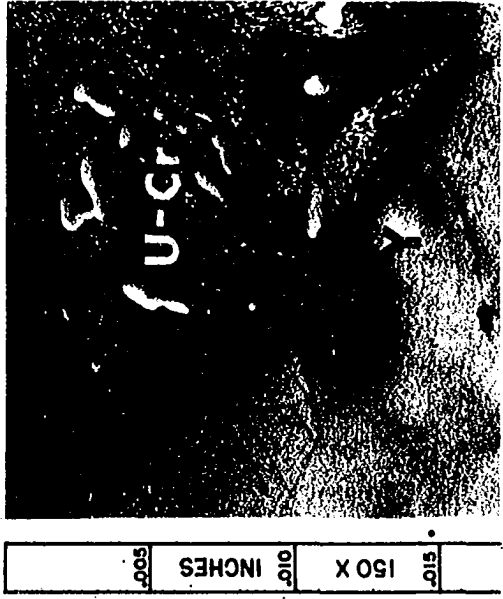
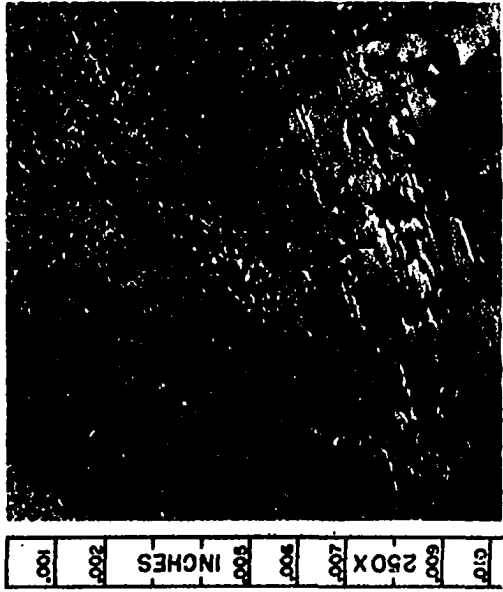


0.01
0.002 INCHES
0.001
250 X
0.007
0.006
0.010



Figure 28. Photomicrographs of interface regions for yttrium corrosion test samples with uranium-chromium eutectic (as electro-polished in 3% perchloric)

- a. Sample 161, 3000 hours: note absence of Si-Y globules and wavy interface characteristic of dissolution attack (near bottom, 250X)
- b. Sample 170, 3000 hours: Si-Y globules and yttrium ppt. present at meniscus--note sharp attack (150X)
- c. Sample 146, 360 hours at 960°C: Si-Y compound at interface near meniscus (250X)
- d. Sample 148, 2000 hours at 925°C: line of Si-Y globules with needle-like structure (bottom, 200X)
- e. Sample 147, 3000 hours: large chunks of yttrium near meniscus level (100X)
- f. Sample 260, 60 hours at 1200°C: yttrium ppt. near meniscus; note U-rich yttrium eutectic microstructure (Xmas tree) in upper left corner (250X)



q

p

f

b

c

e

Figure 29. Photomicrographs of interface regions for yttrium corrosion test samples with uranium-chromium eutectic

- a. Sample 169, 2000 hours: sample current image obtained from oscilloscope of microprobe analyzer showing yttrium, U-Cr, and line of Si-Y compound (400X)
- b. Sample 169, same area as view (a): silicon image obtained from oscilloscope of microprobe analyzer showing presence of silicon (400X)
- c. Sample 169, same area as view (a): yttrium image obtained from oscilloscope of microprobe analyzer showing two distinct regions of yttrium (400X)
- d. Sample 169, 2000 hours: typical yttrium grain microstructure and groove angles; note blip of yttrium unattacked extending to line of Si-Y (100X, as electropolished)
- e. Sample 262, 175 hours: note U-Cr fingers extending into yttrium; globules in bulk of U-Cr are excess chromium crystals (400X, as electropolished)
- f. Sample 169, 2000 hours: yttrium finger engulfed by U-Cr; method of attack preceded by that shown in view (e) above (250X, as electropolished)
- g. Sample 170, 3000 hours: yttrium finger remains unattacked and extends to original interface at line of Si-Y globules (150X, as electropolished)

0.010 0.009 250 X 0.007 0.006 0.005 INCHES 0.004 0.003 0.002 0.001



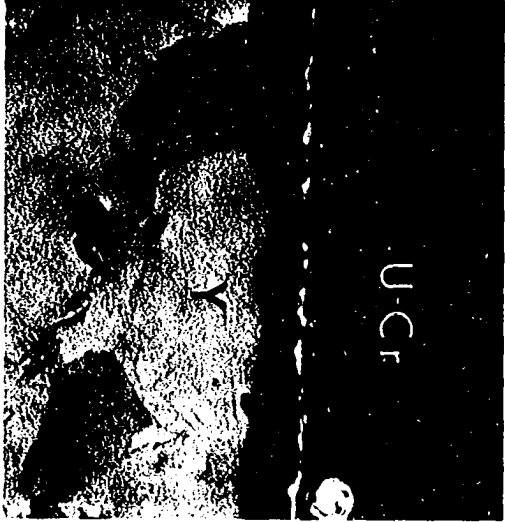
f

0.015 150 X 0.010 INCHES 0.005



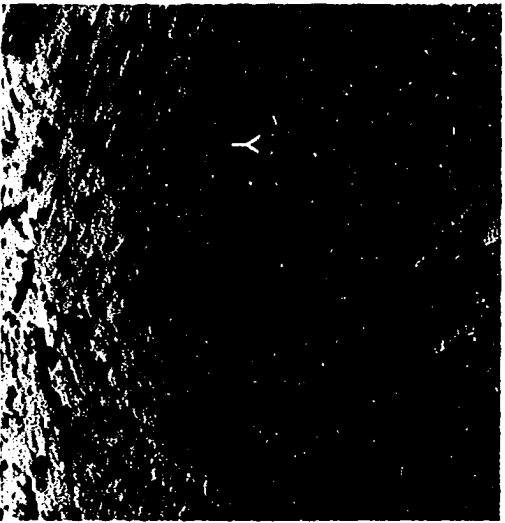
g

0.025 100 X 0.015 INCHES 0.005



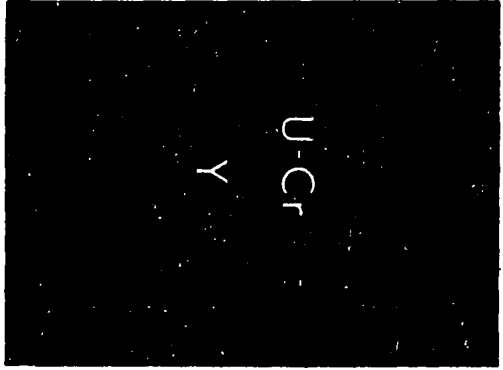
p

0.005 400 X 0.003 INCHES 0.001

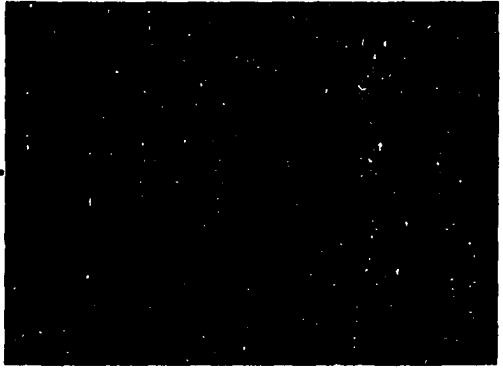


e

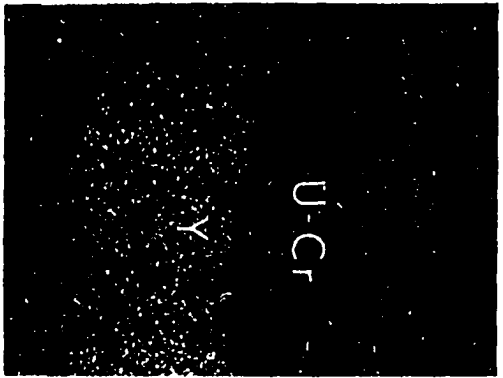
0.005 400 X 0.003 INCHES 0.001



d



b



c

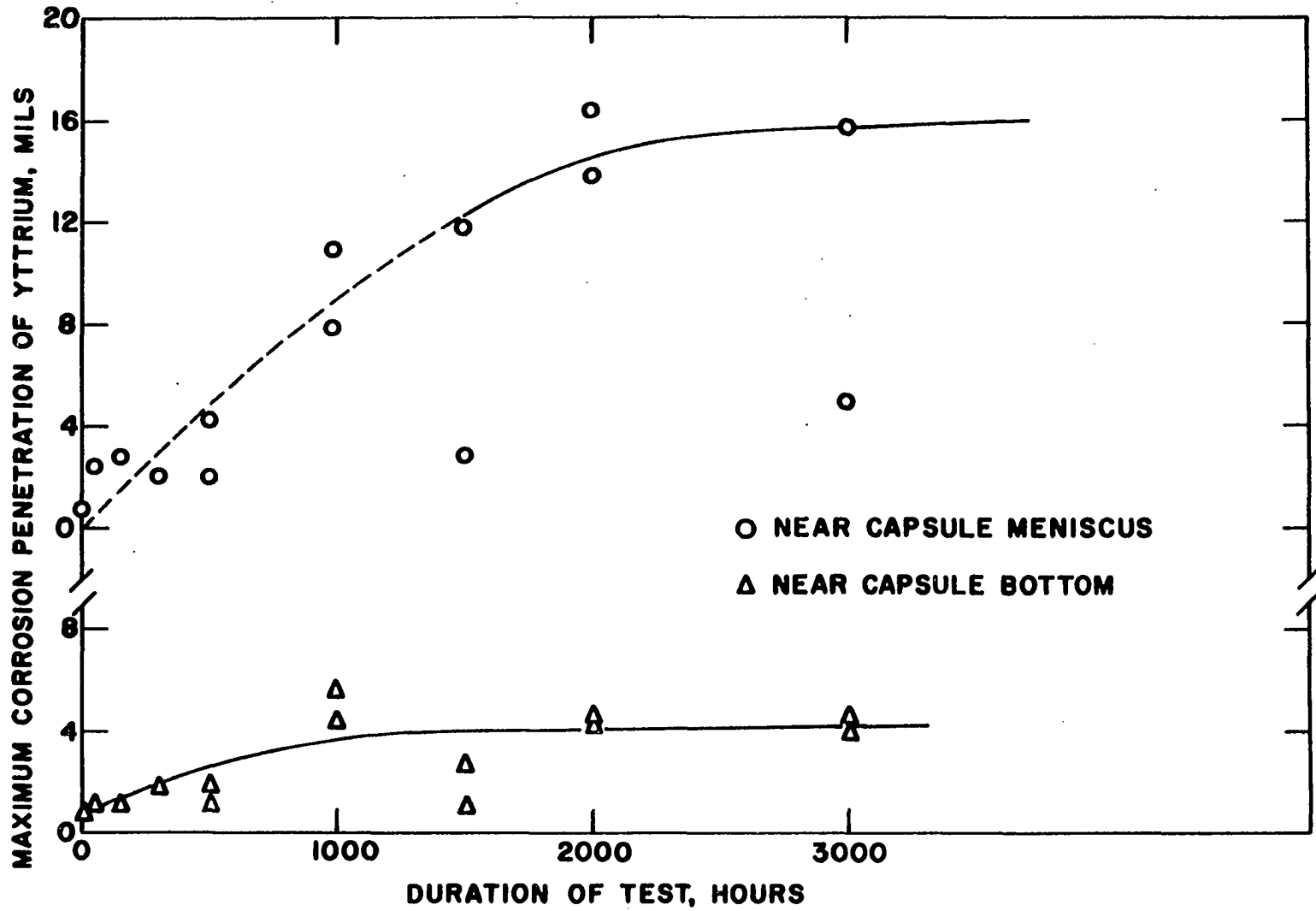


Figure 30. Maximum penetration depth of yttrium walls by the uranium-chromium eutectic with time at 950°C

corrosion specimens. The source of the silicon was traced to the final polishing of the yttrium surfaces with 600 grit silicon carbide (SiC) abrasive paper. Since all capsules including those run by Fisher and Fullhart) were polished with SiC paper, metallographic evidence of silicon was found in nearly all capsules. Only the dynamic tests and Samples 150 and 161 of the static tests were free of the silicon-yttrium (Si-Y) compound globules under microscopic examination, although silicon was undoubtedly present. Yttrium is a rather soft metal and easily becomes embedded with polishing grit even for metallographic preparation. In fact, it was almost impossible to prepare a satisfactory specimen by mechanical means alone. Hence, most specimens were electropolished in a 3% perchloric acid-methanol solution at 60 volts for one minute. This produced a smooth finish for photographing at 500X magnification. Some particles of SiC were still trapped in the microstructure, however, as a result of the initial preparation of the specimens for electropolishing. This grit appears as black spots in several photomicrographs.

The presence of silicon is shown in Figure 29b as the silicon image obtained from the microprobe oscilloscope. The composition of the Si-Y compound was approximately the same in all specimens examined: 22 wt.% Si-75 wt.% Y \pm 2%. This composition corresponds roughly to SiY, a compound of 24.0 wt.% silicon. There are four compounds in the silicon-yttrium system, however, and the Si-Y globules present in the corrosion samples could be a combination of these four.

The first signs of silicon impurity were evident in Sample 261 (Figure 27b). Sample 162 run for 504 hours had just a few globules, but Sample 165 also run for 504 hours had significantly more present. The

amount of Si-Y increased with test duration in all capsules except Sample 161 run for 3000 hours. Silicon grit was probably significantly absent from this capsule when the test commenced. It should be pointed out that the presence of silicon impurity greatly increased the amount of dissolution attack and penetration of the wall. This can be accounted for since once the yttrium had gone into solution in the diffusion band of thickness δ , it was free to react with the silicon present at the interface. The reaction would thus continue until the original silicon disappeared. Actually the silicon was initially present as SiC particles, but since rare earths and yttrium readily react to form carbides at elevated temperatures, a complex reaction probably occurred which resulted in the Si-Y compound. The fact that silicon impurity greatly increases the amount of corrosion is vividly illustrated by comparing Samples 161 and 166, which were free or nearly free of the Si-Y globules, with the other static capsules tests in Table 15. Dissolution attack still occurred in these samples but to a much slighter extent and considerably less penetration was noted for correspondingly equivalent tests.

In comparing the capsules run for various times it was noted that the distance between the Si-Y globules and the interface increased with time. However, there was little tendency for the globules to migrate into the bulk of the melt. In fact, the globules were always found along the interface and never in the bulk of the U-Cr nor floating at the meniscus. The reason the distance increased with time is that the yttrium wall thickness decreased with time. In almost all cases where the Si-Y globules were strung along beside the interface, their position corresponded to the original inner surface of the yttrium. That is, the globules tended to

remain stationary while the yttrium wall suffered dissolutive attack. In the top specimens examined, the Si-Y tended to be spread out because of the increased attack and thermal agitation.

Increased regions of dissolution attack were always noted wherever a cluster of Si-Y globules were present. An example of this is shown in Figure 27f for Sample 168. These regions were especially prevalent in the bottom corners of the corrosion specimens where the bottom cap and side wall met. More silicon was probably present here initially per unit volume of the U-Cr eutectic. Figures 28c, 27d, 29d, and 29g show how the distance between the Si-Y globules and the interface changed with increasing test duration from 360 to 3000 hours.

Another peculiarity noted in a number of the samples is illustrated in Figure 29d where for no apparent reason a small portion of the yttrium is left essentially unattacked. This is shown as a little peak reaching to the line of Si-Y globules and actually contacting them. This same phenomenon is seen again in Figures 27f and 29g.

Sample 263 and 264 were dynamic tests run for 175 hours. Capsule 264 was oxidized in air at 250°C for several hours before charging and sealing. Capsule 263 was cleaned with 600 grit SiC paper just before charging and sealing. After the test period both capsules were bright and shiny and looked the same, inside and outside. A few Si-Y globules were noticed for Sample 264 which suffered slightly more penetration of the wall. Referring to the free energies of formation (110) for the various oxides involved in the system, it is seen that Y_2O_3 is the least stable at 950°C when compared to UO_2 , U_3O_8 , UO_3 , and Ta_2O_5 . Hence, uranium on the inside and tantalum foil on the outside tend to getter the oxygen away from the

yttrium. This is the reason all of the yttrium capsules looked shiny both inside and outside after testing. Thus, after a short period of time Sample 264 essentially acted no differently than Number 263.

Sample 150 run for 1.0 hour had a thin oxide coating (<0.0003 inch) at numerous places along the interface between the yttrium and U-Cr. Sample 261 (50 hours) also had several regions where an oxide film was visible. Further oxide films were not detected on longer duration tests or even the standard reference sample (No. 279B). The dissolution attack was less in the oxide regions indicating that if a stable oxide film could be maintained, reduced corrosion attack would undoubtedly occur. Retaining such an oxide film over long test durations, however, would be rather difficult because of uranium's gettering properties. Theoretically, the uranium atoms could continue to react with the yttrium oxide until all the oxygen had converted to the most stable uranium oxide at the temperature of concern.

Figures 29e, f, and g of three specimens with increasing test periods show the mechanism of the dissolution attack. In Figure 29e it is seen that there are several areas in which a pit or finger of U-Cr has penetrated as much as 0.001 inches into the yttrium wall. (The particles adjacent to the interface in Figure 29e are Si-Y globules, but the phase in the bulk of the U-Cr microstructure is primary chromium which precipitated from the chromium-rich solution upon freezing). When two of these fingers are close together at the interface, they tend to eventually come together as illustrated in Figure 29f, (also Figures 28b, e, and f), encircling a chunk of yttrium and breaking it away from the main body of the wall without completely dissolving it. The chunk of yttrium then tends to float to the

meniscus as seen in Figure 27e or react with the silicon impurity present to form a line of Si-Y globules (Figure 29g).

This phenomenon occurred in most of the samples suffering considerable attack (>0.005 inches penetration). It is a mechanism different from true dissolution attack where corrosion occurs on an atomic basis. It is not a combination of intergranular attack since the fingers occur within the grains, not at the grain boundaries (Figure 29d). In fact, intergranular attack was not found in any of the tests (more on this later). The reason for this type of corrosion is unknown. Perhaps it is the result of energy gradients within or on the surface of individual yttrium grains leading to a type of crystal facet development described by Brasunas (55) for other corrosion systems. Or, it could be caused by localized spots of impurity which form low melting alloys with the U-Cr eutectic. The presence of the silicon impurity might even be responsible.

While some of the chunks present in the samples were formed in this manner, others are probably the result of yttrium precipitating out of solution during the test and at the end when the capsules were quenched. This is undoubtedly true for most of the globules at the meniscus. In one test conducted by the author as a part of another investigation (111), a layer of yttrium had actually covered the whole meniscus area of uranium contained in an yttrium capsule at 1300°C . This could only have formed by yttrium precipitate fusing together with time and as the capsule cooled.

The phenomenon of thermal grooving described in the theoretical section on intergranular attack was observed in a number of the metallographic specimens. Examples of this and the dihedral angles typical of the various specimens are shown in Figures 27c and 29d. The yttrium adjacent to the

interface in these and other photomicrographs was stained during electro-polishing--making it somewhat difficult to see the exact interface. The staining was thought to occur because the yttrium surface was not on the same plane as the U-Cr, but slightly lower. This also accounts for the reason some photomicrographs are not in focus throughout. It is noted that the dihedral angle is considerably greater than 0° or even 90° . This fact coupled with the spectrographic results and $\Delta\bar{H} = 18.7$ Kcal/mole for the U-Y system from Equation 68 shows that intergranular corrosion attack did not occur. Yttrium grain boundaries analyzed by the electron microprobe did not show any signs of uranium or chromium, although aluminum oxide from mechanical polishing was easily recognized. Spectrographic tests of outer yttrium filings did not reveal any uranium lines whereas no significant change in the chromium already present in yttrium could be detected.

The samples run by Fisher and Fullhart (7) are listed in Table 15 as Samples 146, 147, and 148. Here again Si-Y globules were detected microscopically in all three metallographic specimens (Figures 28c, d, and e). The amount of penetration on the long term samples (147 and 148) differed substantially: 0.0019 inch for Number 148 (2000 hours) and 0.0110 inch for Number 147 (3000 hours). However this can be explained as a result of little or no thermal agitation present in Sample 148. Only 3/16 inch depth of U-Cr eutectic was present in the capsule; thus the test was nearly isothermal and essentially static. On the other hand, Sample 147 contained about one inch depth of U-Cr and was seen to undergo 0.0110 inch of penetration. This amount is less than that noticed for Sample 170 but more than Sample 161 both run for 3000 hours. All three of these samples

exhibited the dissolution of large chunks of yttrium, characteristic of the other tests. Yttrium precipitate was also observed floating at the meniscus.

To compare the corrosiveness of U-Cr eutectic with pure uranium in yttrium containers, Samples 259 and 260 were run. Both capsules were run at 1200°C for 60 hours as static, isothermal tests. The increased attack at the meniscus noticeable in the other tests was not nearly as severe in these tests. The corrosion was more uniform although large chunks of yttrium were observed near the interface (Figure 28f). Both samples exhibited an uranium-rich yttrium eutectic microstructure--seen as the dark finger-like structure in the upper left corner of Figure 28f. The experimental solubilities of yttrium in uranium and U-Cr eutectic at 1200°C were 1412 and 2138 ppm, respectively. Equation 25 predicts values of 1404 and 1046 for uranium and U-Cr eutectic, respectively. Again, using the comparison with cerium from Table 7, the yttrium solubilities should be 1078 ppm and 1830 for uranium and U-Cr, respectively. Haefling and Daane (2) got a value 1180 ppm for yttrium in uranium. Equation 25 predicts a value surprisingly close to that obtained with sample 259, but it is also low by a factor of two for U-Cr eutectic. Comparison with cerium shows the proper trend--yttrium solubility higher in U-Cr than uranium, but the values are somewhat low. Yet, this comparison, based on actual experimental results, comes the closest to predicting actual over-all solubility.

In another investigation conducted by the author (111) on the compatibility of molten uranium with yttrium containers at 1150°C and above, tests have been conducted for periods up to 700 hours at 1300°C without capsule failure. In fact, little difference in the degree of attack has been noted between those tests and the tests in this investigation. At

1300°C the largest problem has been the elimination of temperature gradients which cause increased attack at the meniscus. It is evident from the study of the U-Y system that the dissolution of yttrium in uranium is less severe than the dissolution of yttrium in the U-Cr eutectic in this investigation. Hence, the chromium addition to uranium increases the amount of liquid-metal corrosion.

Contrary to data published in the literature the system of U-Cr eutectic in yttrium does undergo liquid-metal corrosion attack. The corrosion mechanism is the dissolution of yttrium metal by solution and diffusion. In this study the corrosion mechanism was followed by intermetallic compound formation with silicon impurity unknowingly introduced as SiC grit from polishing paper. However, even without the silicon impurity yttrium would still suffer dissolutive attack, but not at the rate found in this study. The achievement of a truly static, isothermal test was not possible in the tests conducted. Such conditions are essentially impossible to obtain (63, 71); hence increased attack was always noted at the meniscus level because of thermal agitation. As a result of the solubility tests it was found that the U-Cr eutectic quickly becomes saturated (2 hours) with approximately 760 ppm yttrium after which time attack continues by a thermal-gradient mass transfer mechanism whereby yttrium being the lighter constituent tends to float to the meniscus. Another dissolutive mechanism was also noticed where large chunks of yttrium (< 0.001 inches wide) were observed being engulfed by the melt. Yttrium is more soluble in U-Cr eutectic than pure uranium and appropriately suffers a larger degree of dissolutive attack. The opposite trend was predicted theoretically by Equation 25, but correlation with experimental results on cerium in uranium and U-Cr eutectic

predicts uranium to be less corrosive. A thermal-gradient system incorporating U-Cr eutectic in an yttrium loop would undergo considerable mass transfer with time. Had the two yttrium loops fabricated at the Ames Laboratory (see Review of the Literature) been successful in circulating the U-Cr, plugging would undoubtedly have occurred within several hundred hours because of the large temperature coefficient of solubility for yttrium in U-Cr eutectic.

Corrosion by uranium-chromium-iron alloys

In the previous subsection it was shown that the U-Cr eutectic is more corrosive than pure uranium at 1200°C when sealed in yttrium capsules. In turn the presence of iron in the U-Cr eutectic increases the amount of corrosion further.

Table 16 lists the results of the static capsule tests run with iron additions of 0.02 to 10.0 wt.% to the base U-Cr eutectic. Figure 31 shows several photomicrographs at the interface areas of some of the capsules. Since all the tests in this series were run for 300 hours, the effect of iron concentration on the amount of corrosion which occurs is easy to compare. Figure 32 illustrates this effect as measured near the meniscus and bottom of each capsule tested. The initial trend indicated a gradual increase in penetration depth with additions up to about 4 wt.% iron. Above this amount the penetration begins increasing more rapidly until at 10 wt.% iron the average maximum penetration is about double that at 4 wt.%. This is also typified in Sample Number 276 run with pure uranium-11.0 wt.% iron eutectic for only 60 hours

Table 16. Results of static, isothermal yttrium capsule tests at 950°C with uranium-chromium-iron alloys

Sample number	Iron added to U-Cr wt.%	S/V ratio cm ⁻¹	Type of corrosion	Depth of corrosion		Yttrium in solution ppm	
				Top	Bot		
245	0	2.70	dissolution & Si-Y compd	Top 0.0020 Bot 0.0017	568	Meniscus was almost flat. Attack Y ppt. along interface and floating	
241	0.02	2.74	"	Top 0.0033 Bot 0.0028	--	Meniscus almost flat. Corrosion at interface. Y ppt. at surface, but	
251	0.02	2.75	"	Top 0.0025 Bot 0.0017	--	Meniscus turned down slightly but face. Y ppt. floating near surface	
242	0.25	2.74	"	Top 0.0035 Bot 0.0025	--	Meniscus turned down slightly but face. Y ppt. floating at meniscus	
252	0.25	2.74	"	Top 0.0038 Bot 0.0024	--	Meniscus turned up. Most severe at surface.	
243	0.50	2.76	"	Top 0.0026 Bot 0.0029	--	Meniscus turned up. Attack similar Fig. 31c shows typical interface and	
253	0.50	2.73	"	Top 0.0036 Bot 0.0028	--	Meniscus turned up. Si-Y globules into Y walls near bottom as seen in	
244	1.0	2.78	"	Top 0.0021 Bot 0.0028	1,128	Meniscus turned up. More Y ppt. at where Si-Y globules are present.	
254	1.0	2.75	"	Top 0.0024 Bot 0.0025	--	Meniscus turned down but alloy wet along length of wall. Si-Y globules	
246	2.5	2.77	"	Top 0.0054 Bot 0.0021	1,036	Meniscus turned up. Most severe at scarce especially at bottom. Also	
256	2.5	2.74	"	Top 0.0057 Bot 0.0036	--	Meniscus almost flat, but alloy wet face in Y microstructure (Fig. 31e)	
247	5.0	2.79	"	Top 0.0063 Bot 0.0037	--	Meniscus turned up. Fractures visible (Fig. 31f). Regions of engulfment	
257	5.0	2.76	"	Top 0.0064 Bot 0.0032	--	Meniscus turned up in some areas, rather scarce near bottom. Somewhat	
248	10.0	2.75	"	Top 0.0092 Bot 0.0083	--	Meniscus turned up. Numerous fractures along interface somewhat randomly	
258	10.0	2.75	"	Top 0.0120 Mid 0.0136 Bot 0.0081	11,400	Meniscus wet walls. Fractures visible. One area of increased attack	
276 ^c	11.0	4.34	dissolution	> 0.050	--	Massive dissolution and possibly almost consumed by the corrosion.	

^aAll tests except 276 were conducted for 300 hours.

^bCorrosion penetration listed is the maximum measured along the sectioned capsules' interfaces.

^cSample 276 was run at 950°C for 60 hours with U-11.0 wt.% Fe eutectic to check the compatibility between

Remarks

most flat. Attack along interface nearly equal at top and bottom. Very few Si-Y globules present. Surface and floating at meniscus (Fig. 31a).

flat. Corrosion attack near meniscus about the same as at bottom. A few globules visible adjacent to top at surface, but only several globules along interface.

down slightly but alloy wet walls. More attack at meniscus. Several Si-Y globules present along interface near surface; Fig. 31b--black particles in melt are Y ppt. at meniscus.

down slightly but alloy wet walls. Increased attack at meniscus. Several Si-Y globules along interface at meniscus and some also along interface independent of Si.

up. Most severe attack at the meniscus. Only a few Si-Y globules along interface. Y ppt. at

up. Attack similar up and down the interface. Very few Si-Y globules. Y ppt. again at the surface. Typical interface and dihedral angles.

up. Si-Y globules very scarce. Y ppt. at meniscus and along interface. U-Cr fingers projecting from bottom as seen in Fig. 29d.

up. More Y ppt. along interface than previous capsules. One area near bottom with increased attack. Globules are present. Y ppt. at meniscus.

down but alloy wet walls. Attack at top was greatest somewhat below meniscus. Attack about the same all wall. Si-Y globules present at the interface and Y ppt. floating at the surface (Fig. 31d).

up. Most severe attack at meniscus. Y ppt. floating in thin layer at surface. Si-Y globules rather few at bottom. Also reduced attack at bottom.

flat, but alloy wet walls. Most severe attack at meniscus. Areas where alloy is engulfed below interface structure (Fig. 31e). Y ppt. layer at surface. Si-Y globules along interface.

up. Fractures visible in alloy indicating brittleness. Si-Y globules and Y ppt. strung along interface. Regions of engulfed alloy (see discussion).

up in some areas, down in others. Fractures visible. Si-Y globules and Y ppt. abundant near top but few near bottom. Somewhat less attack at bottom. Alloy engulfed near top.

up. Numerous fractures in alloy. Large layer of Y ppt. at surface. Si-Y globules and Y ppt. strung somewhat randomly rather than tied together. Slightly more attack at meniscus. Y ppt. in alloy bulk.

fls. Fractures visible. More attack at meniscus. Y ppt. at surface and along walls with Si-Y globules. Some of increased attack near cluster of Si-Y near middle. Y ppt. in bulk of the alloy.

tion and possibly compound formation caused capsule failure. Walls were completely penetrated and destroyed by the corrosion. Alloying occurred with the Inconel sheath. Specimens were not analyzed.

s' interfaces.

the compatibility between yttrium and U-Fe alone without chromium present.

Figure 31. Photomicrographs of interface regions for yttrium corrosion test samples with uranium-chromium-iron alloys (as electropolished in 3% perchloric)

- a. Sample 245, U-Cr eutectic: comparison sample for U-Cr-Fe corrosion series; black spots are yttrium ppt. discolored from electropolishing (250X)
- b. Sample 251, U-Cr-0.02 wt.% Fe: meniscus region showing yttrium ppt., groove angle, and excess chromium in liquid-metal bulk (250X)
- c. Sample 243, U-Cr-0.50 wt.% Fe: meniscus region--note groove angles and increased attack (250X)
- d. Sample 254, U-Cr-1.00 wt.% Fe: meniscus region showing yttrium chunks and increased attack (250X)
- e. Sample 256, U-Cr-2.50 wt.% Fe: note regions of engulfed alloy; yttrium has probably precipitated from solution upon cooling (250X)
- f. Sample 247, U-Cr-5.00 wt.% Fe: Si-Y globules in U-Cr-Fe bulk indicating original interface position (250X)

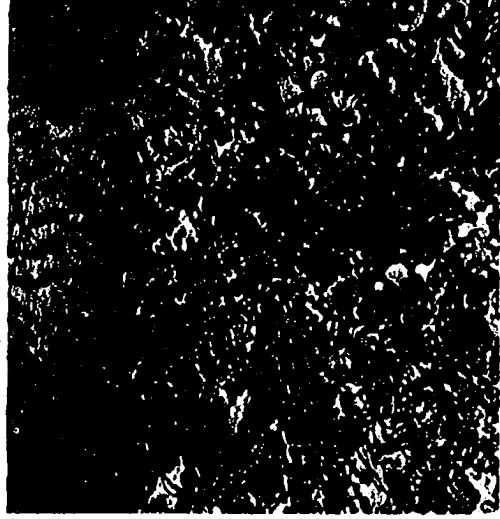
010 250X 007 006 INCHES 002 001



g

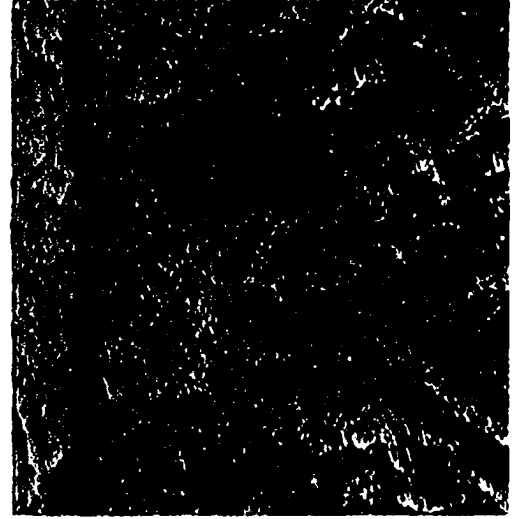
c

010 250X 007 006 INCHES 002 001



d

010 250X 007 006 INCHES 002 001



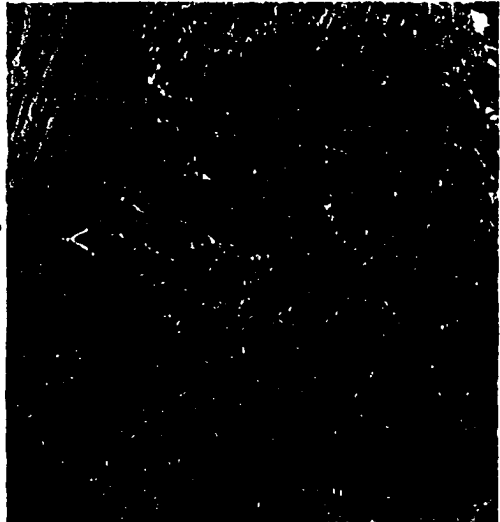
010 250X 007 006 INCHES 002 001



f

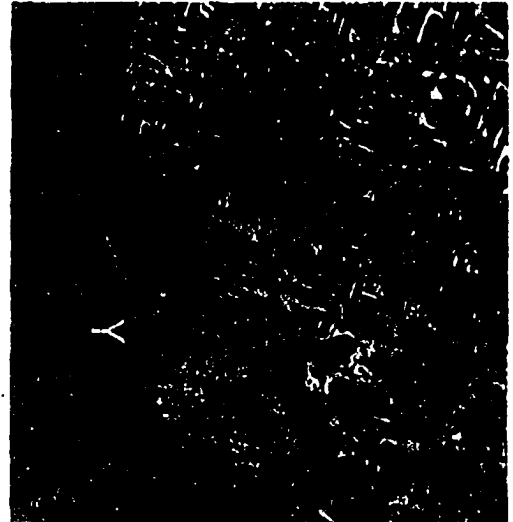
p

010 250X 007 006 INCHES 002 001



b

010 250X 007 006 INCHES 002 001



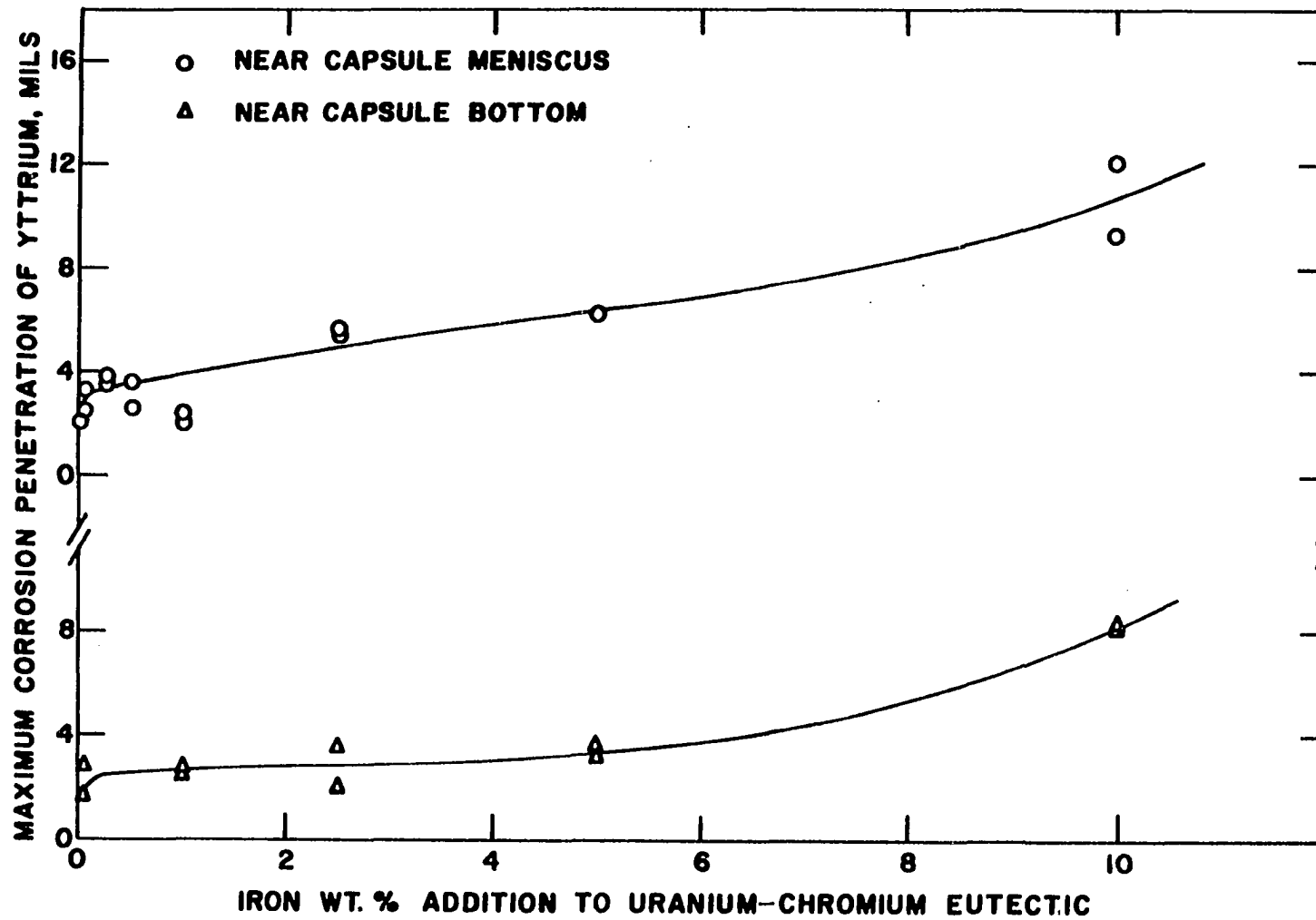


Figure 32. Maximum penetration depth of yttrium wall by uranium-chromium-iron alloys after 300 hours at 950°C

at 950°C which completely penetrated the 0.050 inch wall thickness. The presence of chromium reduces this devastating type of corrosion.

The principal corrosion mechanism was dissolution attack although some intermetallic-compound formation occurred between the yttrium and silicon impurity present as a residue from polishing the inner surfaces with 600 grit SiC paper. This compound formation was more prevalent in the higher wt.% iron tests equaling the amounts in the 2000 and 3000 hour tests with U-Cr eutectic (Table 15).

In all of the metallographic specimens examined, only several cluster areas were found where a gathering of Si-Y globules had caused increased attack. Normally the globules were strung along the interface. Their composition was approximately 20 to 24 wt.% Si-75 wt.% Y. Gathering of globules in the bottom corners as noted for the U-Cr tests was not found.

The most severe attack again occurred at the meniscus level because of the thermal gradient and effects of solution discussed previously. Yttrium precipitate was visible at the surface of each capsule. This increased with iron concentration indicating increased dissolution attack. There was no metallographic, spectrographic, or microprobe evidence of intergranular penetration. Typical yttrium grain boundary structures are seen in Figures 31b, c, d, and e. The dihedral angles are seen to be appreciably greater than 90°, and thermal grooving which was expected is also noticeable. The presence of intermetallic compounds between iron and yttrium, although possible (Figure 4), was not detected. Usually any compound of this nature which forms with a constituent of the fuel alloy will form an adherent layer at the interface. None are detectable in the photomicrographs of Figure 31, either as an adherent layer or as globules

except for Si-Y globules. The microprobe also corroborated this finding.

Difficulty was encountered in the analytical separation of dissolved yttrium from the U-Cr-Fe alloys, because of the presence of the iron. Hence, only three determinations were made. These values represent the approximate equilibrium solubility of yttrium in the U-Cr-Fe alloys at 950°C. A 10 fold increase (11,400 ppm) is noted for the 10 wt.% iron sample over that for the 2.50 wt.% sample (1,036 ppm). As a comparison the U-Cr sample (No. 245) had only 568 ppm yttrium. The difference between the 1.0 wt.% and 2.50 wt.% samples (92 ppm) is probably not significant because of the difficulty in determining yttrium concentrations. Both samples at 1.0 wt.% iron suffered less corrosion attack than their adjacent composition samples, but not a significant amount.

In Figure 31e the phenomenon of engulfment by the U-Cr-Fe is seen for Sample 256. In this instance a line of U-Cr-Fe is shown below the interface. Surprisingly it appears as if the U-Cr-Fe has slipped under the interface since several needle-like structures are seen projecting through the interface into the line of U-Cr-Fe globules below the yttrium surface. This may be the result of yttrium (possibly with silicon) precipitating out of solution and attaching to the wall upon cooling. In the process some U-Cr-Fe alloy becomes engulfed within the yttrium. If this, indeed happens, the yttrium probably starts attaching to the wall before the U-Cr-Fe alloy becomes completely solidified. This entrainment was especially noticeable in the 2.5 and 5.0 wt. % iron samples, but was absent in the 10.0 wt.% sample. It could be associated with the samples containing a large amount of Si-Y close to the interface, whereas in the 10.0 wt.% samples the globules were further from the interface and could not attach

so readily to the wall. The statement that the globules may have been molten is upheld by their rounded shape--nearly spherical for small globules. In all the tests with uranium fuels, the precipitate was hampered from floating to the surface of the melt by the high viscosity of the molten alloys (calculated to be approximately 4.95 centipoise for U-Cr and 4.12 centipoise for U-Cr-Fe at 950°C--rather high values for liquid metals).

The results of this phase of the investigation have shown that iron increases the rate of corrosion attack to yttrium when added to the U-Cr eutectic. Increasing the amount of iron increases the rate of attack. The mechanism of corrosion was dissolution attack complicated by intermetallic compound formation with silicon impurity unsuspectingly introduced from SiC polishing paper. No compounds of iron-yttrium were detected although four or more exist in the system. Intergranular penetration was not detected by spectrographic and microprobe analyses. Thermal agitation from a finite temperature gradient caused generally increased attack at the meniscus level. Pure U-Fe eutectic is very corrosive to yttrium, whereas the presence of chromium greatly reduces the corrosion attack. Yttrium solubility increases from about 760 ppm in pure U-Cr to over 1.1 wt.% for the 10 wt.% iron alloy. Theoretically, Equation 25 predicts an opposite trend with a value of 244 ppm for the 1.0 wt.% iron alloy as compared to 1128 ppm found experimentally. No other known experimental data are available for comparison.

Solubility Test Results

In order to determine the theoretical amount of dissolution attack expected with U-Cr eutectic in yttrium it was necessary to obtain a plot

of yttrium in solution versus time. The data were obtained by equilibrating U-Cr in yttrium capsules for various times and in turn analyzing the melt for yttrium concentration. Since iron greatly interferes with the determination of yttrium in U-Cr-Fe alloys¹, a solubility study was not conducted with the ternary eutectic. Based on the present corrosion test results, however, the dissolution-rate constant, α , would be greater than that for U-Cr eutectic alone.

The analytical values obtained for the various test temperatures and times are shown in Table 17. A plot of the data is illustrated in Figure 33. Since the U-Cr had some yttrium present as an impurity before testing, the time was corrected to allow for this. As corrected, the curve corresponds to Equation 47 with $\alpha = 0.0138$ cm/min and $n_0 = 760$ ppm, where it was assumed $n_t = 0$ at $t = 0$. Without time correction the integration leading to Equation 47 would yield

$$n_t = 760 [1 - 0.792 \text{Exp}(-0.0758t)] \text{ ppm.} \quad (75)$$

Table 18 lists the values obtained from the solubility tests using the radioactive tracer technique. This method was abandoned after conducting only eight tests because the carrier and separation processes took 10 to 12 days to accomplish before the yttrium-90 activity of the samples could be measured. Furthermore, the graphite crucibles greatly interfered with the dissolution of yttrium by the U-Cr as seen by comparing Sample 277 (which was run in a tantalum capsule) with Samples 268, 269, and 274. All four tests were run for 60 minutes at 950°C.

¹F. W. Sealock, Ames Laboratory, Ames, Iowa. Determination of yttrium concentrations in U-Cr-Fe alloys. Private communication. 1968.

Table 17. Analytical solubility values obtained from the solubility test runs^a

Sample Number ^b	Temperature °C	°K	$10^3/T$ °K ⁻¹	Test duration minutes	Yttrium concentration ppm
Blank	--			0	204
Blank	--			0	113
279 B	950			3	226
285	950			3	212
286	950			6	248
289	950			10	489
287	950			18	721
288	950	1223	0.8177	30	466
280	950			45	740
291	950			60	344
292	950			60	755
290	950			90	697
284	950			120	772
278	900	1173	0.8525	30	266
283	1000	1273	0.7856	30	930
281	1050	1323	0.7559	30	1144
282	1100	1373	0.7283	30	890

^aThe surface to volume ratio for all samples was 5.50 cm^{-1} .

^bAll test capsules were rotated 360° at 3.0 rpm which corresponds to a U-Cr velocity of approximately 0.66 cm/sec along the midline of the capsule wall.

The values in Table 18 yield only a partial exponential curve, but the initial approximate slope gives a value of $\alpha \approx 0.001 \text{ cm/min}$. This is low by a factor of about 15 in comparison with α obtained by the analytical method. When the values determined in the graphite crucibles are weighted according to what might be expected from the results of the tantalum capsule, $\alpha \approx 0.017 \text{ cm/min}$ which is more in line with the value determined by the analytical method. The value of α determined

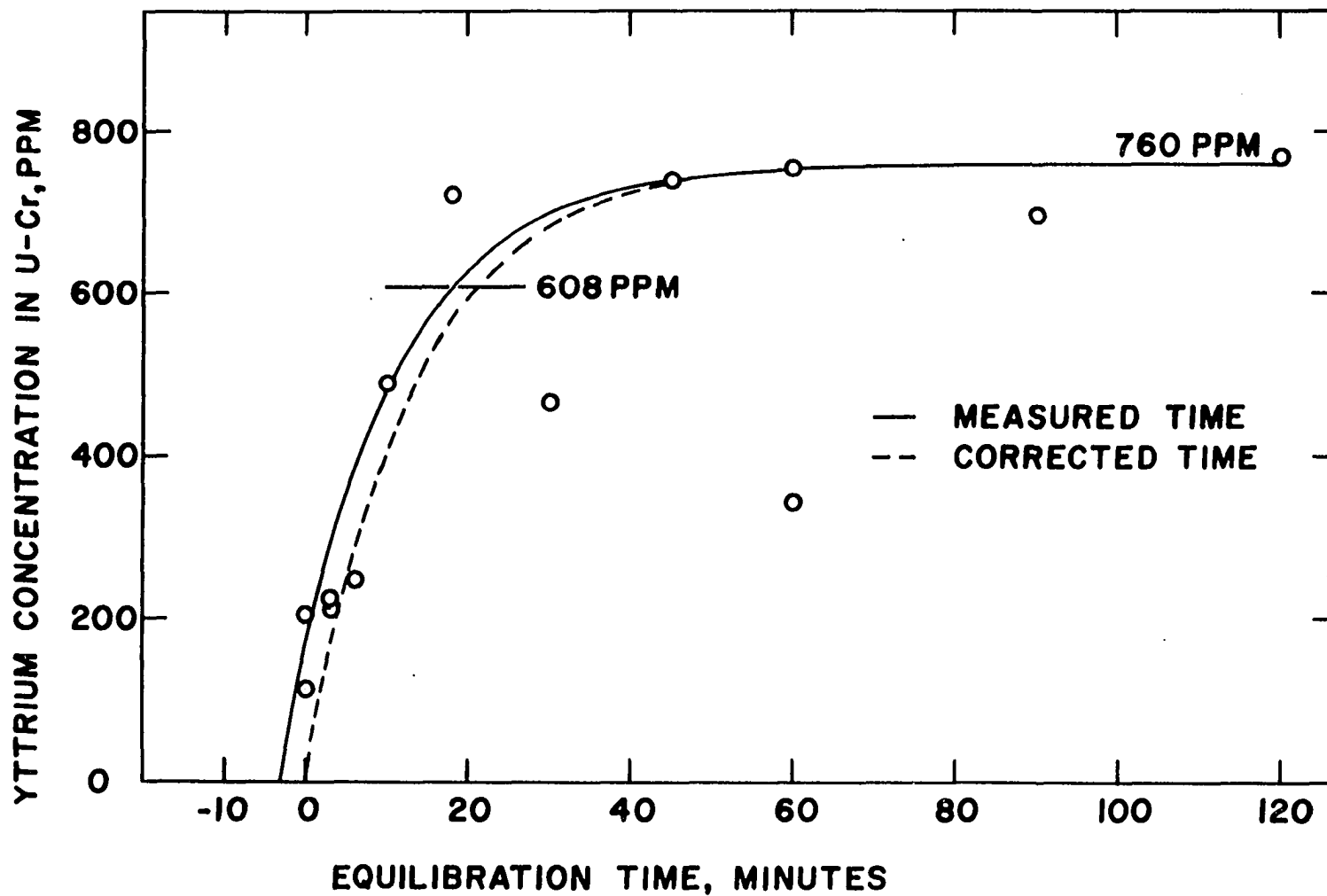


Figure 33. Yttrium concentration in uranium-chromium eutectic at 950°C with time

by the radioactive tracer technique is also in error because this method does not account for the original yttrium present as impurity in the U-Cr (≈ 160 ppm). Hence, the slope determined is not the true initial slope for the curve.

Table 18. Yttrium solubility in U-Cr eutectic at 950°C by the radioactive tracer technique^a

Sample Number ^b	Test duration minutes	Yttrium concentration ^c ppm	Weighted yttrium ^d concentration
271	10	0.3	5.4
270	30	6.5	116.7
268	60	8.4	149.5
269	60	9.7	172.6
274	60	11.1	198.1
277	60	173.4 ^e	173.4
272	240	20.0	356.9
275	1440	259.7	--

^aThe surface to volume ratio was 0.65 cm^{-1} for all samples.

^bAll test capsules were cycled 270° ; one cycle each 25 seconds.

^cYttrium concentration listed accounts only for yttrium which went into solution during the test and not for any yttrium originally present as impurity in the U-Cr eutectic.

^dValues determined by weighting original concentration values on the basis of the results of the 60 minute tantalum capsule using the average concentration value obtained with the 3 graphite crucibles at 60 minutes; weighting factor = 17.85.

^eSample 277 was run in a tantalum capsule whereas the other tests were conducted in graphite crucibles.

Comparison of Sample 277 with the analytical solubility tests can be made using Figure 33. Based on $S/V = 0.65\text{ cm}^{-1}$ for Sample 277 and $S/V = 5.5\text{ cm}^{-1}$ for the analytical tests, Sample 277 should have accumulated

yttrium into solution about $5.5/0.65 = 8.46$ times slower than a corresponding 60 minute analytical test. This corresponds to a $60/8.46 = 7.1$ minute value on Figure 33. Using the corrected time curve and adding the average initial yttrium concentration to Sample 277 yields $158 + 174 = 332$ ppm which corresponds very closely to the value of 320 ppm obtained from the curve. Thus, the two methods seem to give reproducible results if tantalum holding capsules are used for the radioactive tracer method.

A curve of the reduced concentration (n_t/n_x) against the reduced time (t/t_x) is shown in Figure 34 which was plotted from the data in Table 19. This curve follows from Equation 57 where $x = 0.8$, $n_x = 608$ ppm, and $t_x = 21.2$ minutes. Because this expression is independent of geometry and test conditions, one can extrapolate from the curve complete concentration-time data for other temperatures from limited experimental data. Provided the equilibrium concentration and time required to reach saturation are known, one can obtain a fairly precise concentration-time relationship for the system in question.

The above knowledge could be used to determine the relationship of the dissolution-rate constant with temperature, if the time to reach the saturation concentration n_0 were known. This was only determined for 950°C in this study, so the reduced curve can not be used. However, α can be determined from the results of the 30 minute tests listed in Table 17, and a knowledge of n_0 at each temperature. The saturation concentration is determined from Figure 35 by extrapolating from the values at 950°C and 1200°C obtained in this study: 760 ppm and 2138 ppm (Sample 260), respectively. Comparison of the curve obtained in this manner is also

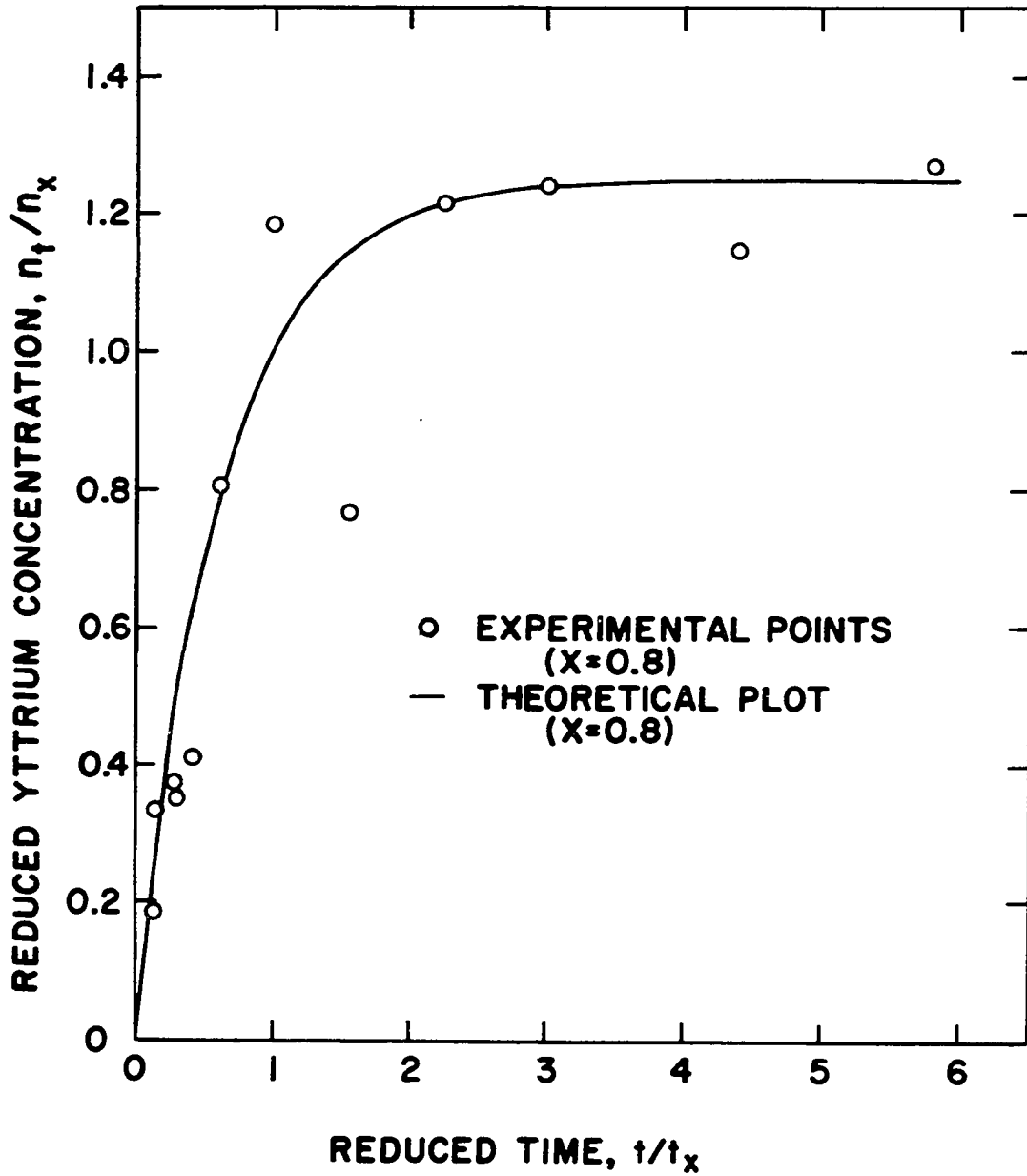


Figure 34. Reduced concentration-time curve for the system of yttrium in uranium-chromium eutectic

made with the solubility predicted by Equation 25 (already seen to be too low) and that by the correlation with cerium in uranium and U-Cr eutectic from Table 7 (apparently more in line with actual values).

Table 19. Reduced data for yttrium in U-Cr eutectic at 950°C^a

Measured time t_m minutes	Corrected time t_c minutes	Concentration n_t ppm	Reduced time t_c/t_x	Reduced concentration n_t/n_x	Theoretical reduced conc. $(n_t/n_x)^b_{\text{theor.}}$
-3	0	0	0	0	0
0	3	113	0.142	0.186	0.255
0	3	204	0.142	0.336	0.255
3	6	226	0.283	0.372	0.457
3	1	212	0.283	0.349	0.457
6	9	248	0.425	0.408	0.619
10	13	489	0.613	0.804	0.784
18	21	721	0.991	1.186	0.996
30	33	466	1.557	0.766	1.148
45	48	740	2.264	1.217	1.217
60	63	755	2.972	1.242	1.240
90	93	697	4.387	1.146	1.249
120	123	772	5.802	1.270	1.250

^aReduced data calculated for $x = 0.8$, $n_x = 608$ ppm, and $t_x = 21.2$ minutes.

^bDetermined from Equation 5.

Using the values for n_t obtained at 30 minutes (33 minutes--corrected time) from Table 17, α was calculated using Equation 49. Table 20 and Figure 36 show the results of these calculations. Because of the variance in the five experimental values, the semilog plot was rather indefinite; however, the slope of the best straight line through the points yields an activation energy of $\Delta E \approx 33$ Kcal/mole. This value, is probably high for several reasons. First, the values at 900, 950, and 1100°C are low.

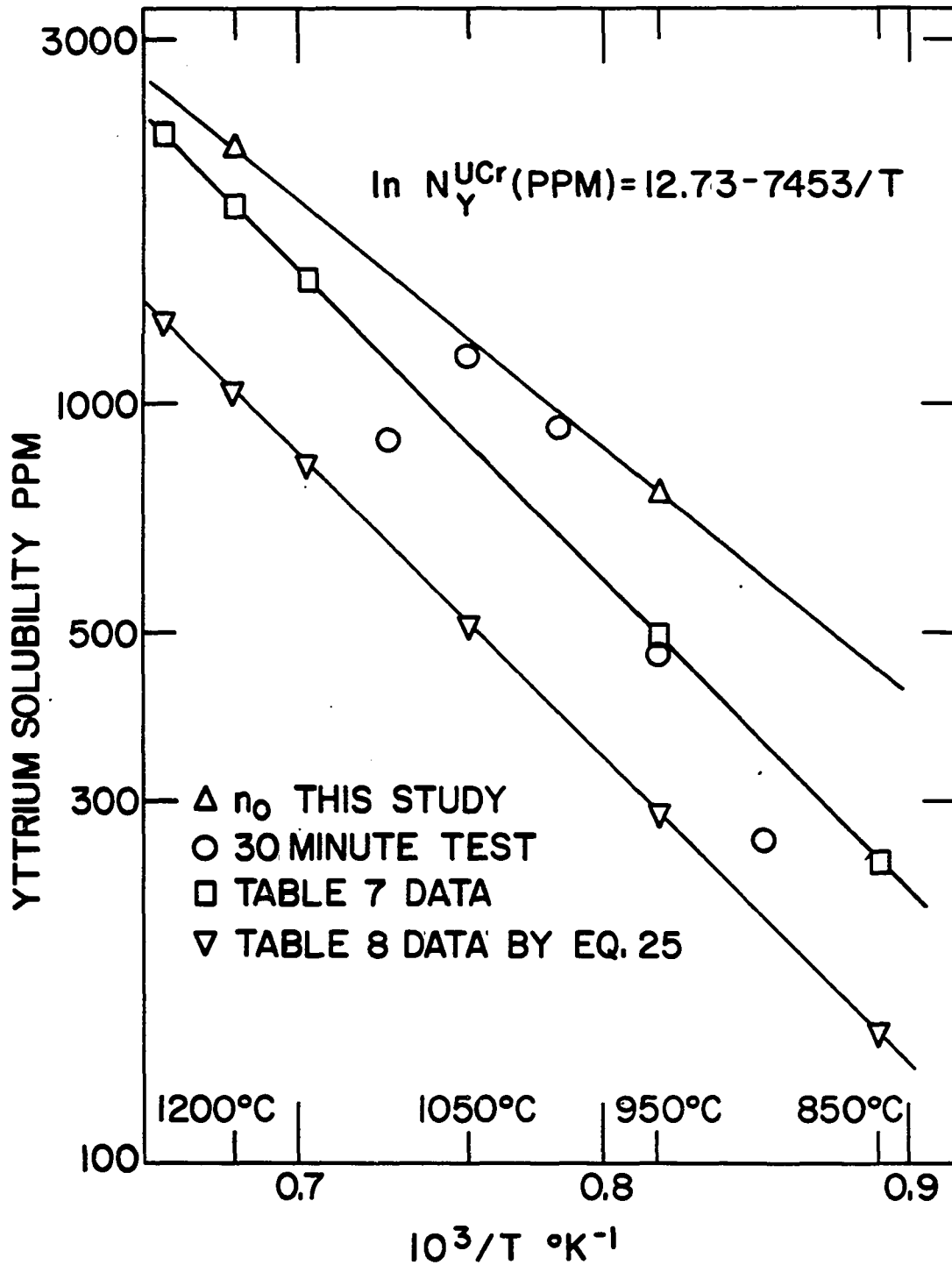


Figure 35. Temperature dependence of yttrium solubility in uranium-chromium eutectic as determined experimentally and predicted theoretically

This can be seen from Figure 33 where for $t = 33$ minutes, $n_t = 698$ ppm at 950°C compared to 466 ppm obtained for the 30 minute test listed in Table 20. The values at 900 and 1100°C should also be correspondingly higher. The α 's determined at 900 and 950°C fall quite close to the best straight line obtained for $\alpha = \alpha_0 \text{ Exp} [-\Delta E/RT]$. Second, the value for $\Delta E = 17.3$ Kcal/mole obtained from the dashed line through the two points shown in Figure 36 agrees more closely with the partial molar enthalpy determined from the solubility curve for yttrium in U-Cr (Table 22).

Table 20. Calculation of dissolution constant α for yttrium in U-Cr from Equation 49

Temperature		$\frac{1000}{T}$	n_t	n_0^a	Corrected time	Dissolution constant ^b
$^\circ\text{C}$	$^\circ\text{K}$	$^\circ\text{K}^{-1}$	ppm	ppm	min	cm/min
900	1173	0.8525	226	586	33.0	0.00333 (0.01019) ^c
950	1223	0.8177	466 (698) ^d	760 760	33.0 33.0	0.00523 (0.01381) ^e
1000	1273	0.7856	930	965	33.0	0.01827 (0.01827)
1050	1323	0.7559	1144	1204	33.0	0.01652 (0.02367)
1100	1373	0.7283	890	1478	33.0	0.00509 (0.03010)

^aExtrapolated from Figure 35: $\ln N_Y^{\text{UCr}} \text{ (ppm)} = 12.73 - 7453/T$.

^bCalculated from solubility test series with $S/V = 5.50\text{cm}^{-1}$.

^cValues in parentheses correspond to dashed line in Figure 36: $\alpha = 17.29 \text{ Exp} [-17,300/RT]$. Solid line gives $\alpha = 4.54 \text{ Exp} [-33,000/RT]$.

^dValue obtained from Figure 33 at $t = 33.0$ minutes.

^eCalculated using $n_t = 698$ ppm.

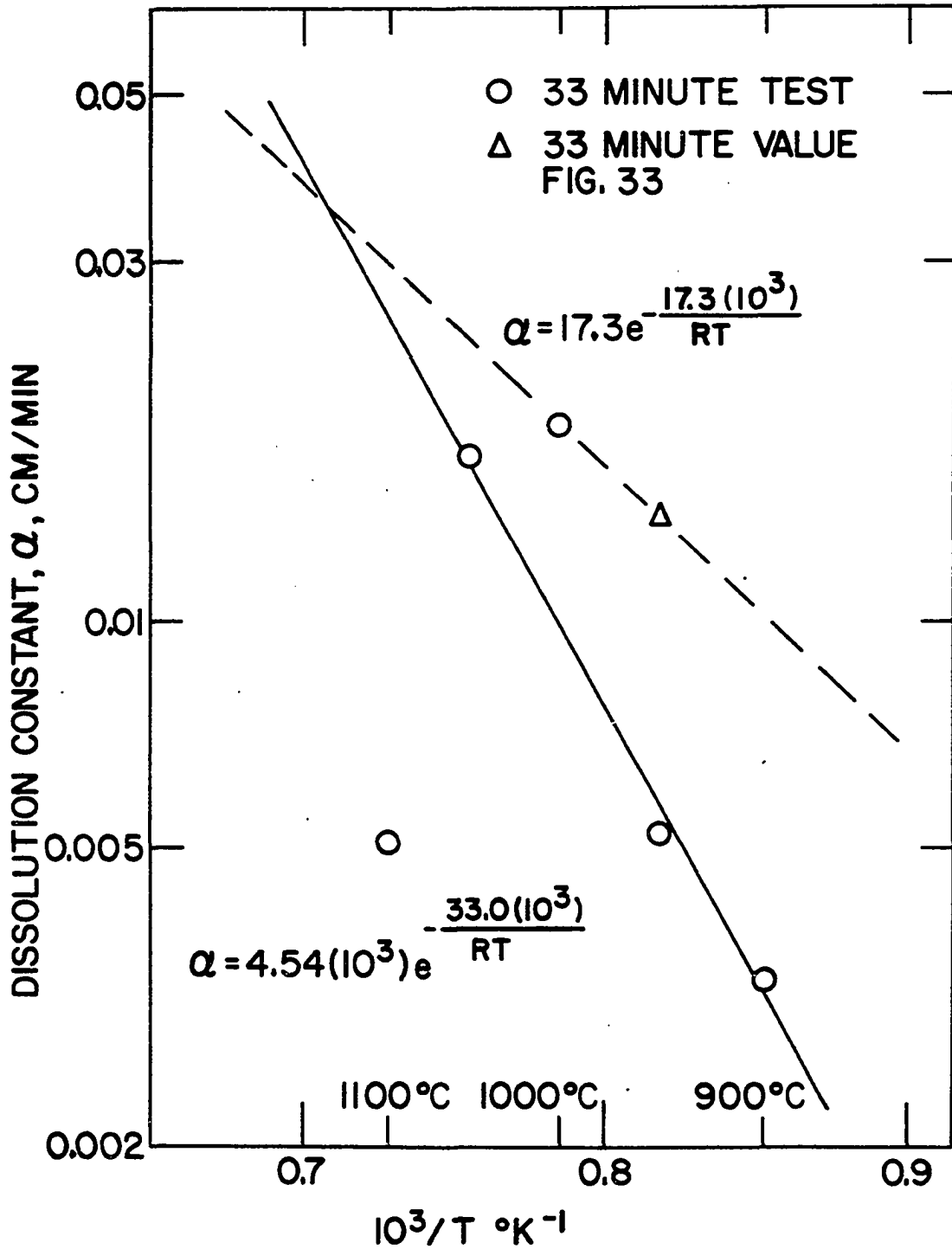


Figure 36. Dissolution-rate constant variance with temperature as determined in this study

The activation energies obtained from Appendix B and Equation 52 can be compared with one another as well as with $\overline{\Delta H}$ values obtained from the solubility equations presented earlier. Comparison of interfacial surface tensions calculated from $\overline{\Delta H}$ and Equation 68 can also be made with those calculated by Good's method (Equation 66). These comparisons are best portrayed in tabular form in Tables 21 and 22.

Table 21. Estimated surface tensions and surface free energies at 950°C

System	Surface tension γ_{LV}^a ergs/cm ²	Surface free energy F_γ^b Kcal/mole	F_γ^c 0.15 ΔH_V Kcal/mole
Y	831.3	13.8	15.0
U	1482.8	18.2	18.0
UCr	1482.3 ^d	17.3	17.2
UCrFe	1482.0 ^d	17.2	17.1

^aCalculated by the approximate method of Grosse (77, 78) using a general relationship relating the critical temperature and surface tension.

^bCalculated from $F_\gamma = 2.20 (V_m)^{2/3} \gamma$ cal/mole (78, 79) where V_m is the molar volume at the temperature of concern.

^cCalculated using $F_\gamma \approx 0.15 \Delta H_V$ (79) at 950°C for cubic or tetragonal metals.

^dValues for the eutectic alloys were calculated assuming the surface tensions vary linearly with the mole fractions of the constituents: $\gamma_{Cr} = 1480.0$ ergs/cm² and $\gamma_{Fe} = 1531.8$ ergs/cm².

The surface tensions and surface free energies listed in Table 21 were all calculated for the liquid state at 950°C. The value for yttrium

Table 22. Comparison of activation energies and calculated surface tensions

System	Diffusion activation energy ^a Q Kcal/mole	Dissolution activation energy ^b ΔE^b Kcal/mole	Partial molar enthalpy, $\Delta \bar{H}^c$ Kcal/mole	Interfacial tension $\gamma_{SL}^d \approx \frac{\Delta \bar{H}}{V/d}$ ergs/cm ²	Interfacial tension γ_{SL} Eq. 66 ² ergs/cm ²
Y in U	7.16	--	17.1 (Table 6) 18.7 (Table 4)	1,236 1,351	107.0
Y in UCr	6.36	33.0 (17.3)	14.8 (This Study) 18.2 (Table 8) 18.8 (Table 7)	1,067 1,316 1,351	110.4
Y in UCrFe	6.14	--	18.7 (Table 8)	1,349	111.4

^aActivation energy determined by absolute-rate method in Appendix B.

^bActivation energy determined from slope of curves in Figure 36; parentheses' value is for dashed curve.

^cSlope of solubility curves is equal to $-\Delta \bar{H}/R$ (81).

^dInterfacial tensions calculated from Equation 68 (80) using V_m at 950°C and $d = 3.558$ angstroms for yttrium.

(831.3 ergs/cm²) is lower than normal for solids and is undoubtedly incorrect as predicted by Grosse's method (77, 78). This method is, in fact, not valid for calculating solid-vapor surface tensions, γ_{SV}^I , which must be determined experimentally, because of the discontinuity in the surface tension at the melting point. The surface free energies in column 3 are calculated from these values and compared with those obtained from the heats of vaporization at 950°C. These compare favorably except for yttrium. The values in column 2 of Table 21 were used to calculate the interfacial

^IA. V. Grosse, Philadelphia, Penn. Estimating surface tensions. Private communication. 1968.

surface tensions, γ_{SL} , by Equation 66 for the systems in Table 22 (last column only). The values predicted by Equation 66 are low as compared to the values obtained in column 5 from the partial molar enthalpy, $\Delta\bar{H}$. In general, interfacial surface tensions, γ_{SL} , range up to 400 ergs/cm² for liquid metal--solid metal systems¹; therefore, the predictions of γ_{SL} by the method of Weeks are probably too high.

Whenever $\gamma_{GB} \geq 2\gamma_{SL}$, grain-boundary penetration would be expected. The values of γ_{GB} are not determined experimentally but must be calculated from the measured dihedral angle, θ , and γ_{SL} via Equation 64b. The dihedral angle measured on a number of the solubility capsules was always 120° or more. With $\theta = 120^\circ$ and the two values for γ_{SL} in Table 22 for yttrium in U-Cr-Fe, $\gamma_{GB} = 111.4$ ergs/cm² or $\gamma_{GB} = 1349$ ergs/cm² from Equation 64b. The latter value of γ_{GB} is higher than normal for metals and would possibly allow intergranular attack. Since no grain-boundary penetration was noted in any of the tests with U-Cr or U-Cr-Fe, the true γ_{GB} for yttrium must be low.

The value for γ_{SL} is quite temperature dependent decreasing with rising temperature as evidenced by the values reported in the literature for various liquid-metal systems. For example, the Cu-Bi system at 400°C has a measured $\gamma_{SL} = 1250$ ergs/cm² (80), while at 900°C $\gamma_{SL} = 100$ ergs/cm² (74). Based on data of other systems at high temperatures, it would seem that Good's expression (Equation 66) is more in line with actual experimental values than that by Weeks (Equation 68). However, because experimental data on surface tensions for liquid metals are so lacking in the

¹J. D. Verhoeven, Ames Laboratory, Ames, Iowa. Interfacial surface tensions. Private communication. 1968

literature, the author will not praise or condemn any one equation, but only present both results.

Referring again to Table 22, values for the activation energies and partial molar enthalpy can be discussed. The diffusion activation energies are low when compared to the values in columns 3 and 4, but this does not mean they are wrong. They should agree only if it is assumed that the energy values are a measure of the barrier to an yttrium atom passing from the solid phase into the bulk of the liquid metal. While this apparently holds for the over-all dissolution process (the parentheses' value is believed to be the more accurate), the diffusion itself--from a theoretical standpoint--requires less energy. This has a bearing on whether the dissolution process is solution- or diffusion-controlled as discussed shortly.

The partial molar enthalpies calculated from the slope of the theoretical and experimental solubility curves compare favorably. Although Equation 25 gives values too low for U-Cr and U-Cr-Fe, the slope or temperature coefficient of solubility is predicted with a fair degree of accuracy.

If the over-all process of dissolution is controlled by diffusion through the stagnant boundary layer, then α is related to D/δ by Equation 51. It is generally agreed by many liquid-metal corrosion investigators that δ is independent of temperature (62, 63). Trying this criterion with the values for D calculated in Appendix B and α from Table 20 for yttrium in U-Cr yields the following equation:

$$\delta = D/\alpha = 60(D_0/\alpha_0)\text{Exp}[(17.3 - 6.4)/RT] = 1.03(10^{-3})\text{Exp}[10.9/RT]. \quad (76)$$

At 950°C, δ would equal 0.093 cm (0.037 inches) or about what is to be expected for the boundary layer (if such exists) as compared to other liquid-metal systems (63). Clearly δ in Equation 76 is not independent of temperature. This fact, coupled with the low energy of activation for the diffusion process, suggests that the dissolution process is solution-controlled and the stagnant boundary layer is non-existent because diffusion occurs much faster than solution. This may seem somewhat surprising because the viscosities involved are some of the highest known for liquid metals.

One might tend to believe a diffusion process would be retarded because of the relationship between μ and D . Indeed, the larger the viscosity, the smaller the diffusion coefficient. However, in this case, the large atomic size differences and small differences in electro-negativities result in a slow solution process. This is also seen from the solubility test results where it was seen to take nearly two hours at 950°C to reach the equilibrium solubility value (Figure 33) as compared to liquid mercury in contact with iron which reaches saturation in just a few seconds (62). (See Figure 8).

CONCLUSIONS

The investigation presented in this paper has consisted of four main studies: 1. preliminary determination of the ternary eutectic point in the uranium-chromium-iron system; 2. solubility tests to determine the dissolution-rate constant, α , for yttrium in the uranium-chromium eutectic; 3. liquid-metal corrosion tests with the uranium-chromium eutectic in yttrium; and 4. tests with iron additions to the uranium-chromium eutectic to determine its effects on the corrosion phenomenon.

A preliminary investigation to determine the ternary eutectic point in the uranium-chromium-iron system has shown that the eutectic exists close to the composition of 95.0 wt.% U-2.5 wt.% Cr-2.5 wt.% Fe and melts at 765°C. This is contrary to published results by Saller et al. (51) who obtained U.S. Patent 2,735,761 (95) and U.K. Patent 816,603 (96) on the supposed ternary composition of 94.0 wt.% U-5.0 wt.% Cr-1.0 wt.% Fe melting at 760°C. Differential thermal analyses conducted as part of this investigation on several alloy samples at the latter composition showed an incongruous alloy with approximate solidus and liquidus temperatures of 765 and 834°C, respectively. These findings are also corroborated by an earlier test conducted at the Ames Laboratory (97).

Results of this study showed the dissolution constant for yttrium in U-Cr eutectic equal to 0.0138 cm/minute at 950°C corresponding approximately to the equation $\alpha = 17.29 \text{ Exp } [-17,300/RT]$ cm/min for temperatures from 900 to 1200°C. The diffusion coefficients calculated in Appendix B for the same system are given by $D = 29.58 (10^{-5}) \text{ Exp } [-6,355/RT]$ cm²/sec. The activation energy for dissolution is nearly three times greater than

the activation energy for diffusion; hence, the over-all dissolution process is solution-controlled.

The dissolution activation energy compares well with the partial molar enthalpies, $\bar{\Delta H}$, obtained experimentally and by theoretical means (Table 22). However, comparison of the interfacial tension, γ_{SL} , from $\bar{\Delta H}$ by an approximate method of Weeks (80) shows poor comparison with γ_{SL} calculated by Good's Equation [Equation 66, (74)]. Good's correlation appears to be more accurate since Equation 66 predicts values in line with those determined experimentally for liquid-metal systems. The interfacial surface tensions should only show agreement if it is assumed to be a measure of the activation energy barrier for an atom to pass from the bulk of the solid metal through the interface into solution.

The experimental equilibrium solubility of yttrium in U-Cr eutectic was found to be given by $\ln N_Y^{UCr} \text{ (ppm)} = 12.73 - 7453/T^{\circ K}$ over the 900 to 1200°C temperature range. The dissolution of yttrium by U-Cr eutectic at 950°C was found to agree to an equation of the form $n_t \text{ (ppm)} = 760\{1 - \text{Exp}[-0.0138 (S/V)t]\}$ with t in minutes and S/V in cm^{-1} . This corresponds to a corrosion rate of 1.66 $\text{mg}/\text{cm}^2/\text{hour}$.

The reduced concentration-time curve (Figure 34) can be used to calculate complete dissolution versus time data for the yttrium in U-Cr system at other temperatures provided the saturation solubility and the time to reach saturation are known. For a given system, the reduced concentrations and times will conform to the curve shown. Most of the liquid-metal corrosion tests were conducted as nominally static isothermal tests, although a true static, isothermal state was not achieved. Temperature gradients of from 1 to 3°C along the capsule lengths generated small

convective currents which were further enhanced to a slight extent by concentration differences. This effect manifested itself as increased corrosion attack near the meniscus in all longer-term static tests. Under ideal conditions the maximum penetration depth for the static capsules with an approximate S/V ratio = 2.7 cm^{-1} should have been about 0.0001 inch at 950°C . That is, the ideal situation would conform to Equations 40 or 49 in which the liquid-metal would reach saturation solubility in a short period of time (a few hours) and thereafter suffer no further corrosion attack. In reality, however, practical systems do not involve ideal situations, and the results of the corrosion tests of this investigation illustrate vividly what would happen under temperature gradients in the core of the liquid-metal fueled reactor of the type proposed by Los Alamos Scientific Laboratory. If a loop system were involved with a temperature differential of only 50°C the corrosion rate at a mean loop temperature of 950°C would be approximately $2.6 \text{ mg/cm}^2/\text{hr}$ which would eventually cause plugging.

The corrosion tests of this investigation showed that yttrium alone is not a worthy long-time containment metal for U-Cr eutectic at 950°C and above. Although most of the capsule tests in this investigation suffered increased attack because of the silicon impurity unintentionally introduced, yttrium capsules without the impurity would have still undergone enough dissolution attack to disqualify yttrium for use in a liquid-metal fueled reactor. These results are contrary to those found in the literature (7) where it is stated, "It can be concluded that the interaction, if any, between these two phases [yttrium and U-Cr eutectic] is insignificant."

Iron additions to the base U-Cr eutectic not only lower the liquidus and solidus temperatures but also increase the amount of corrosion attack.

While alloys with iron additions up to about 1.0 wt.% were only slightly more corrosive, the larger additions (2.5 to 10.0 wt.% iron) greatly increased the amount of penetration. Chromium plays an important role in limiting the amount of corrosion since a test with U-11.0 wt.% Fe eutectic in yttrium failed in less than 60 hours at 950°C whereas two UCr-10.0 wt.% Fe test samples did not fail after 300 hours. However, the addition of chromium to uranium increases the corrosion expected as does the addition of iron. The U-Cr-Fe eutectic existing around U-2.5 wt.% Cr-2.5 wt.% Fe is slightly more corrosive in nature than the U-5 wt.% Cr Eutectic alone with an equilibrium solubility of approximately 1000-1100 ppm yttrium as compared to 760 ppm yttrium for the U-Cr eutectic. No evidence of intergranular penetration or intermetallic compound formation was found in either series of tests. This agrees with the theoretical predictions.

The inexpensive and nominally static, isothermal capsule tests employed in this investigation were a more severe test of yttrium for containment of molten U-Cr and U-Cr-Fe alloys than an ideal isothermal, static or dynamic system would have been. Furthermore, they made it possible to predict what should happen with a more expensive circulating loop operating under a thermal gradient.

RECOMMENDATIONS FOR FURTHER STUDY

Several items which came to light during the course of this investigation are worthy of further study. The following are listed.

1. The investigation of the ternary eutectic in the uranium-chromium-iron system was only a preliminary study. Although the ternary eutectic was found to lie close to the line AB in Figure 23, the exact composition could be determined by one or both of the following methods: a) a zone-melting technique accurate to 0.1 wt.% or better as explained by Yue and Clark (112) for complex metal systems; and b) a differential thermal analysis method using various alloy compositions suitably located on isopleths of a ternary phase diagram as described by Rhines (113). Ricci (109) also gives a rigorous treatment of ternary systems.

2. Determination of the dissolution-rate constant should be made for the U-Cr and U-Cr-Fe eutectics over a range of temperatures. The best procedure would probably be the radioactive tracer technique described earlier. The uncertainty involved in the analytical procedure is considerably greater. Tantalum capsules should be used because of the graphite interaction which was noted in the text. An attempt should be made to obtain uranium free of yttrium impurity in order to construct the initial portion of the concentration-time curves. Although the dissolution of yttrium in U-Cr eutectic appears to be solution-controlled, determination of accurate values of α with temperature will enable one to compare ΔE with Q , the activation energies for dissolution and diffusion, respectively, and thereby confirm which step is rate-controlling.

3. This investigation showed that yttrium definitely suffered

dissolution attack with the U-Cr eutectic and the UCr-Fe alloys. In the 360° rotary tests the amount of corrosion attack was considerably less because the fuel was agitated and increased attack was prevented in certain areas. The presence of silicon impurity greatly enhanced the corrosion process. It would, therefore, be interesting to check for corrosion without silicon present under isothermal, dynamic conditions and under temperature gradient, dynamic conditions. The construction and expense of a forced-circulation test loop can not be justified because plugging would undoubtedly occur quite rapidly. However, an indication of plugging could be determined by using a simple rocking apparatus under a temperature differential (50°C or more). Brasunas (114) and others have described such equipment.

4. Although pure tantalum is a rather poor containment metal for molten uranium and plutonium alloys, remarkable results have been achieved at the Los Alamos Scientific Laboratory using tantalum coated with a carbide layer (115, 116). Some success was also demonstrated in several early tests at the Ames Laboratory with the uranium-eutectic alloys (97). A corrosion investigation using the Ta₂C layer inside tantalum capsules should be conducted with the U-Cr and U-Cr-Fe eutectics to determine the effectiveness of the carbide coating.

NOMENCLATURE

a	chemical activity
a_{AB}	parameter defined by Equation 26
A	solid-liquid interface area, cm^2
ΔC_p	change in heat capacity at constant pressure, $\text{cal/mole}^\circ\text{K}$
d	inside diameter of loop tubing in cm, Equation 71
d_G	Goldschmidt atomic diameter, \AA , 12 fold coordination
D	Diffusion coefficient, cm^2/sec
E_B	binding energy, cal/mole
ΔE	activation energy for dissolution, cal/mole
ΔE^V	energy of vaporization, cal/mole
f	factor defined by Equation 99: fraction of the total free energy of activation due to the bond breaking or kinetic component
F	free energy, cal/mole
F_γ	surface free energy, cal/mole
ΔF	free energy change for process noted by subscript or superscript
ΔF^*	free energy of activation, cal/mole , Equation 101
ΔH	enthalpy change for process noted by subscript or superscript
ΔH^*	enthalpy of activation, cal/mole
k	Mott number, Equation 6, or Henry's Law constant, Equation 7
k'	parabolic rate constant, cm^2/sec , Equation 100
k_s	proportionality solution-rate constant
K	thermodynamic equilibrium constant
m	mass of solute in solution, g
M	molecular weight, g/mole
n	number of metal-metal bonds, Equation 6

n	concentration of the solute in solution, atoms/cc
n_0 or S^0	saturation concentration of the solute in solution, atoms/cc
n_t	concentration of solute at time t , atoms/cc, ppm, etc.
n_x	fraction of saturation concentration, atoms/cc, ppm, etc.
n'	concentration of solute atoms in diffusion layer, atoms/cc
N	mole fraction of solute in solution
N	number of atoms
Q	activation energy for diffusion, cal/mole
r	radius of diffusing atom, cm, Equation 111
R	corrosion rate, $\text{g/cm}^2\text{-sec}$
S	surface area at interface, cm^2
ΔS	entropy change for process noted by subscript or superscript
ΔS^*	entropy of activation, cal/mole
t	time
t_x	time to reach concentration n_x , minutes
T	absolute temperature, $^{\circ}\text{K}$
ΔT	temperature differential, $^{\circ}\text{C}$
T^*	reduced temperature, dimensionless
U-Cr	uranium-chromium eutectic at 95.0 wt.% U
U-Cr-Fe	uranium-chromium-iron eutectic of Saller <u>et al.</u> (51): 94 wt.% U-5 wt.% Cr-1 wt.% Fe
v	flow velocity, cm/sec
\bar{v}	frequency factor, Equation 33
V	volume of solvent, cc
V	molar volume, cc/mole; also V_m
V_m^*	reduced molar volume, dimensionless

ΔW	weight change, g
x	thickness of solid-metal layer removed by dissolution; or thickness of intermetallic phase
X	electronegativity, eV
Y	factor defined by Equation 98

Greek letters

α	dissolution-rate constant, cm/min
α_0	dissolution constant of integration, cm/min, Equation 52
γ	activity coefficient
γ	surface tension, ergs/cm ² : γ_{SV} --solid with its vapor; γ_{LV} --liquid with its vapor; γ_{GB} --grain boundary surface tension
γ_{SL}	interfacial surface tension between liquid and solid metals, ergs/cm ²
δ	Hildebrand solubility parameter, (cal/cc) ^{1/2}
δ	stagnant boundary layer thickness, cm
δ'	effective solubility parameter, (cal/cc) ^{1/2} , Equation 96
δ'	factor defined by Equation 100
ϵ	energy parameter, Equation 107
θ	dihedral angle, degrees
μ	viscosity, poise (g/cm-sec)
μ^*	reduced viscosity, dimensionless
ν	kinematic viscosity, cm ² /sec
ρ	density, g/cc
φ	volume fraction
φ	factor defined in Equation 67

Subscripts

A	quantity referring to solute
AA	interaction between solute atoms
AB	interaction between solvent and solute atoms
B	quantity referring to solvent
BB	interaction between solvent atoms
m	melting
mix	mixing
v	vaporization

Superscripts

°	standard state or equilibrium value
-	partial molar quantity
xs	excess quantity
v	vaporization

Constants

Å	Angstroms, 10^{-8} cm
h	Planck's constant, $6.625 (10^{-27})$ ergs/°K
k	Boltzmann constant, $1.3805 (10^{-16})$ ergs/°K
mil	0.001 inch
N_o	Avogadro's number, $6.0228 (10^{23})$ mole ⁻¹
R	gas constant, 1.9872 cal/mole°K or $8.3143 (10^7)$ ergs/mole°K

BIBLIOGRAPHY

1. Kelman, L. R., Wilkinson, W. D., and Yaggee, F. R. U.S. Atomic Energy Commission Report ANL-4417 [Argonne National Lab., Ill.]. 1950.
2. Haefling, J. F. and Daane, A. H. Trans. Met. Soc. AIME 215: 336. 1958.
3. Rosa, R. and Kantrowitz, A. Int. Sci. Technol. 33: 80. 1964.
4. Thamer, B. J. At. Energy Rev. 1, No. 2: 3. 1963.
5. Thamer, B. J. Corrosion tests with molten plutonium fuels. In Corrosion of reactor materials. Vol. 2. Pp. 285-318. Vienna, Austria, International Atomic Energy Agency. 1962.
6. Cash, R. J., Fisher, R. W., and Core, M. R. U.S. Atomic Energy Commission Report IS-888 [Ames Lab., Ames, Iowa]. 1964.
7. Fisher, R. W. and Fullhart, C. B. Second U.N. International Conference on the Peaceful Uses of Atomic Energy Proceedings 7: 216. 1958.
8. Hansen, M. and Anderko, K. Constitution of binary alloys. New York, N.Y., McGraw-Hill Book Co., Inc. 1958.
9. Elliott, R. P. Constitution of binary alloys, first supplement. New York, N.Y., McGraw-Hill Book Co., Inc. 1965.
10. Cash, R. J. and Fisher, R. W. U.S. Atomic Energy Commission Report IS-768 [Ames Lab., Ames, Iowa]. 1965.
11. Hildebrand, J. H. and Scott, R. L. The solubility of nonelectrolytes. 3rd ed. New York, N.Y., Reinhold Publishing Corp. 1950.
12. Niwa, K. and Shimoji, M. Structure of liquid solutions. In The physical chemistry of metallic solutions and intermetallic compounds. Vol. 1. Pp. 165-179. New York, N.Y., Chemical Publishing Co., Inc. 1960.
13. Hultgren, R. and Orr, R. L. Rev. Int. Hautes Tempér. et Réfract. 4: 123. 1967.
14. Hildebrand, J. H. and Scott, R. L. Regular solutions. Englewood Cliffs, N.J., Prentice-Hall, Inc. 1962.
15. Hildebrand, J. H. An introduction to molecular kinetic theory. New York, N.Y., Reinhold Publishing Corp. 1963.
16. Eyring, H. and Ree, T. Proc. Nat. Acad. Sci. 47: 526. 1961.
17. Frenkel, J. Trans. Faraday Soc. 33, Pt. 1: 58. 1937.

18. Bernal, J. D. *Trans. Faraday Soc.* 33, Pt. 1: 27. 1937.
19. Hardy, H. K. *Acta Met.* 1: 202. 1953.
20. Gingrich, N. S. *Rev. Mod. Phys.* 15: 90. 1943.
21. Darken, L. S. and Gurry, R. W. *Physical chemistry of metals.* New York, N.Y., McGraw-Hill Book Co., Inc. 1953.
22. Frost, B. R. T. *Progr. Metal Phys.* 5: 96. 1954.
23. Sauerwald, F., Brand, P., and Menz, W. U.K. Atomic Energy Authority Report AERE-Trans-1060 [Atomic Energy Research Establishment, Harwell, England]. 1966.
24. Grove, G. R., Jones, L. V., and Eichelberger, J. F. U.S. Atomic Energy Commission Report MLM-1139 [Mound Lab., Miamisburg, Ohio]. 1962.
25. Grove, G. R., Jones, L. V., and Eichelberger, J. F. U.S. Atomic Energy Commission Report MLM-1140 [Mound Lab., Miamisburg, Ohio]. 1962.
26. Annual summary research report for the Ames Laboratory: July 1, 1966 to June 30, 1967. U.S. Atomic Energy Commission Report IS-1600 [Ames Lab., Ames, Iowa]. 1967.
27. Sheinhartz, I., Moyer, K., and Zambrow, J. L. U.S. Atomic Energy Commission Report SCNC-293 [Sylvania-Corning Nuclear Corp., Bayside, N.Y.]. 1959.
28. Hultgren, R., Orr, R. L., and Kelley, K. K. Supplement to selected values of thermodynamic properties of metals and alloys. Berkeley, Calif., Lawrence Radiation Lab. 1968.
29. Gibson, J. A. and Harvey, G. S. U.S. Atomic Energy Commission Report AFML-TR-65-430 [Air Force Materials Lab., Wright-Patterson Air Force Base, Ohio]. 1966.
30. Stuli, D. R. and Sinke, G. C. *Advan. Chem. Ser.* 18. 1956.
31. Oriani, R. A. *J. Phys. Chem. Solids* 2: 327. 1957.
32. Sundquist, B. E. *Trans. Met. Soc. AIME* 236: 1111. 1966.
33. Pratt, J. N. *Rev. Int. Hautes Temp. et Réfract.* 4: 97. 1967.
34. Anderson, P. D. U.S. Atomic Energy Commission Report UCRL-11821 [Lawrence Radiation Lab., Berkeley, Calif.]. 1966.
35. Oriani, R. A. and Alcock, C. B. *Trans. Met. Soc. AIME* 224: 1104. 1962.

36. Strauss, S. W., White, J. L., and Brown, B. F. U.S. Atomic Energy Commission Report NRL-4961 [Naval Research Lab., Washington, D.C.]. 1957.
37. Gschneidner, K. A., Jr. U.S. Atomic Energy Commission Report IS-1757 [Ames Lab., Ames, Iowa]. 1968.
38. Moore, W. J. Physical chemistry. 3rd ed. Englewood Cliffs, N.J., Prentice Hall, Inc. 1962.
39. Mott, B. W. Phil. Mag. 8: 259. 1957.
40. Shimoji, M. Immiscibility of liquid metallic solutions. In St. Pierre, G. R., ed. Physical chemistry of process metallurgy. Pt. 1. Pp. 421-427. New York, N.Y., Interscience Publishers, Inc. 1961.
41. Isserow, S. In Annual progress report to the AEC research division for the period July 1, 1956 to July 1, 1957. Pp. 86-110. U.S. Atomic Energy Commission Report NMI-1182 [Nuclear Metals, Inc., Cambridge, Mass.]. 1957.
42. Rough, F. A. and Bauer, A. A. U.S. Atomic Energy Commission Report BMI-1300 [Battelle Memorial Institute, Columbus, Ohio]. 1958.
43. Lundin, C. E. Rare-earth metal phase diagrams. In Spedding, F. H. and Daane, A. H., eds. The rare earths. Pp. 224-385. New York, N.Y., John Wiley and Sons, Inc. 1961.
44. Pasternak, A. D. U.S. Atomic Energy Commission Report UCRL-16108 [Lawrence Radiation Lab., Berkeley, Calif.]. 1966.
45. Pasternak, A. D. U.S. Atomic Energy Commission Report UCID-15190 [Lawrence Radiation Lab., Livermore, Calif.]. 1967.
46. Strauss, S. W., White, J. L., and Brown, B. F. Acta Met. 6: 604. 1958.
47. Strauss, S. W. Acta Met. 10: 171. 1962.
48. White J. L. U.S. Atomic Energy Commission Report NRL-5555 [Naval Research Lab., Washington, D.C.]. 1960.
49. Lewis, G. N. and Randall, M. Thermodynamics. 2nd ed. New York, N.Y., McGraw-Hill Book Co., Inc. 1961.
50. Saller, H. A., Rough, F. A., and Bauer, A. A. U. S. Atomic Energy Commission Report BMI-869 [Battelle Memorial Institute, Columbus, Ohio]. 1953.

51. Saller, H. A., Rough, F. A., and Bauer, A. A. U.S. Atomic Energy Commission Report BMI-868 [Battelle Memorial Institute, Columbus, Ohio]. 1953.
52. Voigt, A. F. [First] U.N. International Conference on the Peaceful Uses of Atomic Energy Proceedings 9: 591-595. 1956.
53. Technical progress report for the period January 1953 through March 1953. U.S. Atomic Energy Commission Report MIT-1111 [Massachusetts Institute of Technology, Cambridge]. 1953.
54. McKee, J. M., Jr. U.S. Atomic Energy Commission Report AECD-4059 [Nuclear Development Associates, Inc., White Plains, N.Y.]. 1953.
55. Brasunas, A. deS. U.S. Atomic Energy Commission Report ORNL-1647 [Oak Ridge National Lab., Tenn.]. 1954.
56. Brasunas, A. deS. Corrosion 9, No. 5: 78. 1953.
57. Manly, W. D. U.S. Atomic Energy Commission Report ORNL-2055 [Oak Ridge National Lab., Tenn.]. 1956.
58. Miller, E. C. Corrosion of materials by liquid metals. In Lyon, R. N., ed. Liquid-metals handbook. Pp. 144-183. U.S. Atomic Energy Commission Report NAVEXOS P-733 (Rev.) [Office of Naval Research, Washington, D. C.]. 1952.
59. Epstein, L. F. [First] U.N. International Conference on the Peaceful Uses of Atomic Energy Proceedings 9: 311-317. 1956.
60. Weeks, J. R. and Klamut, C. J. Liquid metal corrosion mechanisms. In Corrosion of reactor materials. Vol. 1. Pp. 105-132. Vienna, Austria, International Atomic Energy Agency. 1962.
61. Moelwyn-Hughes, E. A. The kinetics of reactions in solution. 2nd ed. Oxford, England, Oxford University Press. 1947.
62. Epstein, L. F. Chem. Eng. Progr. Symp. Ser. 53, No. 20: 67. 1957.
63. Taylor, J. W. and Ward, A. G. U.K. Atomic Energy Authority Report AERE-M/R-2295 [Atomic Energy Research Establishment, Harwell, England]. 1957.
64. Ward, A. G. and Taylor, J. W. U.K. Atomic Energy Authority Report AERE-M/R-2113 [Atomic Energy Research Establishment, Harwell, England]. 1957.
65. Jackson, J. K. and Grace, R. E. Rates of solution of rotating zinc cylinders in liquid bismuth. In St. Pierre, G. R., ed. Physical chemistry of process metallurgy. Pt. 1. Pp. 633-644. New York, N.Y., Interscience Publishers, Inc. 1961.

66. Levich, V. G. Physicochemical hydrodynamics. 2nd ed. Englewood Cliffs, N.J., Prentice Hall, Inc. 1962.
67. Pasternak, A. D. and Olander, D. R. A.I.Ch.E. J. 13: 1052. 1967.
68. Thomaes, G. and Van Itterbeek, J. Mol. Phys. 2: 372. 1959.
69. Chapman, T. W. A.I.Ch.E. J. 12: 395. 1966.
70. Grosse, A. V. J. Inorg. Nucl. Chem. 23: 333. 1961.
71. Eldred, V. W. U.K. Atomic Energy Authority Report AERE-X/R-1806 [Atomic Energy Research Establishment, Harwell, England]. 1955.
72. Pauling, L. The nature of the chemical bond. 3rd ed. Ithaca, N.Y., Cornell University Press. 1960.
73. Weeks, J. R. and Gurinsky, D. H. Solid metal-liquid metal reactions in bismuth and sodium. In Liquid metals and solidification. Pp. 106-161. Cleveland, Ohio, American Society for Metals. 1958.
74. Good, R. J. Surface energy phenomena and corrosion. In Proceedings of the NASA-AEC liquid-metals corrosion meeting. Pp. 107-125. U.S. Atomic Energy Commission Report NASA-SP-41 [National Aeronautics and Space Administration, Washington, D.C.]. 1964.
75. Smith, C. S. Trans. Met. Soc. AIME 175: 15. 1948.
76. Kirkbride, L. D., Dunning, D. N., Ferguson, W. E., and Perkins, R. H. U.S. Atomic Energy Commission Report LADC-6026 [Los Alamos Scientific Lab., N. Mex.]. 1964.
77. Grosse, A. V. J. Inorg. Nucl. Chem. 22: 23. 1961.
78. Grosse, A. V. J. Inorg. Nucl. Chem. 24: 147. 1962.
79. Grosse, A. V. J. Inorg. Nucl. Chem. 26: 1349. 1964.
80. Weeks, J. R. Relation between solubility and interfacial free energy. In Progress report: nuclear engineering department, May 1 to August 31, 1963. Pp. 82-83. U.S. Atomic Energy Commission Report BNL-823 [Brookhaven National Lab., Upton, N.Y.]. 1963.
81. Kleppa, O. J. and Weil, J. A. J. Amer. Chem. Soc. 73: 4848. 1951.
82. Barrett, L. K. U.S. Atomic Energy Commission Report ORNL-TM-1224 [Oak Ridge National Lab., Tenn.]. 1964.
83. Maneri, C. C. and Milford, F. J. U.S. Atomic Energy Commission Report ARL-48 [Aeronautical Research Lab., Wright-Patterson Air Force Base, Ohio]. 1961.

84. McLean, D. Grain boundaries in metals. London, England, Oxford University Press. 1957.
85. DiStefano, J. R. and Hoffman, E. E. U.S. Atomic Energy Commission Report ORNL-3424 [Oak Ridge National Lab., Tenn.]. 1963.
86. Quarterly status report on advanced reactor technology (ART) for period ending October 31, 1965. U.S. Atomic Energy Commission Report LA-3431-MS [Los Alamos Scientific Lab., N. Mex.]. 1965.
87. Quarterly summary research report in metallurgy: October--December, 1954. U.S. Atomic Energy Commission Report ISC-575 [Ames Lab., Ames, Iowa]. 1955.
88. Quarterly summary research report in metallurgy: January--March, 1955. U.S. Atomic Energy Commission Report ISC-607 [Ames Lab., Ames, Iowa]. 1955.
89. LAMPRE I final design status report. U.S. Atomic Energy Commission Report LA-2833 [Los Alamos Scientific Lab., N. Mex.]. 1963.
90. Epstein, L. F. Mechanisms in liquid-phase corrosion: a. solution controlled. In NASA-AEC liquid-metals corrosion meeting. Pp. 45-47. U.S. Atomic Energy Commission Report NASA-SP-41 [National Aeronautics and Space Administration, Washington, D.C.]. 1964.
91. Bircumshaw, L. L. and Riddiford, A. C. Quart. Rev. 6: 157. 1952.
92. Saller, H. A., Rough, F. A., and Bauer, A. A. U.S. Atomic Energy Commission Report BMI-1002 [Battelle Memorial Institute, Columbus, Ohio]. 1955.
93. Saller, H. A., Dickerson, R. F., Murr, W. E., and Bauer, A. A. U.S. Atomic Energy Commission Report BMI-1013 [Battelle Memorial Institute, Columbus, Ohio]. 1955.
94. Saller, H. A., Dickerson, R. F., Murr, W. E., and Hare, A. W. U.S. Atomic Energy Commission Report BMI-959 [Battelle Memorial Institute, Columbus, Ohio]. 1954.
95. Rough, F. A. and Saller, H. A. Ternary uranium alloy. U.S. Patent 2,735,761. Feb. 21, 1956.
96. Rough, F. A. and Saller, H. A. Ternary uranium alloy. British Patent 816,603. July 15, 1959. Abstracted in Nucl. Sci. Abstr. 13: 18183. 1959.
97. Quarterly summary research report in metallurgy: July--September, 1954. U.S. Atomic Energy Commission Report ISC-531 [Ames Lab., Ames, Iowa]. 1955.

98. Quarterly summary research report in metallurgy: July--September, 1953. U.S. Atomic Energy Commission Report ISC-423 [Ames Lab., Ames, Iowa]. 1954.
99. Quarterly summary research report in metallurgy: October--December, 1953. U.S. Atomic Energy Commission Report ISC-453 [Ames Lab., Ames, Iowa]. 1954.
100. Semiannual summary research report in metallurgy: July--December, 1955. U.S. Atomic Energy Commission Report ISC-708 [Ames Lab., Ames, Iowa]. 1956.
101. Myklebust, R. L. Trans. Met. Soc. AIME 224: 354. 1962.
102. Quarterly status report on LAMPRE program for period ending November 20, 1962. U.S. Atomic Energy Commission Report LAMS-2815 [Los Alamos Scientific Lab., N. Mex.]. 1962.
103. Quarterly status report on advanced reactor technology (ART) for period ending January 31, 1965. U.S. Atomic Energy Commission Report LA-3244-MS [Los Alamos Scientific Lab., N. Mex.]. 1965.
104. Davis, W. E., Bergsland, C. H., Brammer, H., Kinginger, J. H., Nance, J. C., Schortmann, W. E., and Wackman, P. H. U.S. Atomic Energy Commission Report CF-52-8-230 [Oak Ridge National Lab., Tenn.]. 1952.
105. Powell, G. W. U.S. Atomic Energy Commission Report NMI-1183 [Nuclear Metals, Inc., Cambridge, Mass.]. 1957.
106. Burwell, C. C., Bidwell, R. M., Hammond, R. P., Kemme, J. E., and Thamer, B. J. Nucl. Sci. Eng. 14: 123. 1962.
107. Epstein, L. F. Introductory remarks. In NASA-AEC liquid-metals corrosion meeting. Pp. 5-20. U.S. Atomic Energy Commission Report NASA-SP-41 [National Aeronautics and Space Administration, Washington, D.C.]. 1964.
108. Owen, C. V., Scott, T. E., and Carlson, O. N. U.S. Atomic Energy Commission Report IS-1031 [Ames Lab., Ames, Iowa]. 1965.
109. Ricci, J. E. The phase rule and heterogeneous equilibrium. New York, N.Y., D. Van Nostrand Co., Inc. 1951.
110. Coughlin, J. P. U.S. Bureau of Mines Bulletin 542. 1954.
111. Fisher, R. W. and Cash, R. J. Corrosion of yttrium by molten uranium above 1150°C. In Annual summary report: July 1967--June 1968. Pp. C & ME 17-18. U.S. Atomic Energy Commission Report IS-1900 [Ames Lab., Ames, Iowa]. 1968.

112. Yue, A. S. and Clark, J. B. Trans. Met. Soc. AIME 221: 383. 1961.
113. Rhines, F. N. Phase diagrams in metallurgy. New York, N.Y., McGraw-Hill Book Co., Inc. 1956.
114. Brasunas, A. deS. U.S. Atomic Energy Commission Report ORNL CF-52-3-123 [Oak Ridge National Lab., Tenn.]. 1952.
115. Stoller, D. R. Interim carburizing procedure. Unpublished paper K-2-4136. Los Alamos, N. Mex., Los Alamos Scientific Lab. 1965.
116. Quarterly status report on advanced reactor technology (ART) for period ending July 30, 1966. U.S. Atomic Energy Commission Report LA-3582 [Los Alamos Scientific Lab., N. Mex.]. 1966.
117. Cavalier, G. Measurements of the viscosity of undercooled molten metals. In The physical chemistry of metallic solutions and intermetallic compounds. Vol. 2. Pp. 54-65. New York, N.Y., Chemical Publishing Co., Inc. 1960.
118. Grosse, A. V. J. Inorg. Nucl. Chem. 25: 317. 1963.
119. Spedding, F. H., Hanak, J. J., and Daane, A. H. J. Less-Common Metals 3: 110. 1961.
120. Grosse, A. V., Cahill, J. A., and Kirshenbaum, A. D. J. Am. Chem. Soc. 83: 4665. 1961.
121. Smith, T. J. Electrochem. Soc. 106: 1046. 1961.
122. Reactor fuels and materials development plutonium research: January--March, 1966. U.S. Atomic Energy Commission Report MLM-1346 [Mound Lab., Miamisburg, Ohio]. 1967.

ACKNOWLEDGMENTS

The author wishes to express his sincere appreciation to Dr. Glenn Murphy, Distinguished Professor and Head of the Department of Nuclear Engineering, for his patience, understanding, and continued support throughout the course of this investigation. He also wishes to acknowledge his gratitude to Mr. Ray W. Fisher for his personal interest and helpfulness in every phase of the problem. Appreciation is expressed to Dr. Morton Smutz for his interest and encouraging advice.

Recognition is given to Mr. Norman Linder, who helped fabricate and weld the many capsule tests; to Mr. Harlan Baker for preparing metallographic specimens; and to Mrs. Floy Sealock, who performed numerous analytical analyses without delay.

Acknowledgment is made to the Ames Laboratory of the U. S. Atomic Energy Commission for providing the financial support and facilities necessary for this research.

The deepest appreciation is expressed to the author's wife, Donna Marie, for her unending aid, encouragement, patience, and moral support; and to his children, Theresa and Bobby, who with their mother's help, made the investigation all worthwhile.

APPENDIX A

The relative degree of solubilities of two or more metals in the same liquid-metal solvent can be correlated by using thermodynamic data for the pure metals, provided that no intermetallic compounds form in the binary systems. Systems in which intermetallic compounds form would require modification of terms to account for the reduced activity of the solute in the solid phase--something that is hard to do for scantily studied systems. The solutions should be dilute and must also obey regular solution theory because Hildebrand solubility parameters (11) are used in the correlation as presented by Pasternak (45).

The solubility of a metal A in liquid-metal B is represented by



where A_{sol} is the solute A in the saturated solution B at the temperature of interest. When the solution B is saturated at a constant temperature, equilibrium occurs and the following activity condition exists:

$$a_A^{\text{solute}} = a_A^{\text{solution}} \quad (78)$$

That is, the activity of the solute A with respect to an arbitrary state of reference is equal to its activity in solution again referred to the same state. The reference state in this case is taken to be pure supercooled liquid A at the temperature of interest. An alternate definition for activity (21) is given by

$$RT \, d \ln a_A = dF_A \quad (79a)$$

or
$$RT \ln a_A = F_A - F_A^{\circ} \quad (79b)$$

where F is the free energy and F° is the free energy at the standard

state.

Enthalpy, H , is related to temperature and the free energy by

$$\left[\frac{\partial (F/T)}{\partial (1/T)} \right]_P = H \quad (80)$$

therefore,

$$H_A^L - H_A^S = \left[\frac{\partial (F_A^L - F_A^S)}{\partial (1/T)} \right]_P \quad (81a)$$

or

$$H_A^L - H_A^S = \left[\frac{\partial (F_A^O - F_A^S)/T}{\partial (1/T)} \right]_P \quad (81b)$$

Combining Equation 79 into 81b yields

$$H_A^L - H_A^S = -R \left[\frac{\partial (\ln a_A)}{\partial (1/T)} \right]_P \quad (82)$$

In integral form we have

$$-R \int_1^{a_A^S} d \ln a_A = \int_{T_m}^T (H_A^L - H_A^S) d(1/T) \quad (83)$$

or

$$\ln a_A^S = 1/R \int_{T_m}^T \frac{H_A^L - H_A^S}{T^2} dT \quad (84)$$

The integration could be carried out exactly if the enthalpies of all phase transformations and the heat capacities (C_p) of the solid and

super-cooled liquid were known as functions of temperature. For the case where $\Delta C_p = 0$ (i.e. the heat capacity is the same for the liquid and solid) with only the solid to liquid phase transformation occurring, Equation 84 simplifies to

$$\ln a_A^S = -\frac{\Delta H_m}{R} \left[\frac{1}{T} - \frac{1}{T_m} \right], \quad (85)$$

where ΔH_m equals the heat of fusion of the solute at the melting point T_m °K. If one or more phase transformations occurs before melting, such as the $\alpha \rightarrow \beta$ transformation for yttrium and praseodymium, the term ΔH_m should be corrected to include the heat of transformation and the heat of fusion.

The problem now is to relate the activity of solute A in solution, a_A^L , to its mole fraction, N_A^L . If the solution is ideal, the activity of A equals its mole fraction

$$a_A^L = N_A^L, \quad (86)$$

and we have from Equation 85

$$\ln N_A^L = -\frac{\Delta H_m}{R} \left[\frac{1}{T} - \frac{1}{T_m} \right]. \quad (87)$$

In general, liquid-metal solutions are not ideal and the activities are not equal to their mole fractions. Therefore, we must use activity coefficients defined as the ratio of the activity to the mole fraction,

$$\gamma \equiv a/N. \quad (88)$$

For the liquid-metal systems of concern here, γ is a number much larger than unity, corresponding to positive deviations from Raoult's Law, and thus solubilities much less than predicted by Equation 87.

The partial molar free energy of mixing, $\Delta\bar{F}$, is related to the activity of the solute in solution by the following equation:

$$RT \ln a_A^L = \Delta\bar{F}_A = \Delta\bar{H}_A - T\Delta\bar{S}_A \quad (89)$$

where $\Delta\bar{H}$ is the partial molar heat of mixing and $\Delta\bar{S}$ is the partial molar entropy of mixing. The latter term is composed of two parts, an ideal contribution and an excess contribution,

$$\Delta\bar{S}_A = \Delta\bar{S}_A^{\text{id}} + \Delta\bar{S}_A^{\text{xs}} \quad (90)$$

with the ideal partial molar entropy given by

$$\Delta\bar{S}_A^{\text{id}} = -R \ln N_A^L \quad (91)$$

Equation 89 thus becomes

$$\ln a_A^L = \Delta\bar{H}_A/RT - 1/R (\Delta\bar{S}_A^{\text{xs}} - R \ln N_A^L). \quad (92)$$

Equating Equations 85 and 92 and substituting ΔS_m , the entropy of fusion for $\Delta H_m/T_m$, leads finally to

$$\ln N_A^L = \frac{\Delta S_m + \Delta\bar{S}_A^{\text{xs}}}{R} - \frac{\Delta H_m + \Delta\bar{H}_A}{RT} = A - B/T. \quad (93)$$

As seen from this equation, a plot of $\ln N_A^L$ versus $1/T$ will yield a curve whose slope is $-(\Delta H_m + \Delta\bar{H}_A)/R$, the sum of the heat of fusion (and phase transformations, if any) and the partial molar heat of mixing. For very dilute solutions, $\Delta\bar{H}_A$ is a constant, and Kleppa and Weil (81) have shown this region to yield a straight line plot. Extension of this straight line portion to $1/T = 0$ gives $(\Delta S_m + \Delta\bar{S}_A^{\text{xs}})/R$,

where the sum of the entropy of mixing ΔS_m also includes any entropy effects from possible phase transformations. Since values of ΔS_m and ΔH_m are listed for the pure elements (28), it is possible to determine $\Delta \bar{S}_A^{xs}$ and $\Delta \bar{H}_A$ from the plot.

Hildebrand and Scott (11) have shown for liquid solutions, where the volume change on mixing is zero, that the partial molar enthalpy of mixing can be approximated by

$$\Delta \bar{H}_A = \Delta E_m = V_A (\delta_A - \delta_B)^2 \phi_B^2 \quad (94)$$

where V_A is the molar volume of the solute and ϕ_B is the volume fraction of the solvent ($\phi_B \approx 1$ for a dilute solution). δ_A and δ_B are the solubility parameters for the solute and solvent, respectively, and are defined by

$$\delta \equiv (\Delta E^V / V_m)^{\frac{1}{2}} \cong [(\Delta H^V - RT) / V_m]^{\frac{1}{2}} \quad (95)$$

The slope of the plot of $\ln N_A^L$ versus $1/T$ can then be used according to Equation 96 to determine an empirical value for the effective solubility parameter of the solvent, δ'_B

$$|\text{Slope}| = \frac{\Delta H_m + V_A (\delta_A - \delta'_B)^2 \phi_B^2}{R} \quad (96)$$

Table 5 lists the solubility data plotted to obtain the curve for $\ln N_{Pr}^U$ versus $1/T$. A least squares fit of the data yielded the following equation:

$$\ln N_{Pr}^U = 2.43 - 11,390/T. \quad (97)$$

Tables 23 and 24 list the thermodynamic properties for yttrium and praseodymium needed for the calculations. Figure 5 in the body of this paper shows the plots for praseodymium in uranium and the predicted curve for yttrium in uranium, as well as the solubilities predicted by ideal solution behavior from Equation 87.

As seen in Figure 5, the solubility curve predicted by this treatment for yttrium and uranium is too low by more than a factor of 10 in the 1200° C range. There are several reasons for this.

1. Praseodymium is a liquid at the temperatures for which Haefling and Daane (2) conducted their tests whereas yttrium is not. This can be compensated for by setting ΔS_m , ΔS_{Trans} , ΔH_m , and ΔH_{Trans} equal to zero in the calculation of δ'_B and $\Delta \bar{S}^{XS}$ for praseodymium in uranium. This yields $\ln N_Y^U = 3.53 - 18,300/T$, which is only slightly above the predicted curve in Figure 5. Actually gadolinium is the rare earth which most resembles yttrium in chemical properties, but sufficient solubility data are lacking. Hence, no prediction could be made using gadolinium.

2. In the derivation of Equation 85 and those which follow, it was assumed that $\Delta C_p = 0$. Whereas $\Delta C_p \approx 0$ for the refractory metals analyzed by Pasternak, the values for praseodymium and yttrium are 1.08 and 1.93 cal/mole^oK, respectively, at their melting points. Accounting for ΔC_p in Equation 84 should give a closer prediction to actual solubilities.

3. The prediction of the solubility equation for yttrium in uranium relies on the accuracy of the data for praseodymium in uranium given by Haefling and Daane. The constants A and B (Equation 12)

dictate the values of $\Delta\bar{S}^{XS}$ and δ'_B used to determine the equation for yttrium in uranium.

The curves for ideal solution behavior for praseodymium in yttrium are also plotted in Figure 5. These values were obtained from Equation 87 using the enthalpy data from Table 23 for ΔH_m . The $\alpha \rightarrow \beta$ transformation energy was also included in ΔH_m . From Equation 87 it is seen that the mole fraction N_A^U is independent of the solvent, and only thermodynamic data of the pure solutes enter into the equation. The solubility predicted by ideal solution behavior is much higher than the actual reported values. In general, most solutions do not exhibit ideal solution behavior, and praseodymium and yttrium in uranium are no exceptions.

Table 23. Thermodynamic values for praseodymium and yttrium

Metal	Melting point T_m (°K)	ΔH_m^a cal/mole	ΔH_{Trans}^a $\alpha \rightarrow \beta$ cal/mole	ΔS_m^a cal/mole°K	ΔS_{Trans}^a $\alpha \rightarrow \beta$ cal/mole°K	V_m^b 298°K cc/mole	ΔH_v^a 298°K cal/mole	$\delta_{298^\circ K}^c$ (cal/cc) ^{1/2}
Pr	1204	1646	757	1.36	0.71	20.81	85,000	63.9
Y	1799	2724	1193	1.51	0.68	19.95	101,500	71.3

^aData from Reference 28.

^bData from Reference 37.

^cCalculated from Equation 95 neglecting RT.

Table 24. Calculation of the effective solubility parameter, δ_B^i , for uranium

System	$ \text{slope} ^B$ Eq. 93	δ_A (cal/cc) ^{1/2}	$\delta_A - \delta_B^i$ (cal/cc) ^{1/2}	δ_B^i (cal/cc) ^{1/2}	$\Delta \bar{S}^{XS}$ cal/mole°K	A Eq. 93
Pr in U	11.39(10 ³)	63.9	31.2	32.7	2.76	2.43
Y in U	16.39(10 ³) ^a	71.3	38.6	32.7	2.76	2.49 ^b

^aThe slope is calculated using δ_B^i from praseodymium in uranium slope and data in Table 23. See Equation 93.

^bCalculated from $\Delta \bar{S}^{XS}$ for praseodymium and data in Table 23. See Equation 93.

APPENDIX B

The diffusion coefficient, D , for the diffusion of yttrium through the stagnant boundary film of thickness δ can be calculated from the equations of Pasternak and Olander (67)

$$Y = \left[\frac{D\mu}{T} \right] \left[\frac{5.31}{k} \right] \left[\frac{V_m}{N_o} \right]^{1/3} = e^{f\delta^1}, \quad (98)$$

where D = diffusion coefficient for the solute in the solvent, cm^2/sec ,

μ = viscosity of pure solvent in poise, $\text{g}/\text{cm}\text{-sec}$,

T = absolute temperature, $^\circ\text{K}$,

k = Boltzmann constant, $1.3805 (10^{-16}) \text{ erg}/^\circ\text{K}$,

V_m = molar volume of the solvent, cc/mole ,

N_o = Avogadro's number, $6.0228 (10^{23}) \text{ mole}^{-1}$,

f = $[\Delta F_\mu^* - \Delta F_D^*]/RT\delta^1$, the fraction of total free energy of (99) activation attributed to the "jump" of an atom from one sight to another,

ΔF_μ^* = free energy of activation for the viscous process, cal. ,

ΔF_D^* = free energy of activation for the diffusive process, cal. ,

R = gas constant, $8.3143 (10^7) \text{ erg}/\text{mole}^\circ\text{K}$ or $1.9872 \text{ cal}/\text{mole}^\circ\text{K}$,

$$\text{and } \delta^1 = \frac{\Delta F_{BB}^*}{RT} \left[1 - \frac{\Delta F_{AA}^*}{\Delta F_{BB}^*} \right]^{1/2}. \quad (100)$$

The free energy terms in Equation 100 are given by

$$\Delta F^* = RT \ln [\mu V_m / h N_o] \quad (101)$$

where terms AA and BB refer to solute-solute and solvent-solvent interactions, respectively, and h is Planck's constant. Thus, in Equation

101 when calculating the solute-solute interaction free energy (ΔF_{AA}^*), values for μ and V_m for the solute must be used at the temperature of interest.

In this case, for a temperature of 950°C (1223°K), uranium and yttrium are still solids, and the question arises as to what values should be used for the viscosity, μ . Cavalier (117) has measured the viscosity of a number of liquid metals in the supercooled liquid state. He found that the data above and below the melting point fall on the same Arrhenius plot. Therefore, values for μ obtained for pure metals above their melting points can probably be extrapolated to lower temperatures with sufficient accuracy to calculate ΔF^* . ΔF^* values can also be obtained from Equation 102 by plotting μ versus $1/T$ values above the melting points, where ΔH^* and ΔS^* are determined from the slope and intercept, respectively:

$$\Delta F^* = \Delta H^* - T\Delta S^*. \quad (102)$$

Here it is assumed that values of ΔH^* and ΔS^* can be used safely at lower temperatures where diffusion actually occurs.

The determination of V_m and μ at various temperatures requires a knowledge of the density, ρ , at these same temperatures. These values are usually available in the literature. Viscosity values at temperatures below the melting points can be calculated by methods from either Chapman (69) or Grosse (70, 118). Chapman's method is used here.

Chapman's method uses an approximate form for the perturbation of the radial distribution function of a monatomic liquid by a non-uniform

flow field. Substituting this form into the expression for the pressure tensor yields an equation for liquid viscosity in terms of an equilibrium function and the interatomic potential energy function. Reduced viscosity then becomes a function of reduced temperature and reduced molar volume, or

$$\mu^* = F(T^*, V_m^*), \quad (103)$$

where

$$\mu^* = \frac{\mu d_G^2 N_A}{[MRT]^{1/2}}, \quad (104)$$

$$T^* = \frac{kT}{\epsilon}, \quad (105)$$

and

$$V_m^* = \frac{M}{\rho N_A d_G^3}. \quad (106)$$

Here d_G is the Goldschmidt atomic diameter, ϵ is an energy parameter (Equation 107), k = Boltzmann's constant, M is the molecular weight, and the $*$ refers to reduced quantities. Other terms have been previously defined. An approximate expression for the energy parameter is given by

$$\epsilon/k = 5.20 T_m, \quad (107)$$

where T_m is the melting point of the metal, $^{\circ}\text{K}$.

Equation 103 becomes

$$\mu^* (V_m^*)^2 = G (1/T^*), \quad (108)$$

and thus reduced viscosities for liquid metals as a general class can be represented by a simple concave curve of the form

$$\mu^* (V_m^*)^2 = A + B/T^* + C/(T^*)^2 + \dots \quad (109)$$

Figure 37 shows the curve Chapman determined on the basis of the viscosity data of twenty-one liquid metals, with a range of densities from 1.8 to 18 g/cc and atomic weights from 6.9 to 242. It is seen that this method accounts very well for viscosities using only the physical variables. Thus the viscosities of liquid metals obey a corresponding-states law as Chapman assumed to derive his equations.

Table 25 is a tabulation of the necessary information to determine the viscosity, μ , and molar volume, V_m , by Chapman's method. With the viscosity values at 950°C it is then possible to determine the diffusion coefficient D using Equations 98 through 101. These values and the value of D for each of the three systems are tabulated in Table 26. The factor Y in Equation 98 is determined from the plot in Figure 38 given by Pasternak (44). This is a plot of Y and δ^1 values determined for 27 liquid-metal systems for which viscosity and diffusion data are available in the literature for both the pure solvent and the pure solute. The best line through the points was determined by the "method of averages" (44) and has a slope of 0.52 passing through the point $\delta^1 = 0$, $Y = 1.13$. The dashed lines on either side of the best line represent 25% deviations. The 0.5 slope indicates one-half of the total-free energy of activation is accounted for in the "jumping" step and one-half in the "hole-making" step in the over-all process of diffusion.

The diffusion coefficient varies with temperature according to an Arrhenius equation of the form

$$D = D_0 \text{ EXP } [-Q/RT], \quad (110)$$

where D_0 is the frequency factor, cm^2/sec , and Q is the activation energy, Kcal/mole. By determining D at various temperatures using the absolute-rate method, it is possible to evaluate the constants D_0 and Q . Following the same procedure as above, values of D for the three systems of interest were determined at 800, 950, and 1100°C. The results are given in Table 27. D_0 and Q were calculated from a semi-log plot of D versus $1/T$ for each system. The activation energy, Q , is a measure of the energy required for the diffusion process and may be compared to the activation energy, ΔE , in Equation 52 and to the interfacial surface tension, γ_{SL} , between the solid metal and the liquid metal. These values should all agree reasonably close with one another for a given system if it is assumed that the activation energy is a measure of the energy barrier to a solid-metal atom passing from the bulk of the container through the interface into the liquid metal, and if the solid-liquid interfacial tension is assumed to be a measure of this energy barrier. Furthermore the process must be diffusion controlled for the activation energies to be similar.

As a comparison, the diffusion coefficients for the three systems were also calculated by the Stokes-Einstein Equation

$$D = \frac{RT}{N_0} \frac{1}{6 \pi \mu r}, \quad (111)$$

where μ = the viscosity of the solvent in poise, and r = the radius of the diffusing atom in cm. These values are presented in Table 27 with

Table 25. Determination of liquid-metal viscosities at 950°C (1223°K) by Chapman's method

Metal	T _m °K	ε/k °K	1/T* °K	M g/mole	ρ @ 1223°K g/cc	V _m cc/mole	d _G Å
Y	1799	9355	7.65	88.905	4.31 (119) ^a	20.64	3.606 (g)
U	1406	7311	5.98	238.03	18.09 (120)	13.16	3.12 (g)
U-Cr	1132	5886	4.81	201.91	16.46 ^b	12.27	3.007 ^d
UCr-Fe ^c	1033	5372	4.39	196.76	16.26 ^b	12.10	2.991 ^d

^aNumbers in parentheses correspond to source references.

^bEstimated by assuming the same % decrease from room temperature to 950°C as pure uranium; i.e., 5.14 % reduction in density.

^cThis corresponds to the UCr-1.0 wt.% Fe alloy.

^dCalculated assuming Vegard's law (21) applies for the lattice parameters: $d_G(\text{UCr-Fe}) = (1/100) [(at.\% \text{U}) (d_{G_U}) + (at.\% \text{Cr}) (d_{G_{Cr}}) + (at.\% \text{Fe}) (d_{G_{Fe}})]$.

Table 25 (Continued)

Metal	V _m [*] Eq.	(V _m [*]) ²	μ [*] (V _m [*]) ² Fig.	μ [*]	d _G ² N _O /[MRT] ^{1/2} cm-sec/g	μ g/cm-sec
Y	0.7309	0.5342	9.84 ^e	18.42	260.47	0.0707
U	0.7194	0.5175	5.36	10.36	118.63	0.0873
U-Cr	0.7493	0.5615	3.34	5.948	120.19	0.0495
UCr-Fe ^c	0.7508	0.5637	2.80	4.967	120.46	0.0412

^eExtrapolated by extending the curve in Figure 37.

the values obtained using the absolute-rate method. Although the Stokes-Einstein equation gives the proper magnitude ($D \approx 10^{-5} \text{ cm}^2/\text{sec}$) for liquid metals, the absolute-rate method should predict values closer to those determined experimentally. Unfortunately, there are no measured diffusivity values of yttrium in uranium, U-Cr, or UCr-Fe alloys for comparison. However, Smith (121) has measured the diffusivity of cerium in uranium over the temperature range 1170-1480°C. The temperature dependence of the diffusion constant is represented by $D = 4.5 (10^{-3}) \times \text{Exp}[-11,000/RT]$. This relation is valid over the range 1170-1350°C. Smith believes that his observed values at higher temperatures were too large because of convective currents. Extending the relationship to supercooled uranium gives a value of $D = 4.87 (10^{-5}) \text{ cm}^2/\text{sec}$ at 950°C. This is about three times greater than that calculated for yttrium in uranium at 950°C. It must be remembered that cerium is a liquid at 950°C and would thus have a larger diffusivity. Based on this, the absolute-rate method appears to predict values fairly close to those found experimentally.

The value for the viscosity of molten uranium at its melting point (1133°C) determined by the method of Grosse (118) ($\mu_U @ 1133^\circ\text{C} = 0.0588 \text{ g/cm-sec}$) was somewhat lower than those determined experimentally (122) ($\mu_U @ 1133^\circ\text{C} = 0.0653 \text{ g/cm-sec}$) and by Chapman's method (69) ($\mu_U @ 1133^\circ\text{C} = 0.0660 \text{ g/cm-sec}$). For this reason, Chapman's method is believed to give the better value for the systems in Table 27.

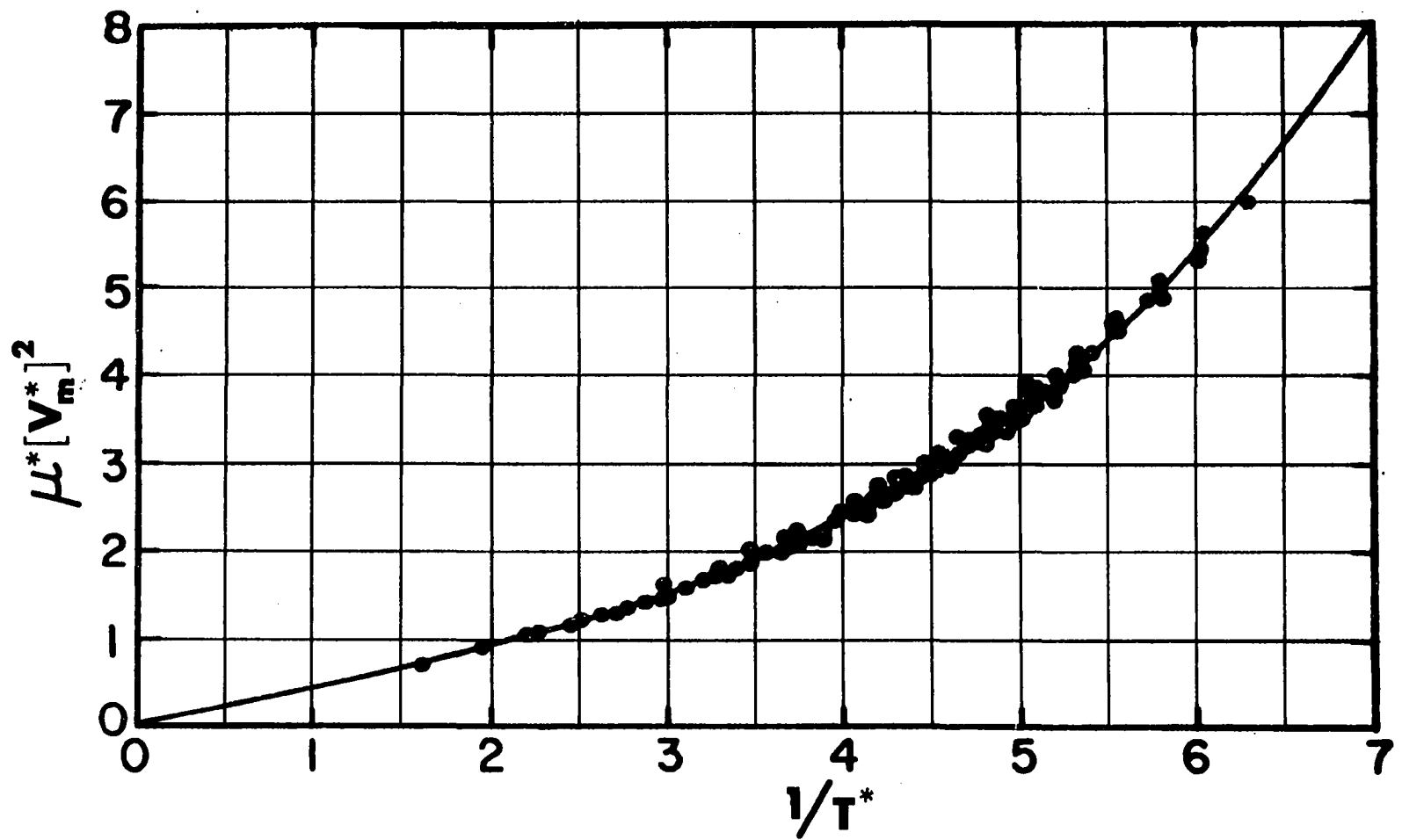


Figure 37. The reduced viscosities of liquid-metals and their dependence on reduced molar volume and reduced temperature (69)

Table 26. Calculation of diffusion coefficients at 950°C by the absolute rate method

System	F_{AA}^*	F_{BB}^*	RT	$\left[\frac{\Delta F_{AA}^*}{\Delta F_{BB}^*} \right]^{1/2}$	$\frac{F_{BB}^*}{RT}$	δ'	Y Fig 38	D (10 ⁵)
	$\frac{\text{Kcal}}{\text{mole}}$	$\frac{\text{Kcal}}{\text{mole}}$	$\frac{\text{Kcal}}{\text{mole}}$					$\frac{\text{cm}^2}{\text{sec}}$
Y in U	14.344	13.763	2.430	1.0209	5.663	-0.118	1.064	1.39
Y in U-Cr	14.344	12.213	2.430	1.0837	5.025	-0.421	0.909	2.14
Y in UCr-Fe	14.344	11.733	2.430	1.1057	4.828	-0.510	0.868	2.46

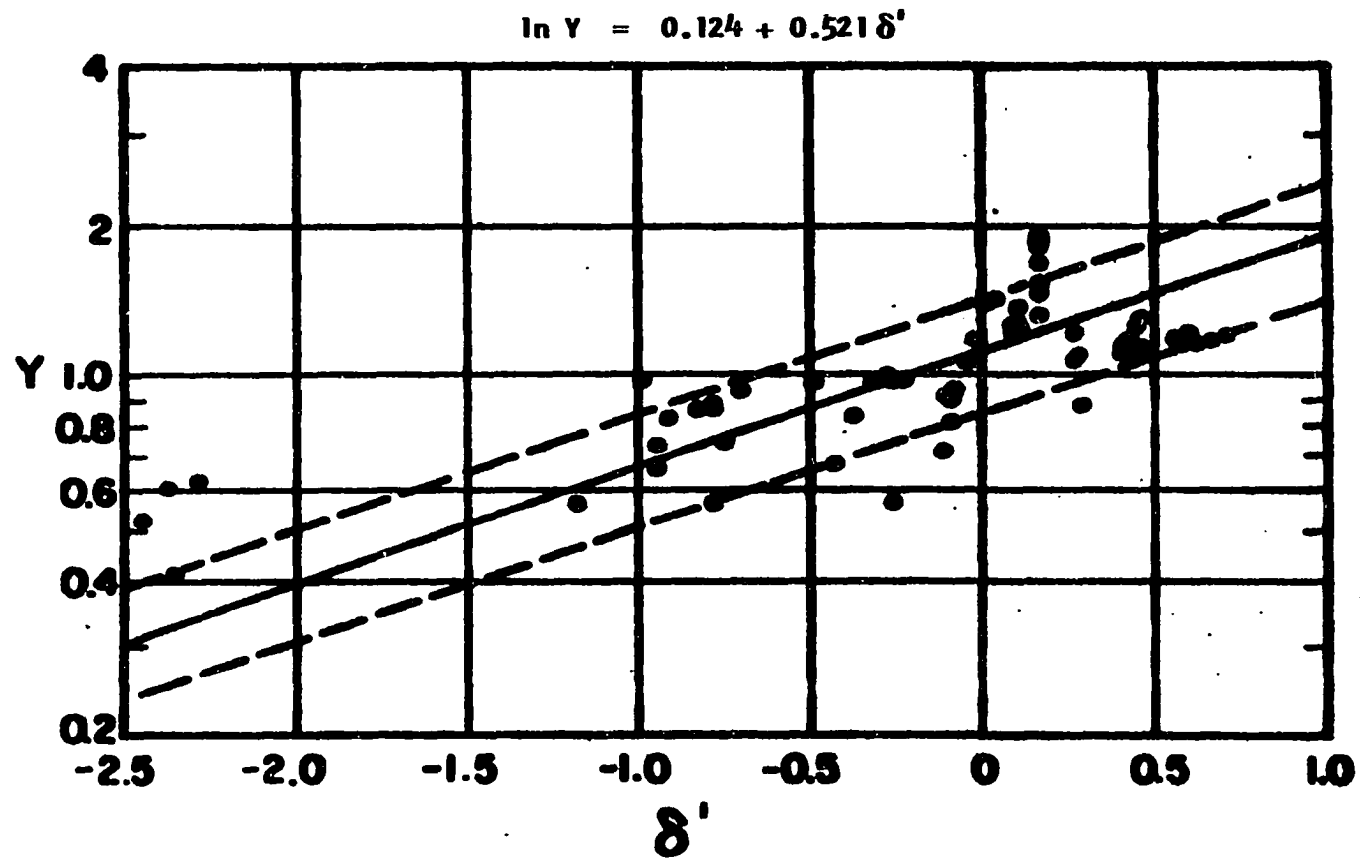


Figure 38. Correlation of mutual diffusion data in liquid-metal systems by the absolute-rate method (44)

Table 27. Summary of diffusion coefficients calculated by the absolute-rate method and the Stokes-Einstein equation for various temperatures

System	Temperature		$\frac{1000}{T}$	$D \times 10^5$	Activation Energy	$D_0 \times 10^5$	$D \times 10^5$
	$^{\circ}\text{C}$	$^{\circ}\text{K}$	$^{\circ}\text{K}^{-1}$	cm^2/sec	$\frac{Q}{\text{mole}}$ Kcal	cm^2/sec	cm^2/sec
Y in U	800	1073	0.9320	0.933	7.162	26.75 ^a	0.375 ^b
	950	1223	0.8177	1.39	7.162	26.75	0.569
	1100	1373	0.7283	1.95	7.162	26.75	0.800
U in U-Cr	800	1073	0.9320	1.51	6.355	29.58	0.705
	950	1223	0.8177	2.14	6.355	29.58	1.00
	1100	1373	0.7283	2.90	6.355	29.58	1.35
Y in UCr-Fe ^c	800	1073	0.9320	1.76	6.136	31.15	0.861
	950	1223	0.8177	2.46	6.136	31.15	1.21
	1100	1373	0.7283	3.29	6.136	31.15	1.59

^a D_0 is the constant in Equation 110: $D = D_0 \text{ Exp } [-Q/RT]$.

^bDiffusion coefficients calculated by standard Stokes-Einstein equation for comparison with the absolute-rate method (Equation 111).

^cEutectic was assumed to be that of Saller *et al.* (51): 99.0 wt.% UCr eutectic-1.0 wt.% Fe.